Investigation of cutting mechanics in single point diamond turning of silicon

by

Amir Mir

A thesis submitted to the University of Strathclyde
for the degree of
Doctor of Philosophy

Department of Design, Manufacture and Engineering Management
University of Strathclyde
Glasgow, UK

September 2016

This thesis is the result of the author’s original research. It has been composed by the author and has not been previously submitted for examination which has led to the award of a degree.

Signed: Date:

Abstract

As a kind of brittle material, silicon will undergo brittle fracture at atmospheric pressure in conventional scale machining. Studies in the last two decades on hard and brittle materials including silicon, germanium, silicon nitride and silicon carbide have demonstrated ductile regime machining using single point diamond turning (SPDT) process. The mirror-like surface finish can be achieved in SPDT provided appropriate tool geometry and cutting parameters including feed rate, depth of cut and cutting speed are adopted.

The research work in this thesis is based on combined experimental and numerical smoothed particle hydrodynamics (SPH) studies to provide an inclusive understanding of SPDT of silicon. A global perspective of tool and workpiece condition using experimental studies along with localized chip formation and stress distribution analysis using distinctive SPH approach offer a comprehensive insight of cutting mechanics of silicon and diamond tool wear. In SPH modelling of SPDT of silicon, the distribution of von Mises and hydrostatic stress at incipient and steady-state was found to provide the conditions pertinent to material failure, phase transformation, and ductile mode machining. The pressure-sensitive Drucker Prager (DP) material constitutive model was adopted to predict the machining response behaviour of silicon during SPDT. Inverse parametric analysis based on indentation test was carried out to determine the unknown DP parameters of silicon by analysing the loading-unloading curve for different DP parameters. A very first experimental study was conducted to determine Johnson-Cook (J-C) model constants for silicon. High strain rate compression tests using split Hopkinson pressure bar (SHPB) test as well as quasi-static tests using Instron fatigue testing machine were conducted to determine J-C model constants.

The capability of diamond tools to maintain expedient conditions for high-pressure phase transformation (HPPT) as a function of rake angle and tool wear were investigated experimentally as well as using SPH approach. The proportional relationship of cutting forces magnitude and tool wear was found to differ owing to wear contour with different rake angles that influence the distribution of stresses and uniform hydrostatic pressure under the tool cutting edge. A new quantitative evaluation parameter for the tool wear resistance performance based on the cutting distance was also proposed. It was also found that the machinability of silicon could be improved by adopting novel surface defect machining (SDM) method.

The ductile to brittle transition (DBT) with the progressive tool wear was found to initiate with the formation of lateral cracks at low tool wear volume which transform into brittle pitting damage at higher tool edge degradation. A significant variation in resistance to shear deformation as well as position shift of the maximum stress values was observed with the progressive tool wear. The magnitude and distribution of hydrostatic stress were also found to change significantly along the cutting edge of the new and worn diamond tools.

Acknowledgements

First and foremost, I would like to express my sincere gratitude to my supervisor Prof. Xichun Luo for his invaluable guidance, encouragement, and constant support throughout this research. I feel extremely fortunate to have such a wonderful person as my supervisor who showed continued patience and support equally in good and tough times. I am also grateful to my co-supervisor Dr. Amir Siddiq for his guidance and support. His expertise in finite element analysis field has truly been a great advantage in this research.

I would also like to thank University of Huddersfield and University of Strathclyde for providing me the generous financial support in the form of full scholarship.

I extend my sincere appreciation to Prof. Kai Cheng (Brunel University, London) for providing diamond machining facilities, Dr. Jining Sun (University of Hariot-Watt, Edinburgh) for providing support in scanning electron microscopy and Mr. Andrew Cox (Contour Fine Tooling limited, UK) for his generous support and recommendations. My sincere thanks to Dr. John Harrigan (Amec Foster Wheeler) and Dr. Salisu Elhussein (University of Aberdeen, UK) for their helpful suggestions in high strain rate compression testing, Dr. Feifei Jiao (Brunel University, UK) for his help during SPDT trials, Dr. Imran Tariq (University of Surrey, UK) for providing IT resource facilities, and Mr. Dieter Marschall (Ametek Inc., Germany) and Mr. Chris Dawson (University of Huddersfield, UK) for providing training on diamond turning and metrology. I would also like to thank Mr. Wenbin Zhong for help in surface

roughness measurements and Dr. Zhen Tong (University of Huddersfield) for his useful discussions.

I am truly indebted and thankful to my parents for their endless love and continuous support and care throughout my life; and to my wife who was encouraging, supportive and caring. Special thanks to my uncle Mr. Farhat Ali Mir whose encouragement and support throughout my life will always be appreciated.

Finally, praise is to my Lord who endowed me an intellect, health, wealth, and company of all those wonderful people around me who contributed to my achievements in a better way.

Table of contents

List of Figures

List of Tables

Abbreviations

ALE = Arbitrary Lagrangian Eulerian

BCC = Body-centred-cubic

BDT = Brittle to ductile transition

CAE = Complete Abaqus Environment

C-L = Cockroft-Latham

CVD = Chemical Vapour Deposition

DBT = Ductile to brittle transition

DEM = Discrete element method

DOE = Diffractive optical elements

EDT = Extended Delaunay tessellation

EFG = Element Free Gelarkin

EUL=Eulerian

FCC = Face-centred cubic

FDM = Finite difference method

FEA = Finite element analysis

FEM = Finite element method

FPM = Finite point-set method

FTS = Fast tool servo

HPHT = High-pressure High-temperature

HPPT = High-pressure phase transformation

JC = Johnson-Cook

LAG = Lagrangian

MD = Molecular dynamics

MEMS = Micro-electro-mechanical systems

PFPE = Perfluoropolyether

PFEM = Particle finite element method

PSZ = primary shear zone

SDM = Surface defect machining

SDZ = Secondary deformation zone

SEM = Scanning electron microscopy

SHPB = Split Hopkinson pressure bar

Si= Silicon

SiC= Silicon Carbide

SPDT = Single point diamond turning

SPH = Smoothed particle hydrodynamics

SSS = Slow slide servo

STS = Slow tool servo

TDZ = Tertiary deformation zone

T-M = Takeyama and Murata

Nomenclature

E = Young's modulus

P = Indentation load

H = hardness of material

z_{eff} = ductile-brittle transition distance

σ_n = Normal stress

$\bar{\sigma}$ = Effective stress

σ^m= Maximum stress

$\sigma_{1,}, \sigma_2, \sigma_3$= Principle stress

σ_y= yield stress

σ_{fl} = Tensile failure stress

τ_{fl} = Shear failure stress

$\bar{\varepsilon}$ = Effective strain

$\bar{\varepsilon}^p$ = Equivalent plastic strain

$\bar{\varepsilon}_f^p$ = Equivalent strain at failure

A,B,C,m,n = Johnson-Cook model constants

$d_1$to d_5 = Johnson-Cook failure constants

F,L = Usui's wear model constants

σ^* = Pressure to von Mises stress ratio $(\frac{p}{q})$

$\dot{\varepsilon}_0$= Reference strain rate

$\dot{\varepsilon}^p$ = Plastic strain rate

χ = Thermal conductivity in temperature equation

$\dot{Q}$ = Rate of heat flux

C_p = Specific heat

q = Von Mises stress

F_c= Tangential cutting force

F_t = Thrust force

μ = Coefficient of friction

μ_{adh} = Adhesive friction coefficient

T_{melt} = Melting temperature

T_r = Reference temperature

T_{mod} = Velocity modified temperature

T = Material temperature

$\dot{\omega}$ = Wear rate

w_{aR} = Approx. recession of rake face

τ = Shear stress

R = Universal gas constant

ε^p = Plastic strain

G(v,f) = Takeyama-Morata abrasive wear term

ε_i = Incident strain

ε_r = Reflected strain

ε_T = Transmitted strain

ε_n = shear strain

V_o = output voltage

V_{in} =Input voltage

C_b = wave speed

A_b = cross-sectional area of split Hopkinson bars

A_s = cross-sectional area of specimen

List of Publications

Journal papers:

1. **Amir Mir**, Xichun Luo, Amir Siddiq, "Smoothed particle hydrodynamics study of surface defect machining for diamond turning silicon". The International Journal of Advanced Manufacturing Technology, 2016: pp. 1-16
2. **Amir Mir**, Xichun Luo, Jinning Sun, "The investigation of influence of tool wear on ductile to brittle transition in single point diamond turning of silicon". WEAR, 2016: pp. 233-243.
3. **Amir Mir**, Xichun Luo, Kai Cheng, Andrew Cox, "Investigation of influence of tool geometry in single point diamond turning of silicon". International Journal of Mechanical Sciences, (2016), under review.
4. **Amir Mir**, Amir Siddiq, Salisu Elhussein, Xichun Luo, John Harrigan, "Determination of Johnson-Cook constitutive model constants for silicon for machining applications", Journal of Applied mechanics, (under review)
5. **Amir Mir**, Xichun Luo, "The development of finite element modeling for machining of metals: A review", Manufacturing Review, In preparation.

Conference papers:

1. **Amir Mir**, Xichun Luo, Amir Siddiq, "Numerical simulation of triaxial test to determine the Drucker-Prager parameters of silicon".

Automation and computing (*ICAC*), 21st International conference, Glasgow, UK, 11-12 Sept 2015, pp. 1-4

2. **Amir Mir**, Xichun Luo, Amir Siddiq, “A numerical investigation on the effect of tool geometry in single point diamond turning of silicon”, Euspen 15th International conference & Exhibition, Leuven, Belgium, June 2015, pp.317-318

Chapter 1- Introduction

1.1 Background and significance

Brittle materials such as silicon and germanium are widely used in semiconductors, micro photonics and weight sensitive infrared applications due to their low mass density, high refractive index, and low thermal expansion coefficient. Silicon is considered as one of the most preferred materials in the manufacturing of micro-electro-mechanical systems (MEMS) devices. Also, there is a growing need for surface texturing to enhance performance capabilities of silicon components in various fields. The surface finish and form accuracy are the key requirements of silicon-based functional surfaces.

Although silicon is an ideal material for many applications, its pressure-dependent characteristics make it difficult to machine. Brittle fracture is an impediment to high surface quality during machining. At conventional scale and using conventional machine tools, silicon undergoes brittle fracture and fails to resist load prematurely without any ductile deformation. Machining of silicon through traditional methods becomes extremely time consuming and costly as it requires grinding, lapping and polishing to remove surface defects and achieve high surface finish. However, silicon and other hard and brittle materials can be machined in ductile mode at micro and nano scale using ultraprecision machine tools. Single point diamond turning (SPDT) has emerged as an effective ultraprecision technique to fabricate products with high form accuracy and optical surface finish without the need of subsequent polishing. SPDT with slow tool servo (STS) and fast tool servos (FTS) can be utilized to manufacture a wide variety of freeform and structured surfaces in single turning operation and very complex surfaces can be manufactured with high optical quality [1]. Also, spindle and linear slides induced errors in conventional diamond turning can be successfully compensated by fast tool servo to further improve high form accuracy [2, 3].

However, SPDT of silicon is inherently a complex process that includes machining through chipping, brittle fracture, ductile deformation, chemical reaction and phase transformation [4-6]. The machining response behaviour of silicon under the cutting edge abruptly changes due to any change in tool edge condition, hydrostatic pressure and various other factors. One of the possible ways to achieve plastic deformation of silicon is through structural transformation into metallic phase under high hydrostatic pressure refers to high-pressure phase transformation (HPPT) [7]. The HPPT yields multiple phases dependent on scale and gradient of hydrostatic pressure during loading and unloading conditions.

In recent years, although a fair level of understanding of tool geometry, chip formation mechanism, phase transformation and cutting parameters has been reached, the process still lacks in absolute understanding of complex interplay of input and output variables. The catastrophic wear of diamond cutting tools is a critical aspect that influences the surface integrity and operational cost of SPDT. From tool geometry perspective, diamond tools with negative rake angle and nanometric cutting edge radius were commonly agreed to provide high hydrostatic pressure ensuing brittle to ductile transition (BDT) [8-10]. However, the optimal rake angle and cutting edge is still required to be determined for prolonged ductile cutting distance at a reduced tool wear rate.

Wear mechanism of diamond tools, as well as the factors, contribute to tool wear are still not fully identified.

In this regard, the challenge is to provide an inclusive understanding of localized cutting mechanics of silicon under the tool cutting edge during the chip formation. It is non-trivial to identify the conditions responsible for severe tool wear and explore the techniques to reduce it.

1.2 Aim and Objectives

The aim of this work is to gain a profound understanding of cutting mechanism of silicon to contribute to a deterministic SPDT process of brittle materials. To achieve this task, experimental and numerical studies were performed to determine conditions favourable to BDT. The main objectives of these experimental and numerical studies are:

- To study and identify the machining conditions that will facilitate ductile mode machining.
- To develop a finite element simulation model of machining of silicon using suitable material constitutive model.
- To identify the tool geometry that can facilitate ductile regime machining of silicon for longer cutting distance while undergoing the least tool wear.
- To identify failure stress of silicon during SPDT process and determine material constitutive model constants using quasi-static and high dynamic compression tests.

- To investigate the machining performance improvement by adopting newly developed surface defect machining (SDM) method.

1.3 Structure of thesis

The chapters of this thesis are organized as follows:

Chapter 1 describes the background and importance of this research work and explains the aim and objectives.

Chapter 2 presents the synopsis of significant developments in SPDT and addresses the fundamental challenges confronted by SPDT in machining hard and brittle materials. The chapter explains the HPPT based brittle-ductile transition phenomenon and tool wear mechanisms associated with SPDT of brittle materials. It also briefly describes different developed techniques to reduce diamond tool wear and suitable cutting parameters, cutting conditions and tool geometry.

Chapter 3 presents the review of the development of FEM machining modelling from the perspective of chip formation and tool wear. Different FEM formulations with their advantages and limitations are highlighted. Important output solution variables are discussed.

Chapter 4 describes the implementation of smoothed particle hydrodynamics (SPH) approach in SPDT of silicon. The chapter addresses the development of SPH machining model of silicon, its implementation process in Abaqus, its capabilities as well its limitations. It also presents a study of inverse analysis to determine the parameters of the Drucker Prager constitutive model for silicon.

Chapter 5 presents the experimental study of the determination of Johnson’s Cook model constants of silicon using quasi-static and high strain rate compression tests. The determined constants are validated using experimental trials and numerical simulation of machining.

Chapter 6 presents the experimental and numerical study of SPDT of single crystal silicon. The study is focused on chip formation and diamond tool wear measurement when different tool geometries were adopted.

Chapter 7 presents experimental and numerical study of the transition of machining mechanism of silicon from ductile to brittle mode with the progressive tool wear. The distribution of von Mises and hydrostatic pressure along the cutting edge of the diamond tool is also investigated.

Chapter 8 documents the details of SPH simulation study of recently developed surface defect machining method (SDM) for SPDT of silicon. Material response behaviour for different defects was investigated and compared for cutting performance.

Chapter 9 concludes the thesis with a summary of contributions to literature and possibilities of future work.

Chapter 2- Literature review

2.1 Introduction

High surface quality and performance requirements of advanced optics have inspired the existing trend of fabrication of functional surfaces on hard and brittle materials. Hard and brittle materials such as silicon, silicon carbide, silicon nitride, etc. offer excellent wear and chemical resistance, high-temperature strength and lower thermal expansion compared to soft and ductile materials such as copper, brass and aluminium. However, mmachining of hard and brittle materials in ductile-regime is a complex process which is highly reliant on controlled material removal with special machine tools of high stiffness and motion accuracy. When brittle materials are machined using conventional machine tools and under conventional machining conditions, poor machined surface is generated with surface and sub-surface defects. Although subsequent grinding and polishing techniques can be adopted to remove the subsurface damage and improve surface quality, they lack in cost and time efficiency.

In addition to the requirement of flat optical surfaces, fabrication of freeform and structured surfaces such as micro-lens arrays (MLAs), Fresnel lens, polygon mirrors, multifocal lenses on hard and brittle materials are also growing [11, 12]**.** Different individual features of functional surfaces exploited in engineering optics, semiconductor, and biomedical applications are shown in Fig. 2-1.

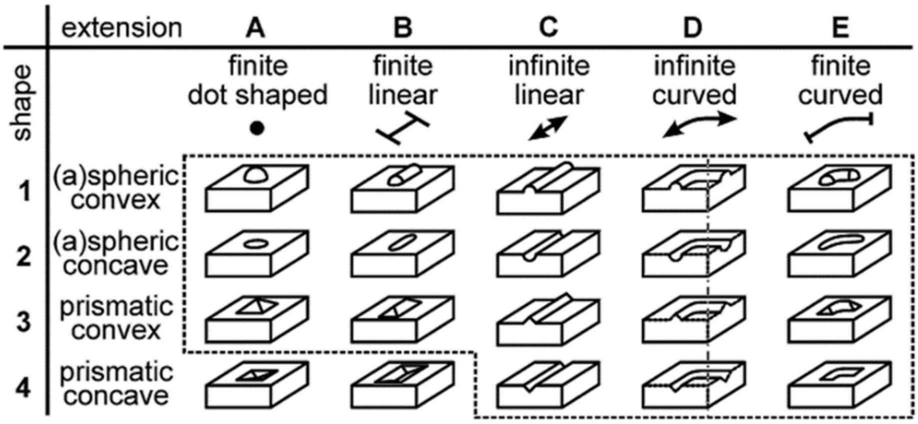

Figure 2-1: Different type of structures based on shape and extension [1]

In order to fabricate these surfaces to high form accuracy and surface finish, brittle materials are required to be machined in ductile mode. Lithographic (electron beam lithography, LIGA, etc.) and replication techniques are among the most famous manufacturing techniques to produce functional surfaces [13-18]**.** These methods are capable of fabricating anti-reflective surfaces, diffractive optical elements (DOEs) microstructures, microlens array, etc. and many other complex surfaces of short spatial wavelength of the order of sub-micrometer level [19-25]. However, in applications where high precision is crucial, these techniques lack in providing the required accuracy and surface quality. Lithographic and replication techniques are suitable for mass production and becomes time-consuming and expensive when a small batch of components are required.

2.2 Ultraprecision machining

The advancement of machining from conventional to ultraprecision can be credited to the increasing requirement of form accuracy, surface finish, and geometric complexity [26]. Taniguchi [27] in 1983 presented a map of predictive requirement and evolution of machining accuracy as shown in Fig. 2-2 .

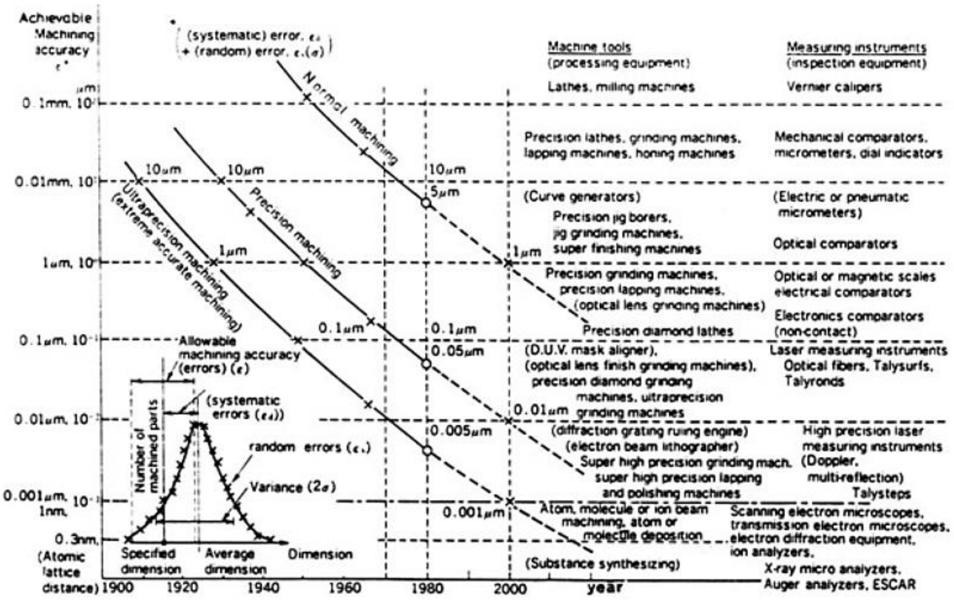

Figure 2-2: Machining accuracy requirement and advancement of machining methods -Taniguchi predictions [27]

Large ultraprecision surfaces such as mirrors for the large-scale telescopes as well as structured surfaces with subnanometer features are required to be manufactured with submicron form accuracy and subnanometer surface finish. Ultraprecision machining such as diamond turning, diamond milling, etc. is a sophisticated technique to maintain surface properties and sub-surface integrity of a machined material. Since ultraprecision machine tools provide motional slides with submicron accuracy and operate at <10nm resolution, functional surfaces can be manufactured with submicron geometrical tolerance and sub-nanometer surface finish.

Ultraprecision machining techniques can be characterized by material removal processes or by energy involved in machining such as mechanical energy (turning, milling, fly cutting etc.), electrical energy, heat Energy (e.g. laser cutting), chemical energy (e.g. electrochemical machining).

2.3 Single point diamond turning (SPDT)

SPDT is one of the most preferred processes in many industries due to its manufacturing precision, high productivity and maximum material removal rate, ability to manufacture complex surfaces, and capability to produce optical quality surfaces. The process was also expedient to manufacture soft material optics which were difficult to polish. When compared to grinding and polishing, SPDT can produced components with better accuracy, quicker manufacturing time and at a reduced cost. Diamond turning is superior to lithography for better relative tolerance of parts. There are no economically viable techniques except diamond turning methods to produce individual diffractive optical elements (DOE) of complex geometry [28-30]. Photolithographic techniques are successfully replaced by diamond turning to produce micro-optics for the compact optoelectronic and micro-electro-optical mechanical systems in various industries (surveillance, biomedical, telecommunication etc.). Free form solid generators with multiple axes and single crystal diamond tool can manufacture several types of micro-optics by allowing the fabrication of three-dimensional structures with the same lithographic dimensional accuracy [31]. An example of a modern diamond turning machine is shown in Fig. 2-3.

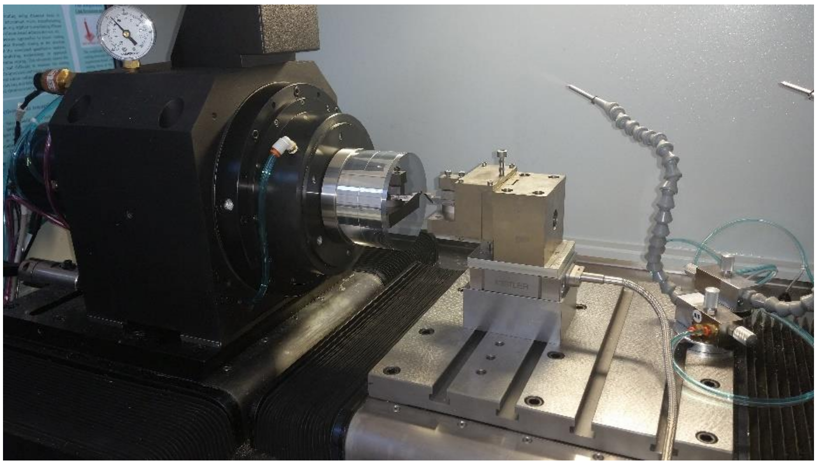

Figure 2-3: Modern diamond turning machine (Moore Nanotech 250 UPL)

The performance of diamond turning techniques is solely limited due to the non-machinability of certain materials owing to high wear rate involved. However, SPDT can be employed to produce complex moulds of high form accuracy and finish on machinable materials, which are then used to produce the complex end products of non-machinable materials using other techniques.

2.3.1 Advent and development of Single point diamond turning (SPDT) machines

During World War II, fabrication of Schmidt correctors for infrared optical systems in Polaroid corp. in USA and Philips in Holland can be considered as the evolution of SPDT [32]. In the late 1970s, standard diamond turning machines were introduced with their commercial applications. In 1982, a Large Optics Diamond Turning Machine (LODTM) built at Lawrence Livermore National Laboratory (LLNL) in USA for diamond turning of annular resonator optics [33]. The capacity to hold the workpiece on LODTM was a 64-inch diameter, 20-inch length and a maximum weight of 3000 pounds. Tool positioning accuracy achieved on this machine was 1.1 microinches RMS.

Another small two-axis diamond turning machine was built in 1982 by Material Fabrication Division workers at Lawrence Livermore National Laboratory (LLNL). The name given to this small diamond turning machine was Baby Optics Diamond Turning Machine (BODTM) [34]. This machine was assembled with commercially available components and could produce aspheric parts up to 4-inch diameter with a dimensional accuracy of 10 µinch with a surface finish of 1µinch. In 1992, an environment-controlled diamond turning machine named “Capsule” was designed and built by Tokyo Institute of Technology Japan [35]. This machining mechanism was enclosed in a capsule shaped structure and therefore the name was given on the basis of its shape.

Diamond turning machines were mainly developed for the generation of rotationally symmetric surfaces. The limited bandwidth of the slide axis, as well as limited controller performance, makes them incongruous to machine micro-structured and non-rotationally symmetric freeform surfaces. Machining of such surfaces requires large data volume and fast data transfer rate as an input/output function. Conventional DTM controllers lack in computational power and their limited architecture restrict any major changes in control algorithms. In diamond turning complex surfaces, spindle speed needs to keep high to achieve better surface finish and to attain higher material removal rate. Synchronisation of the sliding axis with the spindle axis on high speed cannot be technically and economically achieved with the parent sliding axis mechanism and therefore the need for the introduction of slow tool servo (STS) and fast tool servo (FTS) was crucial.

2.3.2 Slow tool servo and fast tool servo

In STS, also known as slow slide servo (SSS), workpiece is mounted on the position controlled spindle axis (C-axis). Spindle axis is velocity controlled in conventional diamond turning machining. In order to produce microstructured or free form surfaces, spindle axis is required to be in a position controlled mode and synchronous to all other sliding axes of the machine. When the spindle rotates, the tool oscillates on Z-axis of the machine, having knowledge of the position of the workpiece. The three axes X, Z, and C are fully coordinated position control axes and machine system can be expressed as a cylindrical coordinate system (X, θ, Z). The key benefits of STS system are its oscillation range up to 25 mm, quick and easy setup, and economical as well as high machining accuracy. Off-axis machining, as well as off-axis fixtures, are expensive, technically challenging as well as time-consuming in comparison with on-axis machining. Fabrication of off-axis components requires large swing capacity, which can’t be achieved with conventional diamond turning machines. With STS and long stroke FTS, off-axis components can now be turned on-axis, due to large travel range [36, 37]. STS are required to machine surface with non-rotational symmetry greater than 70 µm.

Diamonds turning of complex microstructured and non-rotationally symmetric surfaces require tool actuation frequency much higher than the rotational speed of the spindle. This higher tool bandwidth can only be achieved by FTS technology which is considered as one of the most reliable and imperative technologies for the manufacturing of complex optics. FTS are superseding due to its quick setup, fabrication time, and capability to fabricate a diverse range of complex surfaces. The working principle of FTS and STS is shown in Fig. 2-4.

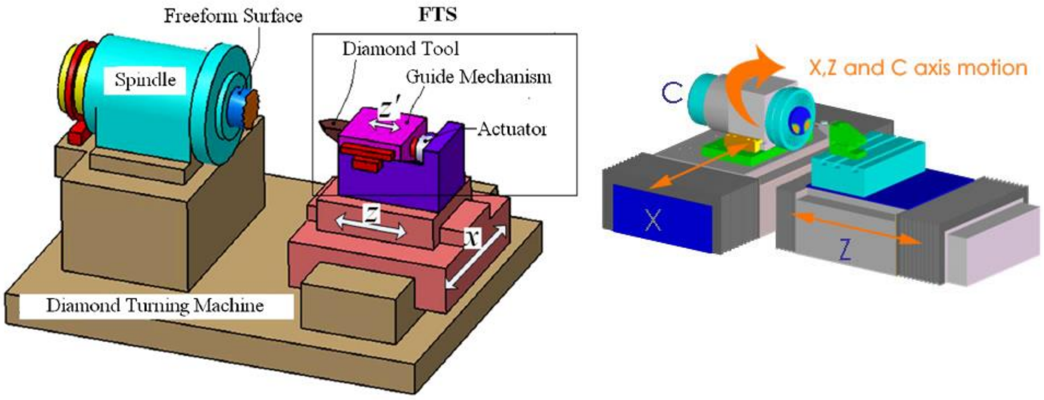

Figure 2-4: working principle of FTS and STS [38]

In FTS system, an auxiliary axis is mounted on the translational slide (normally Z slide) of the machine to oscillate the tool with high frequency and with stroke range from µm to mm range. The bandwidth of FTS system decreases with the increase of stroke length and mass of actuating mechanism. Like conventional diamond turning machines and unlike STS, the spindle is not position controlled. In FTS machining, spindle uses an encoder to provide its position information to FTS system. FTS mainly comprises of an actuating mechanism and a control system to perform its functions along with some supplementary features to optimize its performance.

2.4 Extension of SPDT technique to machine of brittle materials

Technical advancement and miniaturization of electromechanical devices have boosted the demand for ultraprecision optical elements. In early years, the application of SPDT was restricted to machining of optical surfaces on ductile and soft non-ferrous materials. In recent years, fabrication of micro-structured and freeform surfaces on hard and brittle materials has increased [38]. In order to achieve required functional performance from such surfaces, a high optical machined surface with high form accuracy is required. Diamond due to its tremendous mechanical and chemical properties can machine both ductile and brittle materials with required surface finish and form accuracy. One of the distinctive properties of diamond is its extreme hardness that provides higher resistance than other elements. Due to non-adhesive characteristics of a diamond and very small affinity to wide range of materials, diamond exhibit low frictional resistance with most of the materials. This approving behaviour results into low cutting forces and high optical machined surface quality [39].

2.4.1 Diamond cutting tools in SPDT process

Diamond is a crystalline allotrope of Carbon and known as one of the extremely hard materials. It is also a great thermal conductor with an extremely low thermal expansion. Another crystalline allotrope of Carbon is graphite. Diamond and graphite have almost similar thermodynamic stability ($\Delta G = 0.4$ eV at 300K) but they differ in terms of their kinetic stability. In diamond, each carbon atom bonded to four other carbon atoms at a distance of 1.54A°. Strong directional SP3 bonding of diamond is attributed to its extreme hardness, heat conductivity and refractive index.

Diamond cutting tools are produced by natural diamond stones as well as synthetic diamonds. Synthetic diamonds are generally produced at high temperature and pressure by two main high-pressure high-temperature (HPHT) [40] and chemical vapour deposition (CVD) [41] methods. Table 2-1 lists the properties of silicon and diamond tools.

Table 2-1: Properties of silicon diamond tools [103,111,112]

Properties	Natural diamond tools	silicon	Chemical vapour diamond tools
Element symbol	C	Si	C
Density (kg/m^3)	3520	2330	3515
Melting point (°C)	3700	1415	
Hardness (kg/mm^2)	7000-10,000	850	10,000
Crystal structure	Diamond cubic	Diamond cubic	
Yield strength (GPa)	35-60	2.9-7	35-60
Poisson’s ratio	0.2	0.273	0.1
Fracture toughness ($MPa.m^{1/2}$)	2.0	0.82	
Young’s modulus (GPa)	1223	129-190	1050
Thermal conductivity (W/m.K)	>1800	150	1800
Thermal expansion(K^{-1})	1.0 x 10^{-6}	2.6 x 10^{-6}	1.0 x 10^{-6}

The mechanical and physical characteristics of diamond tools vary with the crystal orientation of the stone. The wear resistance of diamond tool in the different crystallographic orientation of rake and flank faces decide wear type and wear rate.

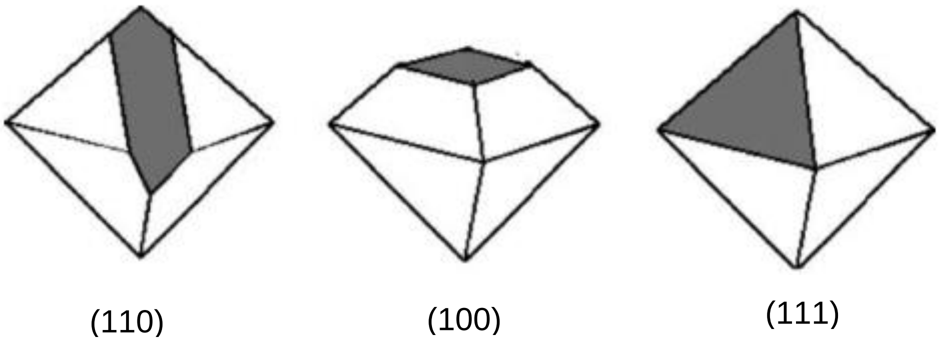

Figure 2-5: schematic of different crystal orientation of diamond [97]

Different crystal orientations of diamond are shown in Fig. 2-5. The tangential and thrust forces vary under the influence of wear resistance of tool to material and can be quantified during experiments.

Sharif Uddin et al. [42] conducted nano-scale machining of silicon and found that wear resistance of diamond tool is higher when using (110) of crystal orientation in rake face compared to (100) and (111) orientation. They found lower thrust forces using (110) orientation compared to the other two. However, under different cutting conditions, they found that tool rake face with (100) and flank face with (110) offer high wear resistance in diamond turning silicon [43].

Cheng et al. [44] performed experimental and molecular dynamics (MD) simulation studies of scratch test of silicon using atomic force microscope (AFM) diamond tip. They concluded that diamond tools with (100) plane as both the rake face and clearance face provide the highest strength, therefore, less wear rate compared to (110) plane.

2.4.2 Machining mechanism of brittle materials

Material removal during machining is achieved mainly through two well- known mechanisms: ductile-mode and brittle-mode mechanisms. In the ductile mode, shear stress exceeds the critical value of material-dependent shear strength and deformation initiate due to slip in specific closed-packed crystallographic planes in specific directions. The chip formation occurs through the continuous plastic flow of material in front of the cutting edge. In the brittle mode, material fails to resist load prematurely before its yield point and chips are formed by the initiation and evolution of cracks.

The potential of machining brittle materials through plastic deformation was first narrated by King and Tabor in 1954 [45]. During the abrasive wear of rocks, they observed the material behaviour through plastic deformation along with typical brittle fracture. The former studies of plastic deformation of brittle materials in different processes and under different conditions were reported by Huerta and Malkin [46], Tow and McPherson [47] and Moore and King [48]. Bifano et al. [49] performed micro-grinding of brittle materials and suggested that ductile-regime grinding of brittle materials can be achieved provided machining is performed with stiff machine tool and small depth of cuts.

2.4.3 High-Pressure phase transformation (HPPT)

The high-pressure phase transformation (HPPT), which is also known as Herzfeld-Mott transition is related to the phase transformation of brittle materials under the influence of hydrostatic pressure during cutting. The deformation characteristic of brittle materials can be expressed in terms of strength that changes with varying pressure and consequently phase transformation. Jamieson [50] conducted the phase transformation study of germanium and silicon and found that both materials change their “gray” crystalline structure to ”white” tin structure at high pressures. Gillman [51, 52] determined that during HPPT, the change in bond angle result in the change of volume and shape in the diamond cubic lattice and result in metallization of brittle materials. Patten et al. [5] machined brittle materials and observed plastic deformation as a result of the phase transformation. They also observed amorphous phase on machined surface and within chips as a result of unloading.

The phase transformations of brittle materials procure with loading and unloading conditions. More than 10 structural phases observed during indentation and scratch test studies and SPDT of single crystal silicon [53-58] under the loading and unloading conditions. Zhang [59] reviewed the phase transformation of silicon under various loading and unloading condition during indentation, scratching, and different machining processes. Fig. 2-6 presents the silicon phases during loading and unloading conditions as a function of hydrostatic pressure.

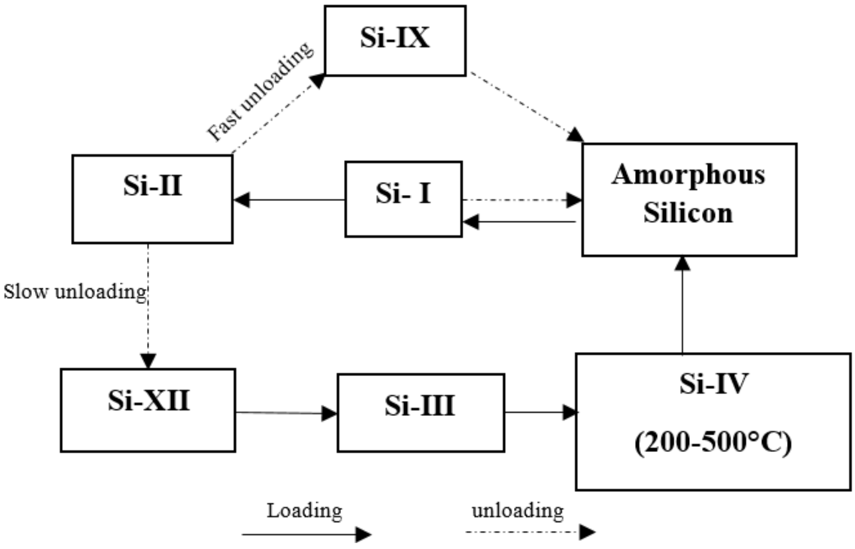

Figure 2-6: Phase transformation of silicon during loading and unloading condition

Silicon retains diamond cubic structure (Si-I) at ambient conditions with a lattice spacing of 5.430710 Å and transition of crystalline silicon transpires at ~11-12GPa into β-sn (Si-II) metallic phase [60] with associated 22% volume reduction [61]. Above 14Gpa, phase transition was found into Imma (Si-XI) at 15GPa, simple hexagonal (Si-V) at 16GPa and Intermediate phase (Si-VI) at 37-40GPa, hexagonal closed-packed (hcp) structure at 42GPa and at 78GPa transform into Si-fcc [50]. Amorphous silicon (a-Si) accompanying other silicon phases were observed in indentation and scratch test and SPDT studies. Upon unloading, Si-II phase transform back to tetragonal Si-IX phase and with further decompression into rhombohedral R8 (Si-XII) and body-centred-cubic BC8 (Si-III) crystalline phases [62-64] with 9% volume increase. At a temperature of 200-500 °C, Si-III phase transform into Lonsdaleite Si-IV [62] at slow decompression and into Si-VIII and Si-IX at fast decompression of Si-II. The transformed phase yields back to original diamond cubic structure (Si-I) with further heating above 500 °C [65]. Phase transformation of silicon directly under the tool tip varies as a function of tool geometry and loading and unloading conditions [61, 63] and phase layer thickness and position changes along the indentation or groove depth. Raman study of phase transformation of silicon is shown in Fig. 2-7.

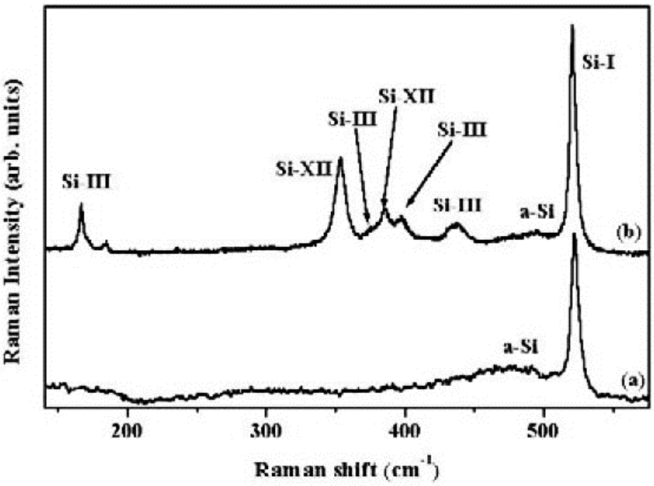

Figure 2-7: Raman spectra of silicon-phase transformation during indentation (a) For 5 steps (b) For 10 steps [58]

2.4.4 Critical depth and critical chip thickness

he critical depth is one of the criteria to identify the transition from plastic deformation to brittle fracture in materials. In indentation, the critical depth refers to the depth of penetration of indenter for crack initiation. One of the earliest work in identifying the critical depth was presented by Lawn et al. [66, 67] during the indentation study of brittle materials. They developed a mathematical relationship of material properties and critical loading condition to quantify the plastic deformation and brittle fracture zones. Leung et al. [68] conducted diamond turning to determine the critical depth of cut of silicon (111) as a function of feed rate. The surface roughness trend of machined surface of silicon with increasing depth of cut and increasing feed is shown in Fig. 2-8 [68].

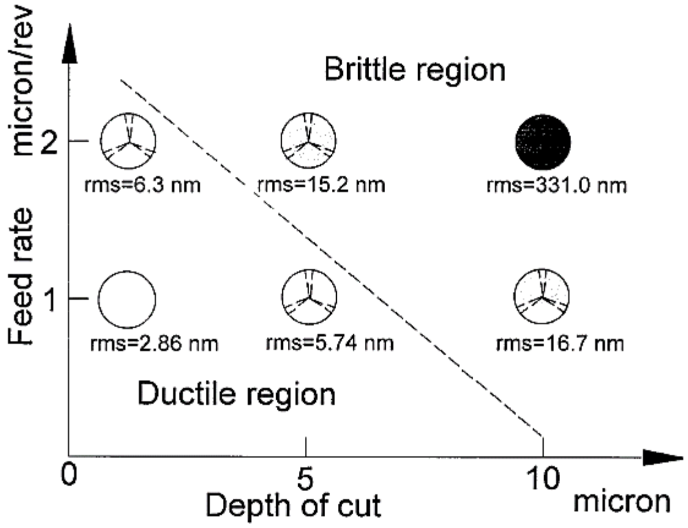

Figure 2-8: Effect of depth of cut and feed rate observed during machining of silicon [68]

Critical chip thickness refers to the threshold value of chip thickness beyond which material removal during machining changes from ductile to brittle mode. Crack or defect generation in diamond turning as a function of critical chip thickness criteria was first presented by Blake and Scattergood [9, 10]. They investigated the ductile to brittle transition along the cutting edge reliant on nose radius, feed rate and cutting depth. Fig. 2-9 shows Blake and Scattergood damage evolution criteria based on critical chip thickness. Material removal transpires in ductile mode at and near the apex of the tool turn into brittle fracture beyond certain distance z_{eff} at critical chip thickness t_c. The fracture damage initiates and propagate with the damage depth y_c penetrating into the final machined surface. For feed rate below threshold value facilitate ductile material removal and superior surface finish.

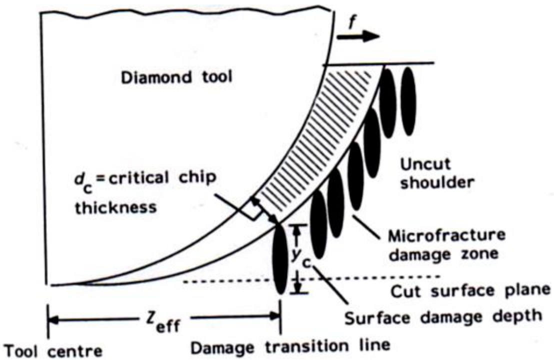

Figure 2-9: Ductile and brittle regime machining model [10]

2.4.5 Cutting parameters and conditions

Blake and Scattergood [9, 10] performed diamond turning of germanium and silicon and found the dependency of critical chip thickness on tool geometry and feed and determined a trifling effect due to cutting speed. They also derived a relation to determine the critical chip thickness (t_c) and damage depth

(y_c) from tool radius (R), feed (f) and ductile-brittle transition distance (z_{eff}) and described as [10]:

$$\frac{Z_{eff}^2 - f^2}{R^2} = \frac{t_c^2}{f^2} - 2\left(\frac{t_c + y_c}{R}\right) \qquad (2.1)$$

The crack damage depth (y_c) varies as a function of feed rate and the damage penetrate into final machined surface beyond critical feed rate.

$$f_{max} = t_c\sqrt{\frac{R}{2(t_c + y_c)}} \qquad (2.2)$$

The penetration of fracture damage into the machined surface as a function of feed rate is shown in Fig. 2-10 [69] .

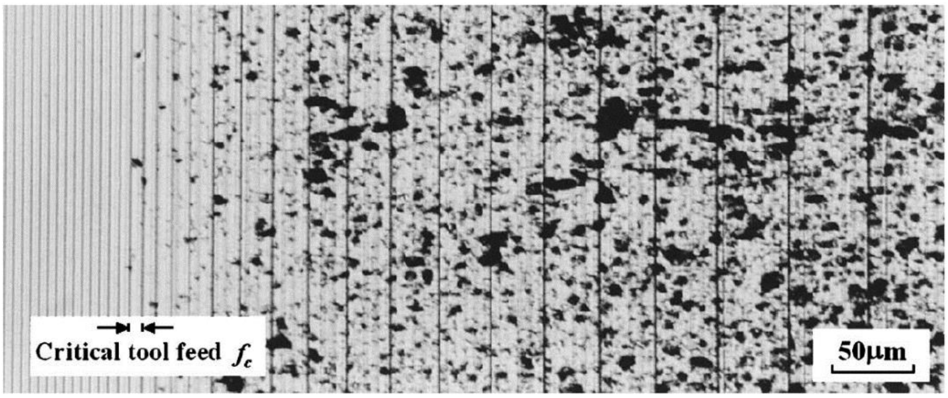

Figure 2-10: Fracture damage beyond critical feed rate [69]

2.4.6 Optimization of tool geometry

Major reported work reveals that using an accurate tool geometry, ductile mode machining of silicon exploiting HPPT can be achieved [9, 68, 70]. From the tool geometry perspective, negative rake angle tools were found to generate high hydrostatic pressure required for structural transformation of silicon ensuing brittle to ductile transition (BDT) [71]. The change in stresses using positive and negative rake angle is illustrated in Fig. 2-11. The shear and compressive stress, as well as their triggering sequence, vary with any change from positive to negative rake angle. The increase in tangential and normal contact area using negative rake angle tool facilitate plastic deformation of brittle materials.

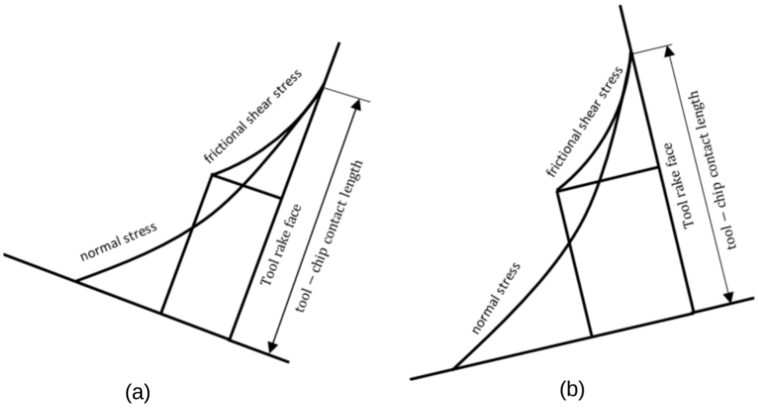

Figure 2-11: Stress distribution change from (a) positive to (b) negative rake angle

Diamond tools with negative rake angle are also assumed to provide cutting edge strength against any chipping or abrasive damage and consequently more control on an abrupt tool wear. Cutting edge sharpness of diamond tools considerably affect surface roughness and, therefore, considered also to be an important factor in achieving the optical surface quality of silicon.

The increase of critical chip thickness was also claimed to increase with an increase in negative rake angle of the tool. Blake and Scattergood [9] performed SPDT of silicon and germanium using diamond tools with rake angles of 0°, -10° and -30°. They observed an increase of critical chip thickness from 0° to -10° rake and found a sharp increase in critical chip thickness at -30° rake. Yan et al. [69] observed an increase of critical chip thickness from 0° to -40° rake angle tools. Shibata et al. [57] conducted machining of silicon using -20° and -40° rake diamond tools at 100nm and 1µm depth of cut. They found that rake angle effect diminishes at a depth of cut of 100nm and becomes prominent from 100nm to 1µm in all crystallographic orientations. Fang et al. [72] suggested the importance of effective rake angle in association with cutting edge radius and depth of cut. Using 0° rake angle and -25° rake angle tools, they observed surface deterioration for an effective rake angle of ~-60 rake using -25° tool and surface finish of 1nm using lower negative effective rake angle.

In tool geometry, cutting edge radius is also one of the most important parameters that influence the machining mechanism of brittle materials. The cutting edge radius should not be confused with the tool nose radius. The comparison of nose radius and cutting edge radius of the tool is shown in Fig. 2-12 [73].

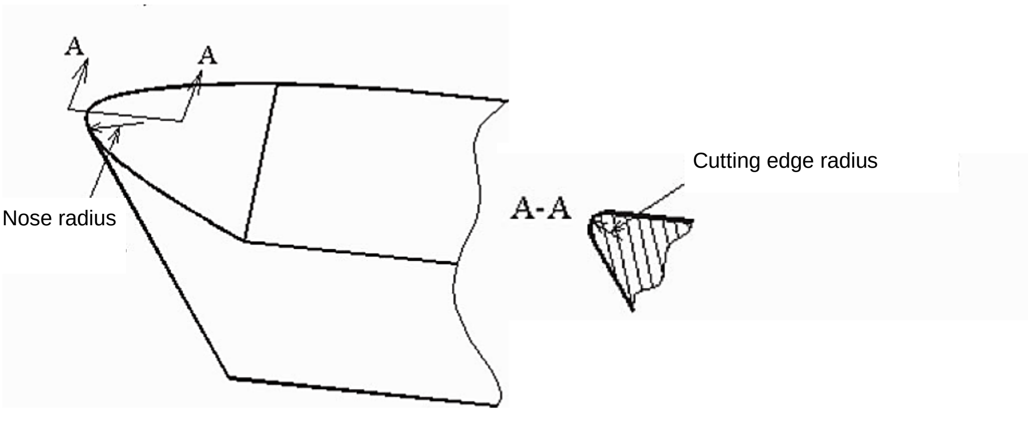

Figure 2-12: Nose radius and cutting edge radius of tool [73]

The effect of cutting edge radius in SPDT of brittle materials become prominent at nanoscale cutting and become a deciding factor of machining mechanism [74, 75]. Arefin et al. [73] studied the influence of cutting edge radius in relation to undeformed chip thickness in the experimental study of silicon. They found that there exists a critical upper bound value of cutting edge radius beyond which machining mechanism of silicon changes from ductile to brittle. Also as long as the undeformed chip thickness is less than the cutting edge radius, silicon can be machined in ductile mode. Cai et al. [75] conducted the simulation study of silicon and found that when the undeformed chip thickness is larger than the cutting edge radius, a peak deformation zone develop and expand in volume with tool motion. The tensile stress developed ahead of the zone result in crack formation. Fig. 2-13 shows the ductile and brittle mode as a function of cutting edge radius in relation to undeformed chip thickness.

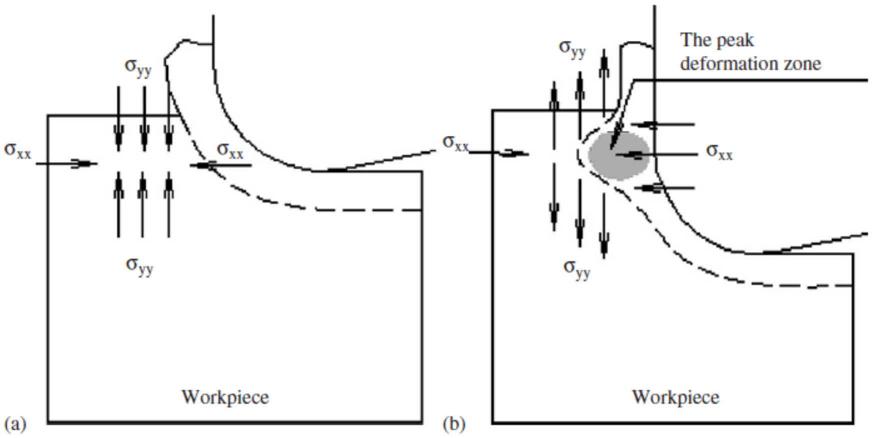

Figure 2-13: Cutting edge radius and undeformed chip thickness effect (a) ductile (b) brittle [70]

The undeformed chip thickness using round nose tools is shown in Fig. 2-14 [43]. For a very small feed rate, the maximum undeformed chip thickness d_{max} of the machined material can be measured using the following equation.

$$d_{max} = R - \sqrt{R^2 + f^2 - 2f\sqrt{2a_0R - a_0^2}} \qquad (2.3)$$

Where R is the tool nose radius, and f and a_0 are the feed rate and depth of the cut respectively. It is important to satisfy the condition $\sqrt{2a_0R - a_0^2} > f$ to accurately estimate the undeformed chip thickness using this equation.

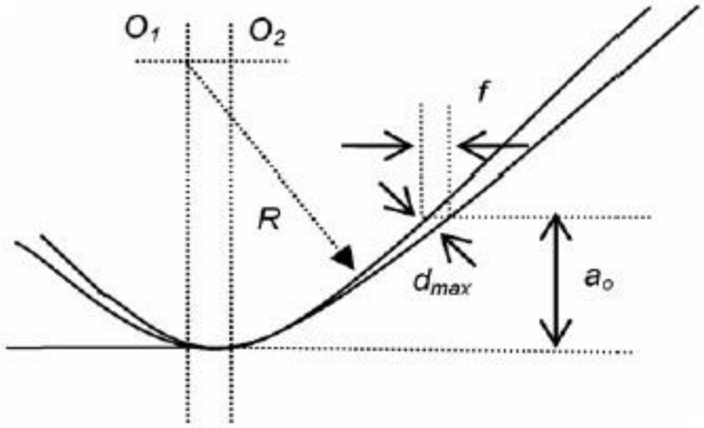

Figure 2-14: Illustration of undeformed chip thickness using round nose tool [43]

2.5 Diamond tool wear in SPDT of brittle materials

Due to its excellent material properties, single crystal diamond tools are used to achieve the high optical quality of ductile and brittle materials in SPDT processes. However, diamond tool also undergoes wear from minor to severe wear dependent on tool material, workpiece material as well as cutting conditions. Phase transformation, crack formation and material removal mechanism vary and removal rate of silicon decrease with the increase of diamond tip wear [76]. In the diamond face turning operation, even worn tool can govern ductile mode material removal of silicon conditional to required hydrostatic pressure and shear stress [55].

The type and characteristics of stone of diamond tool as well as its fabrication method can significantly influence the tool performance.

2.5.1 Diamond tool wear mechanism

Tool wear in SPDT of brittle materials is a crucial factor to achieve deterministic optical machining. Various types of diamond tool wear mechanisms have been observed dependent on the workpiece material. The wear mechanisms of diamond tools identified are adhesion and built-up edge formation, tribo-chemical wear, tribo-thermal wear, triboelectric, abrasion, micro-chipping, fracture and fatigue [44, 77-81]. Usually, multiple tool wear mechanisms in combination can be active but only one tool wear mechanism is dominant for a specific workpiece material and for a certain cutting regime.

Paul et al. [77] performed a study for diamond turnability of materials and proposed a theory that chemical tool wear is mainly caused by the presence of unpaired “d” electrons in the material being turned. They claimed that unpaired “d” electron is responsible for the breaking of tight carbon-carbon bond breaking in diamond followed by the formation of metal-carbon complex which leads to the chemical wear of diamond tools. They also determined that in the presence of oxygen, the metal-carbon-oxygen complexes can form which increases the chemical tool wear.

Wong [82] performed machining tests using a large number of diamond tools and categorised diamond tool wear into chipping, chip dragging, line effects, setting problems, normal wear, and fracture by inclusion in the work material.

Glass, silicon, silicon carbide and many other brittle materials that are used in various industries are hard to diamond turn due to their hardness, brittleness, and low fracture toughness. Cleavage and micro-chipping presumed to be the dominant wear mechanism in diamond turning glass [81]. Shear and tensile stresses induce in diamond tools could cleave diamond tool along its cleavage plane (111) or in other defected crystallographic planes. Micro-chipping occurs in accordance with the cleavage fracture**.** Other types of wear found are the combination of thermochemical, mechanical friction and abrasive wear while turning glass [78].

Cutting in ductile mode significantly reduce the brittle fragmentation of chips and results in reduced tool wear and better surface finish [81, 83]. Yan et al. [84] conducted diamond turning of silicon and found observed tool wear due to microchipping and gradual wear. Microchipping and gradual wear on the cutting edge and flank face are shown in Fig. 2-15 [84].

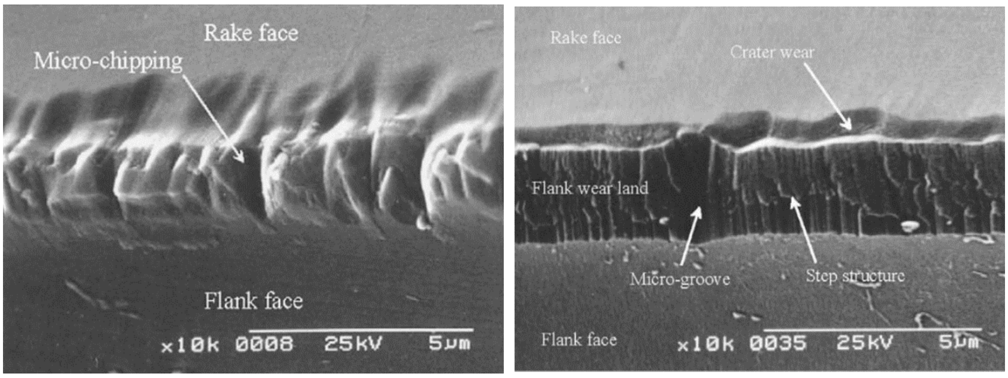

(a) (b)

Figure 2-15: Diamond tool wear (a) Cutting edge (b) Crater and flank wear [84]

Li et al. [85] performed diamond tool wear study in nanoscale machining of silicon. They observed tool wear through chipping and abrasive damage. They also observed that nanoscale grooves initiate at tool flank face. When the wear appears towards rake face, the machining mechanism changes from ductile to brittle. Fig. 2-16 show groove observed chipping and groove observed in their study.

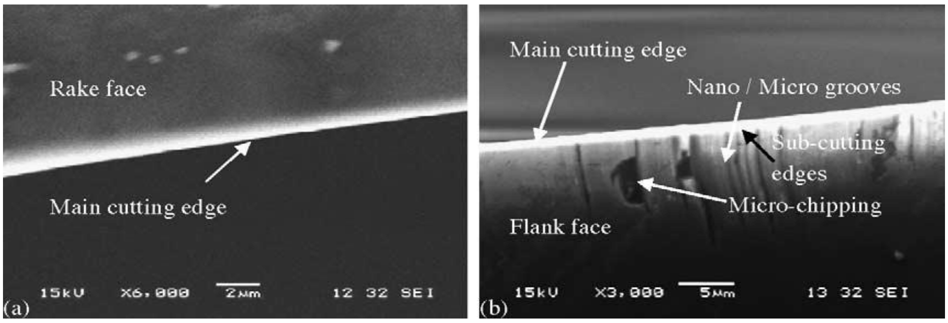

Figure 2-16: chipping and groove wear in turning silicon [85]

Cheng et al. [44] performed experimental and simulation study and suggested that high cutting temperature is responsible for diamond tool wear and thermo-chemical wear is the main tool wear mechanism in diamond turning silicon. They rejected the possibility of tool wear due to the occurrence of fracture in diamond tool as the highest stress value on the tool doesn’t increase the fracture toughness of diamond. Sharif Uddin et al. [43] observed abrasive, adhesive and thermo-chemical wear in diamond turning of silicon. They observed mainly abrasive wear on the flank face of the tool. The crater wear only appears at the higher cutting distance.

2.5.2 Methods to reduce tool wear in machining brittle materials

Zhou et al. [81] performed ultrasonic vibration assisted diamond turning of fused silica glass. The results show that ultrasonic vibration method significantly reduces the cleavage and micro-chipping of diamond tools, suppresses brittle fracture and improve surface finish. They suggested that due to the reduction of effective contact time between the cutting edge and workpiece and enhanced lubricant supply to the machining zone in ultrasonic vibration machining, cutting temperature and average process forces can be reduced. This reduction restrains the crack initiation and its propagation.

Zareena et al. [79] experimentally proved that tool wear and surface quality of material can be significantly improved if diamond tools are coated with Perfluoropolyether (PFPE) polymer. They diamond turned commercial pure titanium (CP –Ti) and Ti-6Al-4V alloy with the PFPE coated diamond tools and with non-coated diamond tools. The results demonstrated that PFPE films can substantially reduce the value of coefficient of friction between the tool and workpiece which in turn improves the diamond tool wear and surface roughness of titanium.

Micro/nanostructures have also been generated on cutting tools to improve the anti-adhesive effect, improve cutting performance, as well as to reduce friction between the tool and workpiece material in order to avoid tool wear and breakage [86-88]. Structured surfaces are of particular importance in MEMS/NEMS, semiconductor industries, and in microfluidics. Micro and nanostructured surfaces are playing a critical role in making MEMS systems more compact and economical.

Another approach to machine brittle materials in ductile mode is the use of the laser during the machining process. Micro-laser assisted machining (µ-LAM) has been verified to achieve ductile mode machining of brittle materials. Ravindara et al.[89] conducted micro-laser assisted scratch test on single crystal silicon. They found that micro-laser assisted machining help in thermal softening of the silicon results in material removal by plastic deformation and reduced abrasive tool wear. Mohammadi et al. [90] conducted µ-LAM of silicon (111) and found that surface roughness of an unpolished surface with a starting surface roughness of 770 nm can be improved to 3.2 nm using this method. Using heat-assisted and vibration-assisted machining, the critical depth of cut can be increased [83].

Various machining methodologies have been exploited to improve ultra-precision techniques to achieve reduced tool wear and improved surface finish. Table 2-2 lists few of the developed methodologies successfully tested against some of the hard and brittle materials.

Table 2-2: Techniques to improve machining mechanism and tool wear

Conventional Machining	Improved technique	Methodology	Workpiece Material	Tool material
Diamond turning	Swivel machining	Tool rotation	SiC	diamond [91]
Diamond turning	Surface modification	Amorphous structure on surface	SiC	diamond [92]
Micro-milling	Micro-milling tool development	Structures on cutting edges	Ceramics	diamond [93]
Turning, milling, drilling, grinding	Cryogenic machining	Liquid nitrogen [94], Liquid CO_2 [95]	Titanium, Tantalum, Hardened steel	CBN,PCBN [96]
Turning, drilling, grinding	Vibration-assisted machining	Hydraulic vibrator, piezo and magneto actuator, 1-D & 2-D VAM [97]	Mild steel, Hardened steel	Carbide [98], diamond [99]
Turning, milling, drilling	Laser Assisted machining	CO_2Laser, Nd:YAG [100]	Tool steel, titanium, silicon, SiC	CBN [101, 102]**,** diamond [90]

2.6 Summary

A critical literature review of machining of brittle material was presented in this chapter. It is evident that machining of brittle materials is a complex process that requires both qualitative and quantitative understandings of material removal, process conditions and tool wear.

SPDT process has been established as one of the most efficient ultraprecision machining methods to produce optical quality functional surfaces on hard and brittle materials. It was also identified that silicon undergoes structural transformation into multiple phases under the influence of varying hydrostatic pressure. From the tool geometry perspective, the cutting edge radius and tool rake angle are the two important factors that influence the ductile regime machining of silicon and other brittle materials. Cutting parameters including critical undeformed chip thickness, cutting speed, feed rate and depth of cut are the most important parameters need to be optimized for improved machining quality.

Chapter 3- A review of research on the finite element simulation of cutting process

3.1 Introduction and background

Machining is a complex phenomenon based on derivative criteria of friction, cutting temperature, adiabatic shearing, stresses, strains, and strain rate. The complexities due to high cutting speed conditions impede to assimilate in-situ deformation characteristics of workpiece and tool materials under variable cutting conditions. The designed experiments and predictive modelling have been adopted in the past few decades to understand the convoluted phenomenon of machining mechanism in a simple and cost-effective manner. These models can be expressively classified based on analytical, experimental, numerical, and empirical as well as hybrid modelling studies [103, 104]. The development of machining techniques to the current stage of conventional as well as ultra-precision micro/nanoscale is highly dependent on the wide range of advanced predictive machining models.

With the development of computer power, numerical analysis has emerged as a powerful tool to investigate a wide range of manufacturing processes and provide a rational insight into machining response behaviour of materials. Numerical simulation methods have evolved to predict the machining behaviour of metals, polymers, ceramics, composites and many other materials. The capability of the numerical methods to approximate the material behaviour from conventional to micro and nanoscale machining is the key development of numerical methods. Two widely adopted numerical simulation methods for machining are finite element method (FEM) based on continuum mechanics and molecular dynamics (MD) method based on discrete mechanics. Fig. 3-1[105] presents the capability of these numerical methods to machine materials from micro to nanoscale.

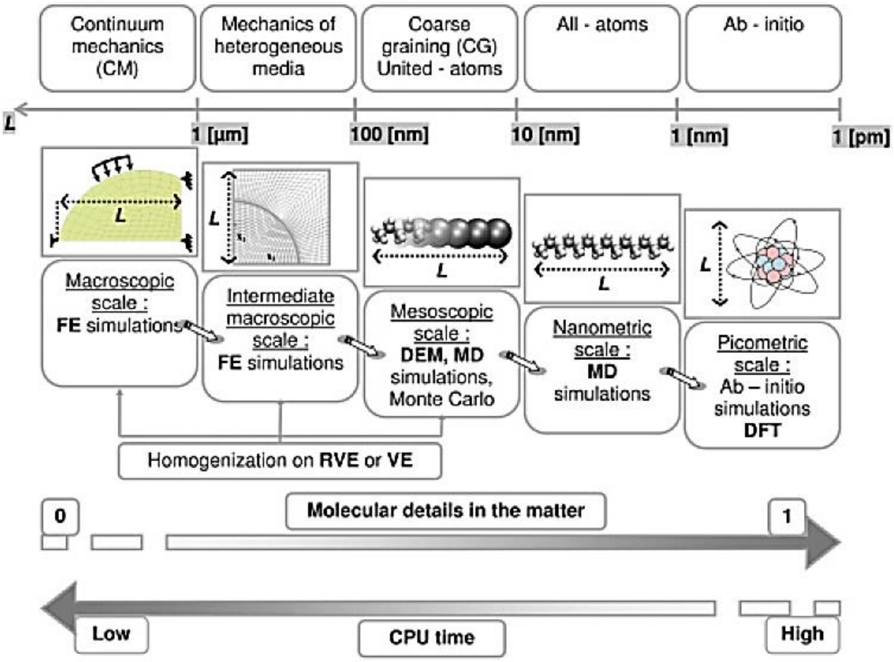

Figure 3-1: Micro and nano-scale modelling capabilities of numerical methods (VE=volume element, RVE= Representative volume element. [105]

3.2 Finite element simulation

The implementation of FEM for machining simulations started in the early 1970s when FE machining simulations were performed using user-defined FE codes. Later with the development of commercial software, machining studies were performed using general-purpose FE codes including NIKE 2D [106-109], Abaqus [110-115], LS-DYNA [116, 117], ANSYS [118] and Marc [107, 119, 120]. FEM has evolved as one of the most prevalent numerical techniques in cutting analysis. It has a significant contribution to machining process by the optimization of cutting parameters exploiting high array testing of input parameters. The qualitative and quantitative analyses of machining have been conducted for the detailed analysis of chip morphologies, cutting forces, temperature, stresses and strains and other output variables. Machining simulations analogous to any other simulations adopt input parameters that define the implicit functional relationship in the explicit form of output variables. The FE machining studies are based on variety of analyses including tool geometry [114, 121-125], machining parameters and conditions (cryogenic, laser/water jet-assisted, etc.) [126-133], crystal orientation [134, 135], tool wear measurement [123, 136, 137], chip separation criteria [138-142] and meshing and remeshing strategies [110, 143-145]. The constitutive material models with different numbers and range of parameters were evaluated for a wide range of materials. Evaluation of input parameters using experimental studies in combination with numerical studies provides an improved understanding of machining mechanics of materials [146, 147]. Fig. 3-3 shows a list of input variables evaluated in experimental and simulation conditions for the required output solution variables.

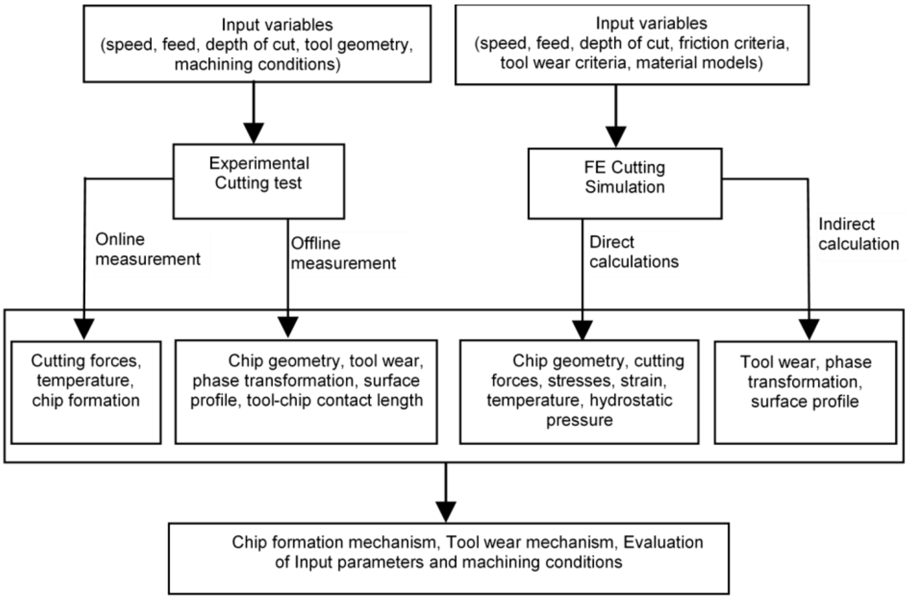

Figure 3-2: optimization of machining using experimental and FE cutting simulation

3.3 Finite element formulations

The correlation of continuum and computational mesh of the problem domain is fundamentally adopted based on the type of continuum and its dynamics as well as the deformation scale. The three main relative motion algorithms or numerical formulations developed and also adopted for machining simulations are the Lagrangian approach, Eulerian approach, and Arbitrary Lagrangian Eulerian (ALE) approach.

3.3.1 Lagrangian formulation

The lagrangian approach has widely been adopted in cutting simulations due to its computational efficiency and tendency of natural deformation behaviour. In Lagrangian approach, both elements and nodes of the mesh remain attached to the material and it is easier to apply boundary conditions and track free surfaces. Lagrangian mesh deforms in replication to material deformation in such a way that position of mesh nodes relative to material points remains fixed. The Lagrangian approach in machining simulation has been extensively exploited since one of its earliest implementation in 1973 by Klamecki [148] until recently with or without adaptive remeshing [107, 149-154].

One of the limitations of Lagrangian approach is severe mesh distortion due to large deformations during cutting simulations. The excessive element distortion at tool-chip interface degrades results accuracy and consequently results in the termination of simulation. With the increasing hardness of the material, chip formation can only be achieved by node separation using adaptive meshing or chip separation methods. Also, when using negative rake angle tools and round edge tools, the node separation methods also suffer performance failure. Further categorization of Lagrangian approach is based on the interrelation of nodes and classified as mesh-based and mesh-free methods.

3.3.2 Eulerian formulation

The Eulerian approach has also frequently been adopted in machining simulations of metals. In the Eulerian formulation, mesh remains fixed in space and material is allowed to flow through the mesh during deformation. Since the mesh boundary nodes and material boundary nodes can’t bind to coincide, it is difficult to model free boundary and interface conditions and it becomes difficult to track free surfaces. When using Eulerian approach for cutting simulation, it is required to define chip geometry beforehand.

The pioneer works of Eulerian approach in cutting simulation was done by Usui et al. [155-157]. Carrol and Strenkowski [158] adopted Eulerian formulation in viscoplastic cutting simulation and their model is known as Eulerian cutting model. They also developed an orthogonal cutting model for single point diamond turning process [138]. Although they found the model more accurate and computationally efficient than updated Lagrangian approach, it was difficult to predict final chip geometry. Later Strenkowski and Moon [159, 160] improved the model by employing a free surface algorithm to determine final chip geometry and tool-chip interface length. A good percentage of FE machining simulations work using Eulerian formulation has been conducted to evaluate chip geometry and optimization of many other machining variables [124, 161, 162].

The Eulerian approach offers a solution to the mesh distortion exploiting fixed reference frame and predefined chip geometry is required to simulate the cutting process. Since the geometry of the chip influence other machining variables including friction, temperature and cutting forces; an improper predefined chip geometry leads to misleading results. The Eulerian approach is more appropriate for fluid simulations or in the processes where material boundaries are already known and described. The approach has been successfully adopted in forging and extrusion processes.

The Eulerian approach has some desirable features over Lagrangian approach, as it doesn’t suffer from mesh distortion issue and, therefore, no remeshing is required. It also offers direct steady-state solutions without undergoing a transition from incipient to steady-state conditions for accurate solutions and therefore computationally less expensive. Figure 3-3 [163] presents the plastic flow in Eulerian and Lagrangian formulation during cutting.

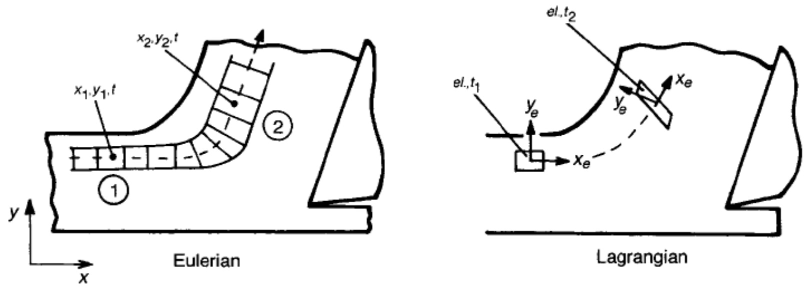

Figure 3-3: Plastic flow in Eulerian and Lagrangian formulation [163]

3.3.3 Arbitrary Lagrangian Eulerian formulation

The ALE approach exploits the benefits of both classical Lagrangian and Eulerian formulations. ALE offers coincidence of boundary nodes with material boundary while adjusting interior nodes to reduce mesh distortion. In cutting simulations, ALE maintains the Lagrangian capability of constrained mesh motion at free boundaries while maintaining the Eulerian behaviour during chip formation in the high deformation zone. Retaining the capabilities of both the approaches in ALE formulation resolves the problem of mesh distortion along with exploiting natural chip formation without predefining chip geometry. The implementation of ALE approach involves the adoption of user-defined mesh regularization or mesh-adaptation strategies [164]. The mesh regularization techniques concerned with keeping mesh practically regular during high deformation, by continuously updating nodal coordinates using displacement or velocity parameters. The estimation of a solution of problem domain using ALE approach can be achieved either by concurrently solving all non-symmetric equations or by using ALE operator split method to decouple

Lagrangian equations [165]. ALE with mesh adaptation approach involved localized mesh refinement within high deformation zone and remeshing.

Many researchers used ALE formulation in machining simulations to evaluate ALE formulation for cutting simulations as well as in different machining analysis including chip formation study, the effect of tool geometry, and evaluation of input variables [142, 165-170]. ALE approach can be employed with Lagrangian boundaries [170, 171] as well as Eulerian boundaries [114, 169] in chip formation zone. Fig. 3-4 [170] shows ALE cutting models with Eulerian and Lagrangian boundaries.

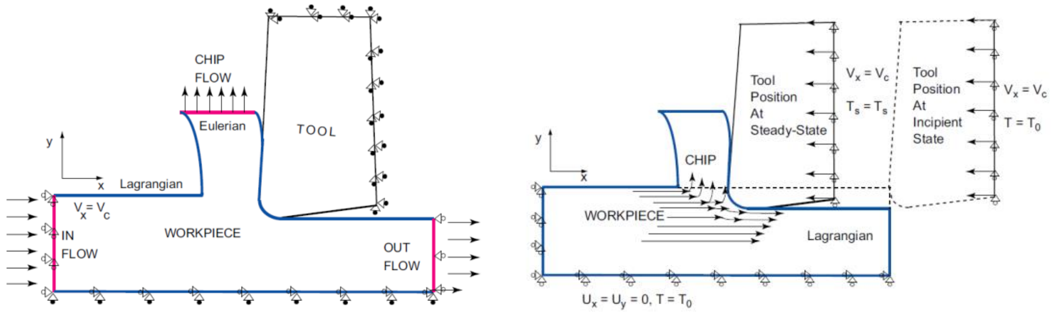

Figure 3-4: ALE formulation with Lagrangian and Eulerian boundaries (left), Lagrangian only (right) [170]

When using ALE formulation with Eulerian boundaries, the friction criteria at tool-chip interface don't significantly influence the output variable when compared the model results based on ALE formulation with Lagrangian boundaries[170]. ALE formulation with predefined chip shape has also been studied by many researchers. Movahhedy et al. [142, 166] and Olovsson et al. [167], evaluated the performance of ALE in 2D cutting simulations and found that no chip separation criteria is required using this approach and results can be better predicted than Eulerian. Various tool wears numerical simulation studies are also based on ALE formulation [172-175].

3.4 Particle based formulations

Particle methods were developed in an effort to approximate the problem domains involving interaction of fluids and solids. Difficulties involved in using Eulerian and ALE approach to simulate interaction of the fluid with different multiple bodies lead to finding the solution to use Lagrangian formulation. Particle methods, in general, can be classified as mesh-based or meshless methods. In meshless methods, the definition of shape functions is only dependent on node positions and no connection is required between the nodes of the problem domain. Also, all the physical and mathematical properties including density, velocity, temperature, etc. are assigned to the node itself rather than mesh elements. In mesh-based particle methods, nodes at the intersecting elements behave like particles and move during deformation with their physical properties. The remeshing occurs according to the new position of the nodes during each time step. Thus, mesh-based formulation exploits the features of meshless approach and FEM.

Various particle based methods have successfully been adopted in machining simulation including SPH [176], material point method (MPM) [177], particle finite element method (PFEM), and Finite point-set method (FPM). The main differences between these particle methods are the mesh features and type of interaction between the particles as well as the calculation of the relative position of a particle of interest and its neighboring particles.

When comparing performance in machining applications, Lagrangian mesh-based approach has been well researched compared to particle based formulations in simulations of machining of ductile materials [107, 149]. However, simulations of hard and brittle materials such as silicon and silicon carbide using mesh-based Lagrangian method is difficult and becomes impractical when using higher negative rake angle tools. This is not only because the pressure-dependent machining mechanism varies as a function of tool geometry and machining conditions; but also the true critical parameter values of physical and geometrical criteria for crack formation [178-180] along with pressure-dependent brittle damage models are difficult to be identified. Also, due to the negative rake angle of the tools, implementation of crack formation criteria along a dedicated layer becomes impractical.

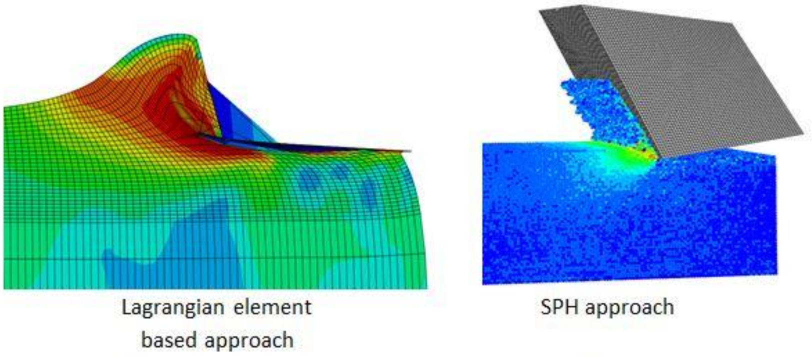
Lagrangian element based approach

SPH approach

Figure 3-5: Mesh distortion in mesh-based Lagrangian approach (left) SPH approach (right)

Due to the mesh-less nature and suitable particle connectivity, particle based methods offer continuous and discontinuous material removal due to plastic deformation and brittle fracture respectively without any separation criteria.

Fig. 3-5 illustrates the mesh distortion issue in the cutting process using FEM and natural chip separation in SPH.

In general, all the meshless methods offer common advantages and disadvantages over classical FEM. The main advantages of these methods over FEM include: (1) Meshless methods are based on Lagrangian formulations and, therefore, offer better approximation in cutting simulation problems than both Eulerian and ALE (2) No artificial physical or geometrical separation criteria is required for chip formation as required in Lagrangian mesh-based FEM (3) Remeshing is not required using mesh-free approach. The main disadvantages include: (1) Mesh-free methods are computationally expensive than conventional FEM due to high number of neighboring particles (2) Meshless methods are not fully developed for all type of analysis for cutting simulation processes and are currently in the development stage (3) Meshless methods are less sensitive to small deformations in comparison with FEM and, therefore, less efficient than FEM for small deformation problems.

3.4.1 Particle Finite Element Method (PFEM)

The PFEM method was developed to solve fluid-structure interaction problems including dynamic free surfaces, flow separations, collapse situations and other general fluid mechanics problems [181, 182]. The basic modelling of fluid and solid domains in PFEM is based on updated Lagrangian formulation. The discretization of fluids and solid domains is done by FEM using mesh generation based on extended Delaunay tessellation (EDT) [183]. The key feature of PFEM method is the very fast mesh generation at every time step based on node position in space using EDT method. The PFEM method adopts MFEM (Meshless Finite element method) [184] shape functions to solve incompressible Navier-strokes equations to evaluate forces on each particle.

The implementation of PFEM method later extended to evaluate surface wear situations [183], in the analysis of fluid-multibody interaction [185], modelling of bed erosion in free surface flows [186] and many other fluid dynamic problems. The application of PFEM for cutting process simulation was first proposed by Oliver et al. [187]. Later Carbonell [188] used this approach to model tunnelling process and rock cutting tool wear. Sabel et al. [189, 190] performed the tensile test and cutting simulations tests using PFEM and compared the results with FEM simulations. They found the approach useful for machining simulations. Rodriguez et al. [191] performed cutting simulations to evaluate PFEM as an efficient numerical simulation tool for cutting process. They conducted orthogonal cutting of 42CD4 steel using PFEM and analyzed output variables including cutting forces, stresses, strains and temperature and compared the results with experimental results as well as numerical cutting simulation results using Abaqus, AdvantEdge, and Deform. Furthermore, they performed sensibility analysis to geometric and cutting conditions of PFEM usability using Design of Experiments (DoE) methodology. They found some results in good agreement with experimental and other numerical simulation studies and some discrepancies. They concluded PFEM as an efficient approach which could approximate better solutions to cutting simulation problems and, therefore, required further development and evaluation for different machining processes.

3.4.2 Finite point-set Method (FPM)

The FPM developed by Fraunhofer Institute for Industrial Mathematics (ITWM) is a mesh-free numerical method to simulate mechanical and fluid dynamics problems [192]. The FPM is based on the law of conservation of mass, energy and momentum and exploit finite difference method (FDM) and moving least square method to solve differential equations and approximation of field value and derivatives respectively [193]. In FPM, similar to SPH approach, each particle produces a sphere of influence and interacts with other neighbouring particles within a smoothing length. Any undesired particle accumulation or cavities can be avoided by deleting or generating particles using advanced particle management algorithm. This method was successfully employed for the cutting simulations of medium carbon steel AISI 1045 and nickel-based alloy Inconel IN718 for continuous and segmented chip formations and compared with experimental and DEFORM simulation results [193, 194]. Although some output variable results were found in good agreement with experimental and other simulation studies, certain discrepancies were observed in thrust forces, shear angle, temperature and chip geometry. The method is still in the development stage and not much further work is published using this approach.

3.4.3 Discrete element method (DEM)

Another popular addition to meshless methods is DEM with a wide range of applications in many different fields. The DEM was originally developed by Cundall in 1971 to solve geomechanics problems [195] and since then gradually and continuously evolved through various different development stages. The DEM model consists of discrete or detachable solid rigid particles initially glued together. The particles can be of different 2D or 3D shapes and sizes including circles, spheres, triangles polygons, ellipses [183]. The contact forces between the particles are governed by relative displacement based on force-displacement law [196].

One of the earliest applications of DEM in orthogonal cutting simulations was performed by Fleissner [197] using spherical particles. Qui et al. [198] performed indentation and 2D and 3D cutting simulation to investigate machining mechanism of glass and tool geometry effect. Although the authors claimed the efficiency of DEM approach to simulate machining processes, the results were not compared with any experimental study or other established numerical simulations approach. Tan et al. [196, 199] employed DEM to investigate crack initiation and propagation in Al_2O_3 and SiC at micro-scale and compared the results with experimental studies. Lliescu et al. [200] performed an orthogonal cutting simulation of carbon fibre reinforced polymer. Eberhard and Gaugele [201] performed an orthogonal cutting simulation of steel and aluminium using DEM and compared with experimental results. However, the results obtained were dissatisfactory in terms of chip geometry and cutting forces. They also pointed out the dependency of material model parameters on particle size, geometry, and arrangement. For different geometric model, same material parameters cannot be valid.

3.4.4 Smoothed Particle Hydrodynamics (SPH)

SPH is the earliest developed and most frequently adopted method for machining simulation among meshless particle methods. SPH approach was first developed by Gingold and Monaghan in 1977 [176] for astrophysics applications.

In SPH formulation, particles interact with each other based on defined constitutive equations. SPH has successfully been exploited in metal forming [202] , metal cutting [116, 134, 203], indentation [204], fracture mechanics [205], geo-mechanics [206] as well as in structural mechanics [207] studies.

In comparison with FEM, SPH approach is found less efficient in studying processes with tensile instability [208, 209] or small deformation processes. Nevertheless, it has been found more effective to study large deformation processes than lagrangian mesh-based approach. SPH approach has also been found to perform in an analogous manner to FEM following sensitivity analysis of particle resolution, mass-scaling and better than FEM in interface friction criteria [210]. In metal cutting processes, SPH method was used for studying chip formation of soft metals such as copper [134, 211], aluminium [203, 212] as well hard materials such as titanium alloys [213] and brittle materials [214]. Limido et al. [116] conducted a comparative study of chip morphology of aluminium alloy and steel using 2D SPH approach, classical lagrangian FEM, and experimental approach. They found realistic chip formation and proportional cutting forces using SPH approach for both materials. Madaj and Piska [203] found a good correlation of chip geometry in experimental and SPH simulation of aluminium alloy while investigation the effect of material model parameters and particle density. Calamaz et al. [215] employed SPH approach to understanding the effect of tool wear on the variation of chip formation of titanium alloy Ti6A14V and experimentally validated the results.

Table 3-1: Performance comparison of FEM approaches for machining studies

Formulation	Type	Advantages	Disadvantages
Lagrangian	Classical FEM	Better results approximation,	Chip separation required, mesh distortion, difficult to mesh complex geometries,
Eulerian	Classical FEM	No chip separation required, direct steady-state chip conditions, computationally efficient	Required predefined chip geometry, difficult to locate free surfaces
ALE	Classical FEM	Combine features of Lagrangian and Eulerian, avoid mesh distortion,	Computationally expensive, difficult to apply for brittle materials, remeshing required in extreme deformation, suffer error in history of state variable, inefficient in small deformation areas
SPH,DEM,FPM (Lagrangian)	Particle (meshless)	Particle based (no mesh distortion), better interface friction criteria, Ideal to simulate brittle behaviour	Not suitable for smaller deformation, suffer tensile instability,
PFEM (Lagrangian)	Particle (mesh-based)	Use features of particle and mesh-based approach, no chip separation criteria required, new mesh adjustment according to node positions,	Computationally expensive, limited performance evaluation

3.5 Finite element simulation of machining process

In machining, dependent on the workpiece and tool material and cutting conditions, cutting temperature could rise up to 1500°C or more, strain in the range 1-5 and strain rate exists in the range of (10^3 to 10^6) s^{-1}. Although FE simulations of machining processes encompass mechanical and coupled thermo-mechanical analysis, thermal effects along with mechanical effects define true machining behaviour. The FEM ability of coupled mechanical-thermal process simulation defines interdependence of perceptible and imperceptible elements of the mechanical and thermal processes. The Design of Experiments (DOE) approach using Taguchi method or Response Surface Methodology (RSM) adopted in designing experimental machining [149, 216-219] can also be employed for the optimization of FE machining process. However, the major part of FE machining simulations is based on general simulation approach without employing any design methodology.

Finite element simulations of machining processes involve simulations of turning [138], drilling [220, 221], milling [165, 222-224], grinding [225, 226] along with other machining processes [107, 227], this study deals with investigation of basic cutting methodology in SPDT process with wedge shape tool adopted in these machining operations.

3.5.1 Finite element machining models

The pioneer studies of cutting simulation were mainly focused on two-dimensional orthogonal models. The FE simulations of three-dimensional models increased with the development of high computational power and robust solvers [228] as well as strategies to reduce the computational cost [229, 230]. FE cutting simulations are based on orthogonal and oblique cutting models. In orthogonal cutting, the cutting edge of the tool is perpendicular to cutting direction. In oblique cutting, the tool cutting edge is inclined at an acute angle to the direction of the tool. Fig. 3-6 shows the chip formation in two models. Although most of the machining processes are based on oblique cutting, the major part of FE cutting simulations is based on orthogonal cutting. The oblique cutting models [228, 231-234] have also been studied but their percentage is quite low due to complexities involved in chip formation and distribution of solution variables. These two cutting models produce different chip geometry, chip direction, and cutting forces.

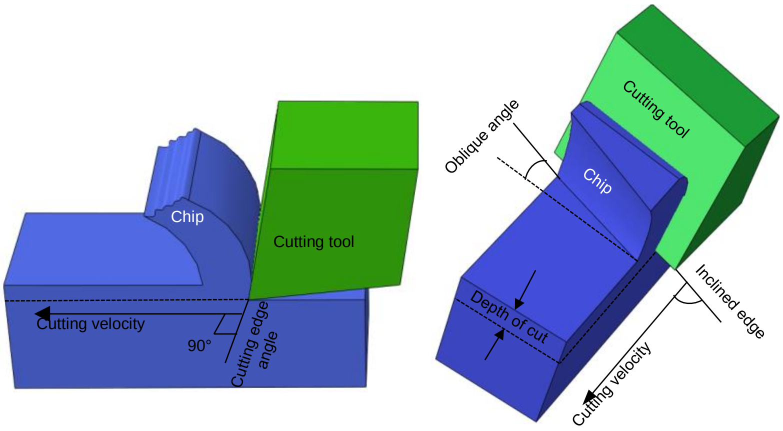

Figure 3-6: Orthogonal and oblique cutting models

In the experimental and mathematical analysis, the development of material separation or chip formation is analysed in three deformation zones. These zones are identified as primary shear zone (PSZ), secondary deformation zone (SDZ) and tertiary deformation zone (TDZ). The PSZ encompass from tip of the cutting tool to the area/point of the free surface where deformed chip transforms into the undeformed chip. The PSZ encompass shear plane or zone and major material shear deformation realize within this zone. The SDZ embrace along the rake face of the tool from the point above the tooltip to the contact length. The TDZ lies from under the tool tip along contact length towards the flank side of the tool. The tool-chip contact area during chip formation is divided into two regions known as sticking region and sliding region. Fig. 3-7 presents the schematic diagram of three deformation zone and sticking and sliding regions.

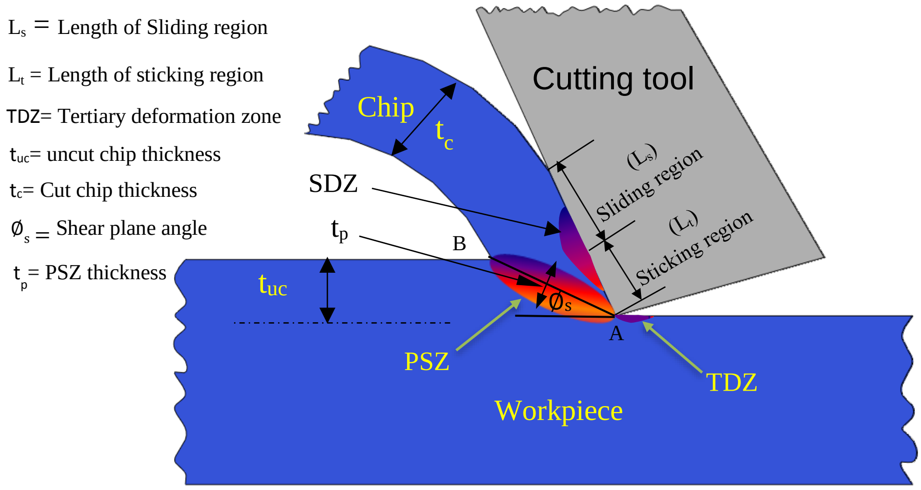

Figure 3-7: Illustration of chip formation and deformation and tool-chip contact regions

3.5.2 Defining parts geometry, properties, and contact

Regardless of modelling and analysis capabilities of FE software, a typical FE machining simulation involves modelling of tool and workpiece geometries, assigning material properties, meshing the parts, defining tool-workpiece contact and selecting the output variables according to the machining analyses. Dependent on the FE software, the parts geometries can be sketched, loaded from existing database or imported from other modelling software. In machining simulations, the tool can be modelled as rigid or deformable body whereas it is required to model workpiece as a deformable body. The performance of FE machining model and to accurately predict the true material response behaviour of the deformed material is highly dependent on assigning the appropriate material properties with plasticity and damage models. The material properties are required to be defined related to the material model. For the modelling of mechanical analysis, the mechanical properties along with elasticity and plasticity behaviour are needed to be defined. The properties including thermal conductivity, specific heat, and thermal expansion are required to be defined while performing coupled thermo-mechanical analysis.

The contact modelling of tool and workpiece is the most important factor that governs the accuracy of chip formation. A master-slave approach has frequently been adopted [235] in which master surface and slave surface are in contact with each other. In principle, rigid surfaces or harder materials are generally considered as master surfaces and deformable or softer bodies as slave surfaces. This selection is important since master surface can penetrate into slave surfaces and reverse is not allowed. Fig. 3-8 presents an example of the penetration of master surface into slave surface.

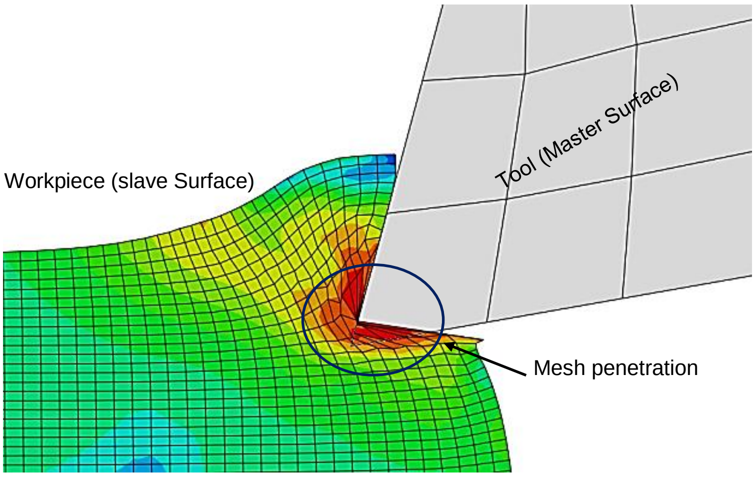

Figure 3-8: Penetration problem of master surface into slave surface

Nodes or surface contacts can be defined between the tool and workpiece surfaces dependent on formulation and cutting conditions [236]. The friction models as well as tangential (frictional) and/or normal contact behaviour with/without heat generation can be selected dependent on the available model in employed FE software. Kinematic or penalty contact method with finite or small sliding can be applied to represent tool-workpiece contact [170]. In order to simulate the chip separation, it is important to define the contact at the internal nodes rather than only on the external surfaces of the workpiece.

3.5.3 Chip separation criteria

The most fundamental and complex phenomenon of machining is controlled material removal known as chip formation, with coincidental physical and/or chemical changes. The three main chip morphologies researched in 2D and 3D FE cutting simulations of metals are continuous chips, discontinuous or broken chips and segmented or serrated chips. The final geometry (shape, length, thickness, width) of all these chips is dependent on employed FE formulation (element-based, particle-based, ALE etc.), mesh quality (element type, density, orientation, etc.), chip separation criteria, and cutting conditions (speed, feed, depth of cut,). In general principle, continuous chips are obtained by plastic deformation without fracture in the form of a coil or slightly curved form, dependent on material ductility [237]. However, FE cutting simulations are based on two conflicting theories for the initiation of continuous chip formation. One theory of inception of chip formation is based on crack generation ahead of the tooltip and its propagation with the cutting speed [238]. The other theory doesn’t support any crack formation ahead of the cutting tool tip [144]. Discontinuous chips are mainly obtained by brittle fracture (removal by cracks) or chip breakage in the secondary deformation zone. These chips are obtained in completely broken segments of different shapes and sizes and generally formed in machining of brittle materials. Serrated chips appear in segments loosely attached to each other in the saw-tooth form on the free surface of chips. These chips are obtained by the fluctuation of high shear strain and low shear strain and are normally obtained in hard and brittle metals.

Due to fixed reference frame, no chip separation criterion is required when modelling using Eulerian approach. However, due to free material flow through the mesh, predefined chip geometry is required to be defined. When using Lagrangian approach, the separation of chip mesh from the workpiece mesh undergoes high distortion due to large deformation conditions in cutting. In order to resolve Lagrangian mesh distortion during cutting, various chip separation criteria have been developed to facilitate material removal from the workpiece. The classification of these separation criteria is based on physical and geometrical parameters.

3.5.3.1 Physical separation criteria

One of the earliest works in the development of chip separation methods to achieve chip formation was done by Strenkowski and Carrol [106, 138]. They developed chip separation criteria based on the effective plastic strain. In their work, chip separation from workpiece was meant to take place once the value of effective plastic strain at nodes ahead of cutting edge exceeds predefined threshold value. The effective plastic strain threshold value was found to influence the residual stresses and chip geometry. The value found during their study lie between 0.4 to 0.65 dependent on the cutting conditions.

Later various researchers proposed chip separation criteria based on different other physical parameters. Lin and co-authors [139, 239, 240] proposed chip separation criteria based on strain energy density. Zhang [141] used normal failure stress separation criteria while investigating work hardening effect in elastic-perfectly plastic and elastic-plastic with work hardening constitutive models. Hillerborg et al. [241] proposed critical fracture energy required to open a crack and stresses for the evolution of cracks. Hashemi et al. [242] developed crack initiation algorithm for chip separation and segmentation using principle stress criteria as a function of fracture strength. In their work, when the value of principle stress at nodes reaches predefined critical value, crack initiated ahead of the tool tip. Owen and Jr [243] investigated chip formation in high-speed machining and employed equivalent plastic strain and uncoupled integration of Lemaitre ductile damage model [244]. Chen et al. [111, 245] proposed energy-based ductile failure criteria based on equivalent plastic strain and element characteristic length along with shear damage criteria for the chip formation. Ducobu et al. [246] proposed temperature dependent tensile failure criteria based on eroding element method.

Although all these criteria were successfully adopted by later researchers [128, 179, 242, 247-250] the criteria was also reproached as the values of these physical parameters significantly varies with cutting conditions, tool rake angle, cutting speed and feed [141].

3.5.3.2 Geometrical chip separation criteria

The earliest chip separation criteria based on geometrical parameter was adopted by Usui and Shirakashi [140] to resolve mesh distortion during chip formation. The general approach in the geometrical criteria is based on failure at the critical distance between the nodes present at the line within dedicated partition layer. Fig. 3-9 illustrate geometric separation criterion in which chip formation takes place with the separation of the nodes. In this model, when distance D between the tool cutting edge at point (d) and the workpiece node (point $H_{1,2}$) immediately ahead of the tool become less than the predefined threshold value, node separation take place. It is also required that the value of critical distance D must be small enough to produce chip formation in a continuous mode as well as the value should be optimal to predict true deformation behaviour. Although the implementation of geometrical criteria is simple in machining simulations, in order to maintain the chip separation direction, there is a need to introduce a predefined separation line to separate linked elements of workpiece and chip. This parting line limits the simulation model to exploit only sharp edge of tools to integrate with the parting line.

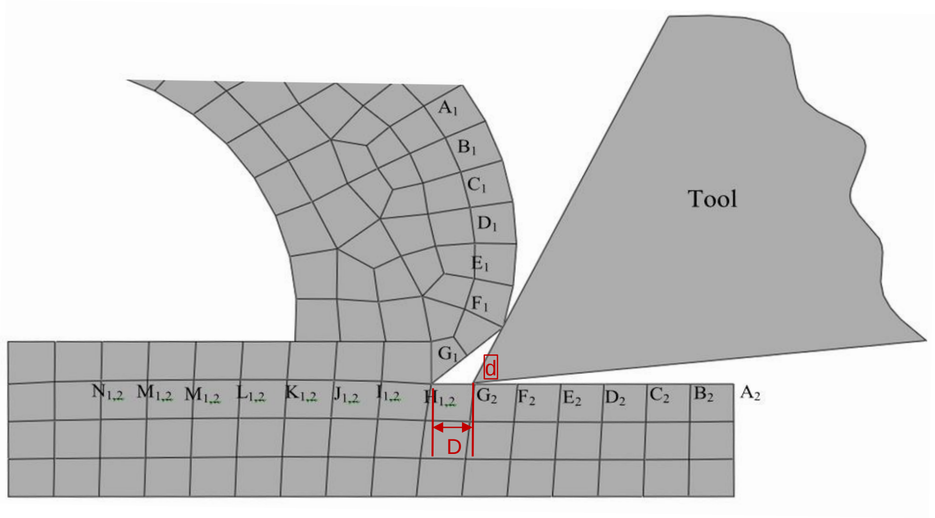

Figure 3-9: Chip separation criteria based on geometrical parameters

An improper critical distance value could result in the unrealistic material gap. It also results in convergence and numerical instability problems and greatly influence authenticity of the results. While investigating the performance of geometrical and physical chip separation criteria using plane-strain deformation, Zhong [141] found that critical geometric distance should always be sufficiently small to zero provided numerical stability can be achieved. Komvopoulos and Erpenbeck [150] exploited distance based criteria using plane-strain steady state model and determined the optimal value of critical distance 0.5L (half of element length, L) using trial and error simulations. Obikawa et al. [180] used geometrical criteria and selected critical distance equal to one-fifth of undeformed chip thickness. Mamalis et al. [120] used geometrical separation criteria in their cutting model and used critical distance equal to 5% of the element length. Zhang and Bhagchi [251] presented geometric criteria along a predefined separation line and proposed the critical distance within 30%-50% of element length. They also introduced improved geometric separation criteria based on the ratio of critical distance to a depth of cut. Later researchers frequently adopted geometrical separation criteria with critical distance value based on material properties, experimental data analysis and cutting conditions [120, 122, 144, 151, 152, 252].

The influence of critical distance approach on the chip and machined surface has also been investigated. Movahhedy et al. [142] selected the optimal critical distance value using trial and error cutting simulations. They found that waviness of the machined surface varies with the change of critical distance value. Huang and Black [253] performed an investigation study to evaluate geometrical separation criteria, physical criteria as well as a combination of both criteria. The study revealed that separation criteria significantly affect stress distribution as well as the distribution of effective plastic strain on the machined surface and the chip. However, the criteria don't significantly influence chip geometry as well as stress distribution in the chip.

The combination of geometrical and physical damage criteria have also been tested for performance and found to provide better results than individual criteria [136]. Lin and Lin [231-233] employed a combination of strain energy density and geometric distance as chip separation criteria in the oblique cutting model. Shet and Deng [254] and Shih et al. [255] adopted critical stress value as chip separation criteria at a specified distance ahead of the cutting tool. In their model, chip separation occurs when a stress index factor reaches its critical value at a specified distance ahead of the cutting edge of the tool. The stress criterion was defined as

$$\mathrm{f} = \sqrt{\left(\frac{\sigma_{\mathrm{n}}}{\sigma_{\mathrm{fl}}}\right)^2 + \left(\frac{\tau}{\tau_{\mathrm{fl}}}\right)^2}, \qquad \sigma_{\mathrm{n}} = \max(\sigma_2, 0) \qquad (3.1)$$

In eq. (3.1), f is stress index parameter, $\sigma_n$and τ are the normal and shear stresses at assigned distance ahead of cutting tool. The components $\sigma_{fl}$and τ_{fl} are pure tensile failure stress and shear failure stress respectively. According to their model, when the value of stress index factor reaches its critical value 1.0 at assigned distance (size of one element), chip separation takes place.

3.5.4 Meshing criteria and techniques

In FEM, due to complex parts geometries as well as to analyse distribution and intensity of output variables within specific zones, continuum structures are divided into elements interconnected to each other at the intersection points called nodes. The discretization involves subdividing the problem domain into finite elements of different sizes and shapes. The meshes of workpiece and tools in machining simulations are based on 2D or 3D elements. The earliest 2D FE cutting simulations studies were based on 2D linear triangular elements and later followed by quadrilateral elements [149]. Fig. 3-10 shows the most common elements used in FEM studies. The advancing front method and the Delaunay triangulation methods [235, 256] are the bases of many mesh generation programs for meshing. Using Delaunay triangulation method, only triangular elements can be used for mesh generation.

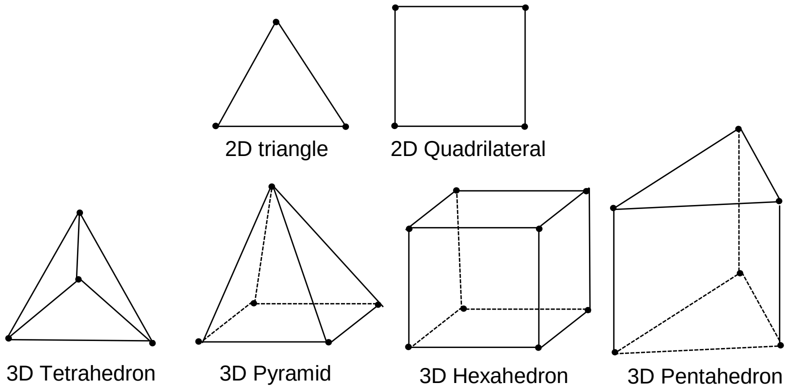

Figure 3-10: common element used in FEM simulations

The performance of chip formation and the severity of mesh distortion in the Lagrangian formulation are highly dependent on the type of elements used [257] which can influence convergence and numerical stability. The performance of elements can be influenced by the cutting conditions, tool geometry and cutting speed with respect to the type of machining. The same element configuration offers varied elements efficiency under two different cutting conditions. During the deformation, elements suffer two major numerical problems called shear locking and volumetric locking. Finite elements endure locking when they observe the artificial stiff response to deformation. One of the main reasons of locking is the inability of interpolation functions to approximate strain distribution accurately in solids. Another possible factor leads to locking problem is an improper FE equation system caused by poor governing equations.

Second order elements are considered to perform with high accurate results output in machining simulations compared to the first-order simplex which suffers volumetric and shear locking during deformation [235]. The first-order fully integrated quadrilateral elements offer better convergence properties than triangular elements in orthogonal cutting [110, 258]. The fully integrated elements and elements with reduced-integration show dissimilar deformation behaviour under extreme deformation conditions. The degree of chip segmentation found higher when using fully integrated element [110, 258]. When modelling continuous chip curvature, fully-integrated elements offer better curvature than reduced-integration elements [112]. The elements with full integration have more affinity to undergo volumetric locking. Although the implementation of reduced integration in quadrilateral and brick elements could be helpful to avoid locking phenomenon, it also suffers locking when using 4-noded quadrilateral or 8-noded brick elements [149].

The number of elements within unit area refers to mesh density dependent on element type. Although mesh density is crucial to achieving ideal chip formation with better results, the computational cost could be higher using same mesh density within the whole domain. It is advisable to use refined mesh in and near chip formation zone while coarse mesh can be used in the remaining model.

One of the solutions developed to resolve the mesh distortion problem in orthogonal cutting includes the development of remeshing strategies without the need for geometrical or physical separation criteria. Adaptive remeshing introduces new smoother mesh when required to reduce element distortion by maintaining the same mesh topology in terms of a number of elements and nodes. Fig. 3-11 shows the remeshing criteria applied in cutting model and how it improves chip formation results.

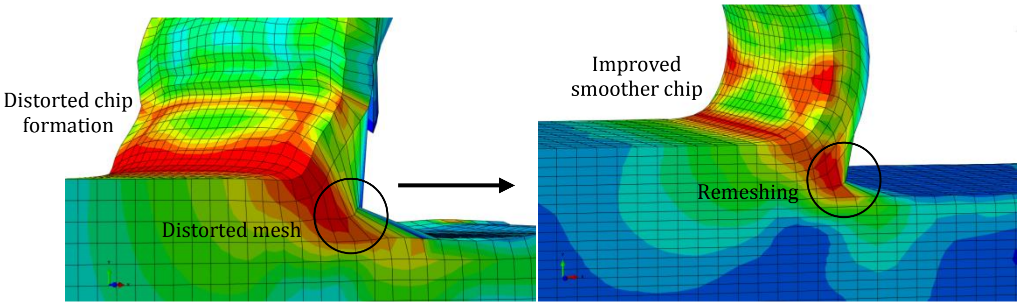

Figure 3-11: Remeshing avoids mesh distortion and improves chip formation smoothness

In remeshing technique, when workpiece elements satisfy predefined critical conditions, all the values of state variables are obtained at node points of the distorted mesh by extrapolating the integration point values and averaging over connected elements. New mesh is generated and all the state variables from the nodes of the old mesh are interpolated to the nodes of the new mesh. However, the transfer of solution variables from old to new mesh could lead to a reduction in the magnitude of variables. This error can be reduced by adopting more refined mesh in the shear deformation zone during remeshing. One of the issues in refinement is the convergence problem arise in refining mesh when the position of nodes of the new and old mesh are different [259]. Fig. 3-12 presents two of the mesh refinement methods used during remeshing process. In the trapezoidal method, mesh refinement is achieved by geometric refinement using trapezoidal elements with different element angles. In another approach, additional free nodes are introduced within the original mesh by linear interpolation from the adjacent nodes and mesh density can be increased by increasing number of free nodes and keeping the similar element angle. The choice of mesh refinement criteria is based on deformation conditions and sensitivity requirement.

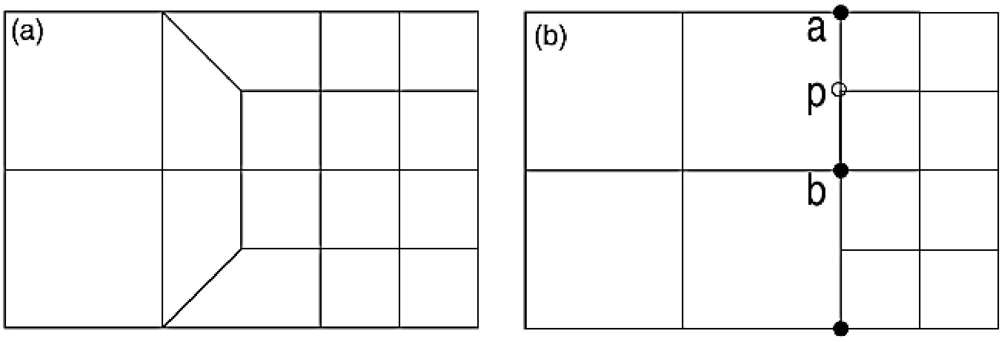

Figure 3-12: Mesh refinement techniques (a) trapezoidal method (b) additional free nodes of similar angle by interpolation [259]

Although adaptive remeshing technique can be adopted for any material, its performance reduces to failure for brittle and hyperelastic materials. The remeshing technique in comparison with geometrical or physical techniques seems better strategy for realistic simulation; the results can be affected by crack generation ahead of the cutting (based on the theory of chip formation due to crack) [119]. Although, the crack generation and its propagation can be predicted using adaptive remeshing [260], it still suffers some limitation in the estimation of magnitude and direction.

3.6 Numerical simulation modelling of tool wear

One of the major contributions of FEM in machining simulations is providing a platform to predict tool wear rate and mechanism under a variety of machining conditions. Tool wear is a critical machining factor that has significant effects on principal output parameters including cutting forces, temperature and surface finish. The FEM has successfully been exploited in the estimation of different type of tool wear in different machining processes. Tool wear mechanism and wear rate models are mainly based on analytical, experimental and empirical studies [155, 261-266]. The well-known model developed to estimate tool life based on machining conditions is Taylor's tool life equations and its modified models [267-269].

The researchers employed different tool wear models and developed different methodologies to predict tool wear initiation and evolution to predict tool life in cutting simulation for a wide range of materials. The frequently adopted tool wear materials in FE tool wear studies are coated and uncoated carbide tool, CBN and PCBN tools, and ceramics, cermet, and diamond tools [270, 271]. Dependent on the tool and workpiece material and cutting conditions, the tool wear develops mainly under the influence of mechanical, chemical and thermo-mechanical contact [272].

There are direct and indirect methods developed to characterize the tool wear in FE cutting simulations. Research studies reveal that tool wear is dependent on cutting temperature, stresses, contact pressure and cutting velocity [230, 273-276]. In indirect approach, the tool wear can be effectively estimated by predicting the distribution of these output variables under different machining conditions. Monaghan and MacGinley [277, 278] studied tool wear in various coated and uncoated tungsten carbide and cemented carbide tools. They studied stress and temperature distribution with different coatings in the PSZ, SDZ and coating boundaries and found the simulation results in good agreement with experimental results.

The FE simulation of tool wear studies requires the estimation of tool wear and its modelling. Most of the FE studies integrated empirical or analytical tool wear models using user-defined subroutine into the given FEM package [230, 270]. The general approach is to run the tool wear analysis by user-defined subroutine at steady-state chip conditions. The output solution variables (according to the wear model) are calculated at all tool nodes which are in contact with the workpiece. The tool wear subroutine incorporates measured values of solution variables and calculates tool wear rate using adopted empirical or analytical wear model. The geometry of the tool is then updated using calculated tool wear rate by wear subroutine. Fig. 3-13 presents the basic steps to measure the tool wear in FE studies.

Tool wear models exploited in FE tool wear simulation studies are based on abrasion, adhesion and diffusion [155, 172-175, 277, 279, 280]. The pioneer numerical study in tool wear estimation was performed by Usui et al. [155] using adhesive wear based characteristic equation and predicting the temperature and stress distribution. The Usui's abrasive wear model has frequently been adopted in various other tool wear studies [270, 280-282]. The Usui's model described as

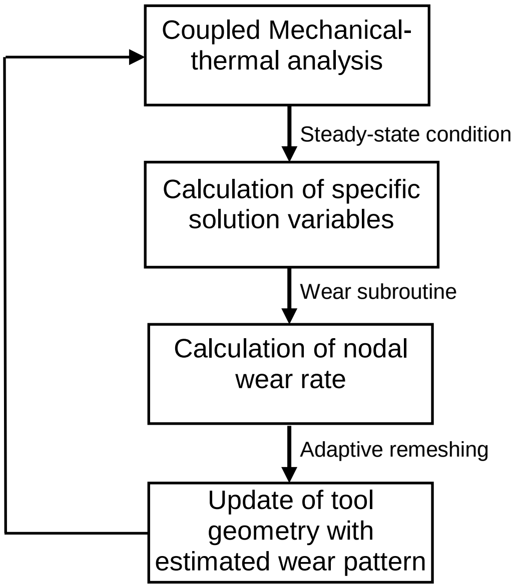

Figure 3-13: Basic methodology adopted in tool wear measurement techniques

$$\dot{\omega} = F\sigma_n V_s \exp\left(-\frac{L}{T}\right) \qquad (3.2)$$

Where $\dot{\omega}$ is the wear rate and F and L are the tool and workpiece materials constants.

Attanasio et al. [174, 175, 283] performed 2D and 3D ALE based simulation studies of flank and crater tool wear of tungsten carbide based on diffusive wear mechanism. They adopted Takeyama and Murata (T-M) [263] tool wear model which is based on abrasive and diffusive wear. The model is described as

$$\dot{\omega} = G(V, f) + D\exp\left(-\frac{E}{RT}\right) \qquad (3.3)$$

Where, the term $G(V, f)$ represents abrasive wear. The parameters V and f are the cutting speed and feed. The term E is the activation energy and R is the universal gas constant. They ignored the abrasive wear due to high hardness of tungsten carbide as well as due to the reason that, in T-M wear model at temperature exceeding 700-800 °C, the abrasive wear disappears and only diffusion takes place [284]. However, they found the disagreement in results of crater extension when using T-M wear model. When using Usui's model, the simulation presents high error in crater depth and position compared to experimental study [285]. In order to overcome the limitations of T-M and Usui's wear models, they proposed a new coupled abrasive-diffusive model by combining Usui's and T-M wear model and performed tool wear study based on abrasive and diffusive wear mechanism [173]. Molinari and Nouari [273, 274] proposed diffusion wear model by considering the contact temperature as the main parameter in determining the diffusive wear rate. Zanger and Schulze [276, 286] performed tool wear studies and proposed a hybrid method of experimental and numerical approach based on output data to calculate wear rate. They determined that Usui's and T-M models can better predict wear rate using FEM analysis. Lorentzon and Jarvstrat [285] evaluated Usui's model and its two modified forms and T-M model using different frictional criteria. They concluded that Coulomb's friction model cannot accurately predict quantitative tool wear irrespective of the wear model used. Also friction criteria significantly influence sliding velocity which consequently influences crater wear depth and location. Salvatore [287] presented tool crater wear modelling using measurement of tool wear volume loss as a function of dissipated energy by friction. They adopted predefined maximum energy approach at which elimination of nodes takes place when the dissipated energy reaches its maximum value.

The updating of tool geometry with wear pattern can be performed using element deletion method and nodal displacement methods [172, 270, 286]. The use of nodal displacement method has been employed extensively. Yen et al [281, 282] performed a study of tool wear rate for uncoated carbide tool in cutting simulation of carbon steel. They employed Usui's wear model [261][and evaluated tool wear at a discrete point in cutting time. They updated the rake and flank face geometry based on calculated wear using Individual nodal movement method and also used average values of cutting variables. Xie et al. [172] also adopted nodal movement method to model tool wear pattern. They adopted flank wear calculation subroutine in the iteration model and implemented a predefined flank wear land width. The simulation continues in cycles until the predefined maximum flank wear land width is achieved. A similar approach of iteration model, maximum flank wear land width and nodal movement method is adopted by many researchers [286, 288]. When using node movement method, the direction of nodal movement is in the direction of contact pressure at the relative node. The updating of tool geometry using nodal displacement method results in mesh distortion. The mesh distortion is resolved using adaptive remeshing procedure in which smoother new mesh is generated with updated geometry. Adaptive remeshing produce tool wears pattern on the tool during the updating tool geometry stage [172, 173]. It has also been employed to smoothen the crater wear profile as well as mesh coarsening at cutting edge [172].

Another approach exploited in characterizing the tool wear is by pre-defining the crater and flank wear in tool modelling and comparing the simulation results of new and predefined worn tools [137, 271, 281, 289, 290]. Different wear magnitudes and geometry can be modelled using this approach and sensitivity of output variables is analysed against various tool wear conditions.

3.7 Post Processing: Results and Analysis

In order to understand the true response behaviour of workpiece and tool during chip formation, it is necessary to determine the variation of output solution variables within chip formation zones as a function of input variables. The output solution variables obtained in FE simulations are node-based quantities (displacement, velocity, reaction force, etc.) or element-based quantities (stress, strain, etc.). In FE machining studies, various output parameters have been analysed including yield stress, plastic strain, effective plastic stress and strain, temperature, strain rate, hydrostatic stress, temperature, residual stress, cutting forces. The response of cutting forces and distribution of temperature and stresses as a function of input variables is briefly discussed in the following sections.

3.7.1 Stress and strain components

The stress distribution on tool-chip interface in FE machining studies has widely been studied using stress distribution study models [162, 291, 292]. The stress distribution models are based on data obtained using different experimental methods including photoelastic and split tool methods [293-296]. Before the exploitation of commercial FE packages, individual stress components were measured to record deformation conditions. Von Mises is the most frequently studied yielding criteria in FE cutting simulations [231, 297, 298] using commercial software. According to the von Mises yield criteria, initial yielding occurs when deviatoric stress invariant acquires a critical value. The von Mises criterion in terms of principle stresses is described as:

$$(\sigma_1 - \sigma_2)^2 + (\sigma_2 - \sigma_3)^2 + (\sigma_3 - \sigma_1)^2 = 2\sigma_Y^2 \qquad (3.4)$$

Where, σ_1 , σ_2 and σ_3 are principle stresses and σ_Y is the yield stress of the material.

Research studies suggest that in machining, the magnitude of von Mises stresses is higher near the tool tip in PSZ compared to SDZ and TDZ [231, 232, 299, 300]. The intensity of the stresses varies along the tool-chip interface as a function of tool rake angle and cutting edge.

The stress distribution on the machined surface in terms of residual stresses has also been the topic of interest. Machining is a process that involves plastic deformation, heat generation and many other mechanical, chemical and thermal effects. After machining, some stresses remain within the final machined surface which influence the form accuracy and surface finish of the material. These stresses are called residual stresses which are the distributed stresses on and under the machined surface after machining.

In FE machining simulations, residual stresses are generally recognized as tensile stresses and compressive stresses along cutting direction and perpendicular to cutting direction [114, 122, 144, 231, 301, 302]. When measuring residual stress, the elements at the final machined surface should be chosen at points sufficiently away from the tool edge and from the boundary conditions to reduce the influence of both factors. High mesh density in the chip formation zone is required to improve prediction of residual stresses in machining simulations [151].

3.7.2 Cutting forces

Cutting forces have been frequently investigated to gain a pivotal understanding of mechanics of chip formation and tool wear. High cutting forces can influence surface integrity and cause tool failure. The cutting forces are generally analysed as a function of cutting force magnitude and its trend during cutting. The principal cutting forces components in machining simulations include tangential cutting force in the direction of cutting velocity, feed force in the direction of feed and thrust force normal to the velocity.

The well-known Merchant's force model [303] is based on orthogonal cutting and discuss the inter-dependency of shear angle Φ, tool rake angle α, and cutting forces. Fig. 3-14 presents the Merchant's circle force model in orthogonal chip formation process. In his model, the resultant force R exerted by the tool is resolved into tangential force F_t and feed force F_f. Additionally, the force R is resolved into shear force F_s and normal component F_n.

Tool geometry, friction parameters, and shear angle are the three important parameters with a strong correlation that have a significant effect on cutting forces. In general principle, regardless of material type, high coefficient of friction offers high frictional resistance and therefore high cutting forces.

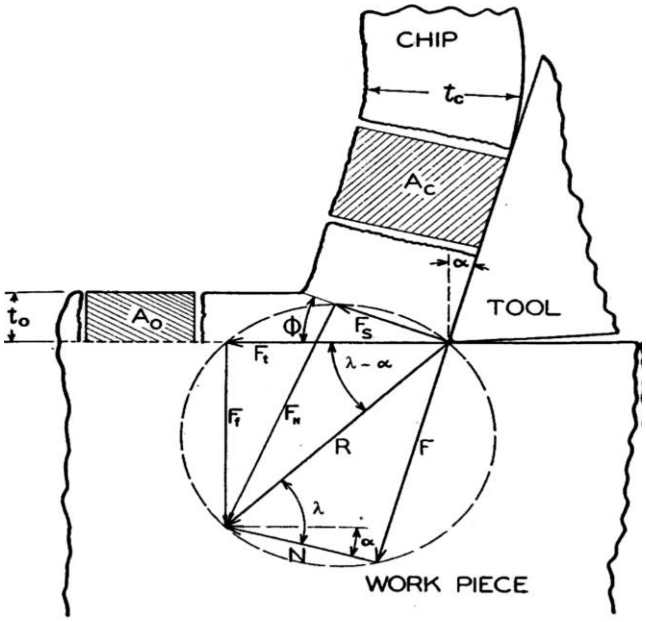

Figure 3-14: Merchant’s circle force model diagram [303]

The FE studies [122, 159, 255, 258, 304] suggest that cutting forces increase with the decrease of rake angle and cutting edge radius. The studies also reveal that for the same tool geometry, when the coefficient of friction increases, shear angle decreases.

Numerical simulation studies reveal that cutting forces are also affected by cutting speed. The magnitude of cutting force decreases with the increasing cutting speed [299] due to material softening effect. However, this behaviour is highly dependent on the thermal conductivity of tool and workpiece [305].The studies also suggest that the machining response of reduction of cutting forces with increasing speed found highly dependent on feed rate [299]. The effect of material constitutive models in machining simulations was investigated by many researchers [153, 236, 306]. The study revealed that cutting forces are the most influenced output variables when different constitutive material models are used using the same cutting conditions.

The cutting forces can be accurately estimated based on the frictional shear factor value. When using smallest value of 0.1 in the cutting simulation, cutting forces can be predicted within a maximum of 4% error [119]. Tangential, thrust and feed forces can be highly influenced by the type of friction models used in cutting simulation [169]. When using constant and variable friction coefficient in two different simulations, the %age difference between experimental and simulation feed forces are 50% and 10% respectively [307]. Arrazola and Ozel [170] compared Coulomb's friction and sticking-sliding friction using friction coefficient with finite sliding and shear stress limit. They found a significant difference of 35% in thrust forces and 11% difference in tangential forces. Haglund et al. [169] compared six different friction models including Coulomb, limited shear stress model, and temperature-dependent friction coefficient model. They used constant and variable friction coefficient and in combination within sticking and sliding region. Their findings suggest the significant influence of friction models on tangential and feed forces.

3.7.3 Cutting temperature

During machining, the high cutting temperature may lead to desirable or undesirable effects dependent on the tool and workpiece material and cutting conditions. It could ease machining by material softening or could result in tool wear and thermal expansion and undesirable residual stresses consequently effecting machining performance. Although there exist experimental and analytical methods to record temperature [245, 308-310], it is difficult to monitor the exact cutting temperature locally as well as its distribution at tool-chip interface. FEM is regarded as a highly valuable tool in the prediction of cutting temperature during machining and its distribution [311]. The cutting temperature in FE machining simulations are usually analyzed to estimate chip and machined surface behaviour, variation in mechanical properties and tool wear.

One of the critical factors to consider in FE machining simulations is temperature distribution in different deformation zones and in cutting tool [240, 308]. The conversion of mechanical energy into heat energy at tool-workpiece interface during chip formation inspires higher cutting temperature. In PSZ, heat is produced during chip formation owing plastic deformation. Dependent on the chip geometry, heat in SDZ generate due to plastic deformation and friction between chip and tool rake surface along the contact length and also contribute to cutting temperature. The heat produces in the TDZ due to the friction between tool flank face and machined surface. The heat generated in TDZ is initially in small magnitude and start contributing to cutting temperature with the progression of tool wear. Fig. 3-15 presents a general heat generation and transfer zones.

The major FE machining simulation work is based on the study and evaluation of temperature distribution at steady-state conditions. A pioneering study of temperature distribution analysis was done by Tay et al. [312], in which they studied the temperature gradient across the shear plane for characterization of material properties and work-hardening rate. The temperature of chip surface is generally obtained as average temperature by adding temperature of all the nodes of chip surface divided by a number of nodes. Numerical studies suggest that the maximum heat generation takes place in the PSZ and

SDZ caused by plastic deformation and sliding and sticking friction [118, 125, 128, 305, 310]. The temperature in SDZ found higher than the PSZ [299, 300] for a wide range of metals.

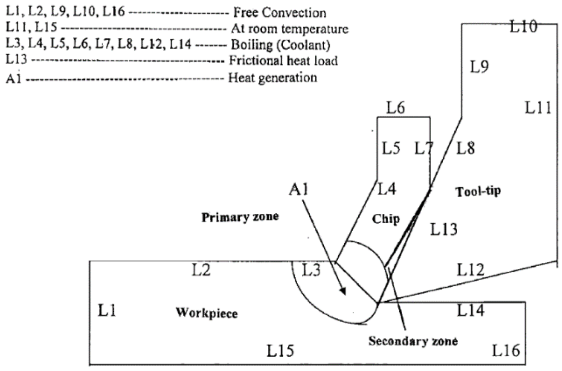

Figure 3-15: Temperature distribution during chip formation [310]

The temperature distribution at the rake and flank faces of the tool has also been studied [124, 125, 271, 305, 310]. The average temperature is found to rise with an increase in the cutting velocity [118, 124, 311] and tool rake angle. The increase of coefficient of friction results in frictional resistance in the SDZ which leads to increase in cutting temperature at tool-chip interface. The temperature distribution remains non-uniform as a function of chip geometry along the rake face and maximum temperature occurs just above the cutting edge. The temperature on the rake face observed much higher than the flank face of the tool.

The effect of machining input variables on cutting temperature including cutting speed, feed, cutting depth, and tool material and geometry have largely been investigated [124, 125, 274, 275, 301, 305, 313]. The thermal conductivity of the tool and workpiece materials contributes significantly to the cutting temperature. The cutting tool with higher thermal conductivity offer better performance when cutting lower- thermal conductivity workpiece material than cutting a workpiece with higher thermal conductivity [314].

3.7.4 Summary

This chapter reviews the development of FE modelling of the machining process. The mesh-based and meshless approaches employed in machining simulations are discussed along with different chip separation criteria and friction criteria. Meshless methods have great potential to perform realistic chip formation and tool wear studies without suffering mesh distortion issues. However, FE software containing meshless methods doesn't allow full thermo-mechanical analysis using particle methods. Also, there is a limitation of contact definition of two meshless surfaces. Specialized machining FE codes don't support meshless methods. Chip separation criteria are the most controversial aspect of machining simulation using FEM as it influences the results of all the output variables. The accuracy of geometrical separation criteria and physical separation criteria is highly dependent on the selection of the critical value of the parameter. Geometrical separation criteria suffer from the limitation of tool geometry. It cannot be accurately used when negative rake angle and higher cutting edge radius tool are used. In most of the machining simulation studies, the critical values of these criteria were mainly obtained without any sophisticated designed rules. For a given workpiece material, the critical value may vary as a function of FE model type, the scale of machining, cutting conditions, tool geometry and various other factors. Substantial experimental studies, as well as extensive trial and error simulation studies, are required to validate the true threshold geometric or physical values.

Chapter 4- Smoothed particle hydrodynamics modelling for SPDT of silicon

4.1 Introduction

SPH method has been well-developed and successfully validated for the simulation of machining compared to other particle methods including DEM and FPM. The method has been successfully employed in the machining of various ductile materials [116, 211, 315]. However, simulations of machining of brittle materials using SPH method are very few. Silicon, being one of the hardest and brittle materials never been simulated for cutting process using SPH. Considering an efficient approach in terms of accuracy and computational cost for the cutting process, SPH method was adopted in this study using FE code ABAQUS to investigate the cutting mechanics of silicon. The SPH method can provide profound insight of variations in natural chip formation, hydrostatic pressure and stress distribution in hard and brittle materials and therefore, carries great significance. In this chapter, the classical SPH method along with its governing equations is discussed. The modelling of simulation of orthogonal cutting of silicon from the perspective of tool and workpiece geometry and contact conditions is presented. A material constitutive Drucker-Prager (DP) model was selected to predict the machining response behaviour of silicon and the model parameters were identified using inverse analysis approach.

4.2 The standard SPH formulation

The principle of the SPH method is to provide the numerical approximation to the initial boundary value problems described by the partial differential equations in terms of laws of conservation of mass, energy and momentum. During numerical approximations for the spatial derivatives, the neighboring elements, and nodes of the element of interest do not change in standard mesh-based Lagrangian method. Whereas in SPH, particles position changes relative to each other and the neighboring particles of the particle of interest change during deformation.

4.2.1 SPH Kernel approximation

SPH uses kernel approximation to approximate field variables and properties in the SPH solution domain shown in Fig. 4-1.

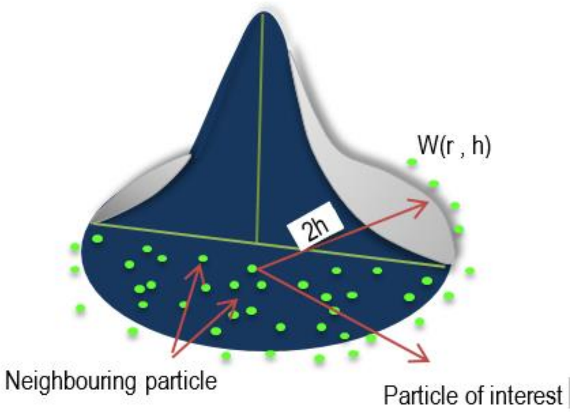

Figure 4-1: SPH kernel approximation

SPH approximate field variables at any particle by classical summation of smoothing function values of neighbouring particles within a sphere of influence. The length of the sphere of influence is defined as the maximum distance to which the interaction can occur.

The SPH approximation is derived from the following equation:

$$f(x) = \int_V f(\acute{x})\delta\,(x - \acute{x})d\acute{x} \qquad (4.1)$$

Where $f(x)$ is a scalar function of the three-dimensional position vector x ranging within a volume V. $\delta(x - \acute{x})$ is the Dirac’s delta function. The kernel is normalized to unity as below:

$$\int_V W(x - \acute{x}, h)d\acute{x} = 1 \qquad (4.2)$$

When h approaches zero, the smoothing kernel will satisfy the delta function

$$\lim_{h \to 0} W(x - \acute{x}, h) = \delta(x - \acute{x}) \qquad (4.3)$$

So the scalar function $f(x)$ in the kernel function W can be described as

$$f(x) = \int_V f(\acute{x})W(x - \acute{x}, h)\, d\acute{x} \qquad (4.4)$$

The function $f(\acute{x})$ can be deduced by considering the kernel in the form of point spread function. In the discrete SPH form, the values of $\acute{x}$ turns into the set of SPH particle’s discrete position and the summation function replace the integral. The SPH particle approximation can finally be written as

$$f(x) \cong \sum_{j}^{n} \frac{(m_j)}{\rho_j} f(x_j)W(|x_i - x_j|, h) \qquad (4.5)$$

Where $f(x_j)$ is the scalar value of *j-th* particle and m_j and ρ_j are the mass and densities of *j-th* particles; where *j* represents the neighbouring particle of the *i-th* particle for which field variables need to be approximated.

4.2.2 Equations of continuity, motion and state

4.2.2.1 Equation of Continuity

The equation of continuity when defining the elastoplastic behaviour of material using SPH formulation is described as

$$\rho_i = \sum_{j=1}^{n} m_j W_{ij} \qquad (4.6)$$

Where,

$$W_{ij} = W(x_i - x_j, h) \qquad (4.7)$$

The free-surface, as well as material interface, can be treated using following equation

$$\rho_i = \frac{\sum_{j=1}^{n} m_j W_{ij}}{\sum_{j=1}^{n} \frac{m_j}{\rho_j} W_{ij}} \qquad (4.8)$$

The mass conservation equation in Lagrangian description can be expressed as

$$\frac{\partial \rho}{\partial t} = -\frac{\partial \rho v_i}{\partial x_i} + v_i \frac{\partial \rho}{\partial x_i} \qquad (4.9)$$

$$\frac{d\rho}{dt} = -\sum_{\beta}^{n} \frac{m^{\beta}}{\rho^{\beta}} \rho^{\beta} v_i{}^{\beta} \frac{\partial W^{\alpha\beta}}{\partial x_i} + v_i \sum_{\beta}^{n} \frac{m^{\beta}}{\rho^{\beta}} \rho^{\beta} \frac{\partial W^{\alpha\beta}}{\partial x_i} \qquad (4.10)$$

Where α and β are the coordinates directions and v is the velocity vector.

The equation 4.10 can be further simplified as

$$\frac{d\rho}{dt} = \sum_{\beta}^{n} m^{\beta} (v_i{}^{\alpha} - v_i{}^{\beta}) \frac{\partial W^{\alpha\beta}}{\partial x_i{}^{\beta}} \qquad (4.11)$$

4.2.2.2 Equation of momentum

The equation of momentum in the SPH model is expressed as

$$\frac{dv_i}{dt} = \frac{1}{\rho} \frac{\partial \sigma_{ij}}{\partial x_j} + F_i \qquad (4.12)$$

Where σ_{ij} is the stress tensor and F_i is the body force. When solving the first term of equation (4.12)

$$\frac{\partial}{\partial x_j}\left(\frac{\sigma_{ij}}{\rho}\right) = \frac{\rho \dfrac{\partial \sigma_{ij} - \sigma_{ij} \dfrac{\partial \sigma}{\partial x_i}}{\partial x_i}}{\rho^2} = \frac{\partial}{\partial x_j}\left(\frac{\sigma_{ij}}{\rho}\right) + \frac{\sigma_{ij} \dfrac{\partial \sigma}{\partial x_i}}{\rho^2} \qquad (4.13)$$

By substituting the value of term $\frac{\partial}{\partial x_j}\left(\frac{\sigma_{ij}}{\rho}\right)$ from eq. (4.13) into eq. (4.12), we get

$$\frac{dv_i}{dt} = \frac{\partial}{\partial x_j}\left(\frac{\sigma_{ij}}{\rho}\right) + \frac{\sigma_{ij} \dfrac{\partial \sigma}{\partial x_i}}{\rho^2} + F_i \qquad (4.14)$$

From eq. (4.5), the final SPH equation of momentum in the elastic-plastic model can be described as

$$\frac{Dv_i{}^{\alpha}}{Dt} = \frac{\sigma_i{}^{\alpha\beta}}{\rho_i^2}\sum_{j=1}^{n}\frac{m_j}{\rho_j}\rho_j\frac{\partial W_{ij}}{\partial x_i{}^{\beta}} + \sum_{j=1}^{n}\frac{m_j}{\rho_j}\frac{\sigma_j{}^{\alpha\beta}}{\rho_j}\frac{\partial W_{ij}}{\partial x_i{}^{\beta}} + F_i \qquad (4.15)$$

The eq. (4.15) can be simplified to eq. (4.16)

$$\frac{Dv_i{}^{\alpha}}{Dt} = \sum_{j=1}^{n} m_j\left(\frac{\sigma_i{}^{\alpha\beta}}{\rho_i^2} + \frac{\sigma_j{}^{\alpha\beta}}{\rho_j{}^2}\right)\frac{\partial W_{ij}}{\partial x_i{}^{\beta}} + F_i \qquad (4.16)$$

4.3 Some limitation of SPH

Although the SPH method offers various technical advantages in the modelling of simulation of machining, it suffers some limitations that should be considered during modelling. A summary of the limitations of SPH technique as well as the limitation of the modelling aspects in Abaqus is presented in the Table 4-1.

Table 4-1: Limitations of SPH approach and capabilities in Abaqus

	SPH formulation
Material deformation	Less accurate approximation than the mesh-based method in the area of small deformation.
Stress distribution	The particle interaction become unstable (tensile instability) in the regions where tensile stresses become higher. This could lead to unrealistic fracture-like behaviour.
Mass distribution	An exact mass distribution in the part is limited to the model it with the regular cubic arrangement. The volume of SPH particles as well as the nodal mass of all associated particles in a given part is same. Therefore, the mass- distribution at the free surface of the part becomes inaccurate if the part is modelled other than regular cubic arrangement.
Loads	Surface loads cannot be directly applied to SPH particles.
Parts interaction	The interaction of dissimilar material is not possible in Abaqus and therefore, tool cannot be modelled with SPH particles
analysis	Only mechanical analysis can be performed. The thermal analyses are not supported in Abaqus
Computational time	When using multiple CPUs, some output variables including contact, energy, forces have limited choice in the manner these variables are calculated.
Modelling SPH	The SPH method cannot be applied directly in CAE environment of Abaqus and method is applied by modifying the generated input file

4.4 SPH machining model of silicon

4.4.1 Implementation of SPH in Abaqus

The SPH approach in Abaqus cannot be implemented for two-dimensional elements and only support three-dimensional modelling. In order to simulate the true machining conditions, 3D SPH machining model of SPDT of silicon was developed. The SPH approach adopted in Abaqus uses cubic spline as the interpolation polynomial based on classical SPH theory, as well as quadratic and quantic interpolation. The approach can also be used as updated forms of SPH based on mean flow correction configuration (XSPH method) as well as normalized SPH (NSPH method).

In Abaqus, SPH can be implemented to define silicon workpiece part in CAE environment using conversion to particle method. However, this method suffers some limitations. The initial and boundary conditions in this method cannot be specified for the converted PC3D particles. Also, boundary conditions applied to parent element nodes cannot be transferred to generated PC3D particles. Concentrated nodal loads and constraints including coupling or ties cannot be specified to the generated PC3D particles.

In this study, the second method was adopted in which PC3D particles were assigned to the silicon workpiece by modifying the generated input file. The tool-workpiece contact, initial and boundary conditions relevant to mechanical analysis as well as concentrated loads were defined at the workpiece. Node-based set of all the silicon workpiece part was created and node-based workpiece surface was defined.

Initial and boundary condition and interactions were defined and field output variables were requested in a standard way. The input file is generated and modified to change elements into PC3D particles. Fig. 4-2 shows the workflow of modelling of SPH simulation adopted in this study.

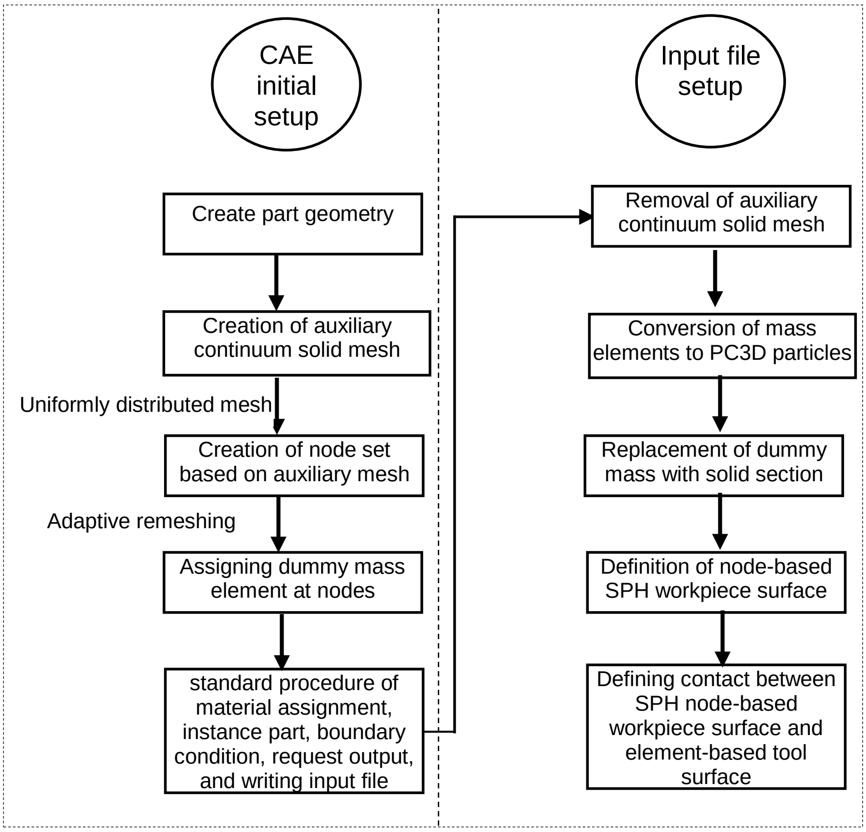

Figure 4-2: Workflow of SPH machining model of SPDT

4.4.2 Defining parts: silicon workpiece and diamond tool

In the simulation of machining using SPH, ideally, both the tool and the workpiece should be modelled using PC3D particles. However, the contact interaction of two SPH parts of dissimilar materials, as well as particles and Eulerian parts, is not allowed in Abaqus. Therefore, it is required to model one of the parts in contact using mesh-based Lagrangian elements. Fig.4-3 shows the SPH model of SPDT process.

Silicon workpiece was created as a deformable part and discretized with relevant 1-node PC3D elements. In SPH formulation, there is a small associated cube centered to the particle with user-defined characteristic length (half the length of cube side). When defining the workpiece with SPH, these small cubes fill the whole volume of the workpiece with some trivial approximation at the boundaries

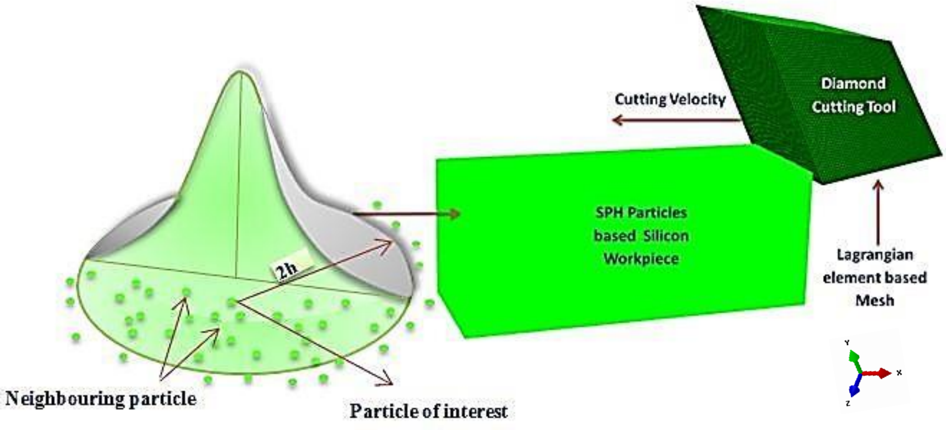

Figure 4-3: SPH cutting model of single point diamond turning

.

Since SPH particle of interest is influenced by the neighboring particles, it is crucial to define the nodal coordinates of these particles uniformly distributed in all directions. The sweep technique with medial axis mesh algorithm and minimized mesh transition was adopted to produce the uniform mesh. The transformation of workpiece geometry into SPH part is shown in Fig. 4-4.

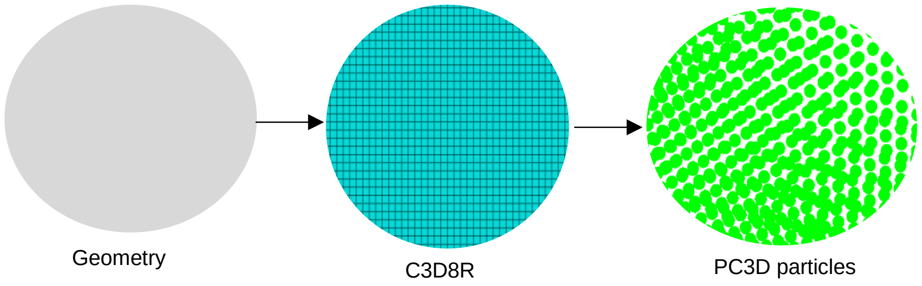

Figure 4-4: Sequence from workpiece geometry to SPH part

Diamond tool was kept rigid and was modelled with Lagrangian reduced integration C3D8R elements. Since ductile mode machining of silicon is solely possible at high hydrostatic pressure, negative rake angle tools were used in all the simulation studies.

4.4.3 Tool-workpiece interaction and chip formation

The interaction between the particles of two different SPH parts in contact can avail particle internal friction criteria without introducing any theoretical friction model. However, due to the limitation of employed FE code, the interaction between diamond tool and silicon workpiece is based on the node to surface contact algorithm. When using SPH approach, the diamond tool, and silicon workpiece can only interact using general-contacts. Penalty based contact algorithm was adopted at the tool-workpiece interface with friction coefficients range from 0.05 to 0.2.

In order to simulate the chip formation in SPDT, the diamond tool was assigned a velocity and the silicon workpiece bottom was kept fixed in all directions with encastre conditions to achieve required stiffness. Silicon part meshed with C3D8R elements and node set based on SPH particles was generated. The element-based surface of the diamond tool is required to be defined in the assembly module. The contact of the SPH-based surface of silicon with mesh-based surface of diamond tool was defined using general contact between SPH silicon surface and mesh-based tool surface.

In the SPH method, all particles have a physical degree of freedom and during chip formation, each particle movement is influenced by its neighbouring particles located within the sphere of influence of radius *r* which is twice the smoothing length, *2h*. The smoothing length was carefully chosen and distribution of particles was kept homogeneous to avoid any artificial stress concentration during cutting. The particles beyond the area of influence do not contribute to the intrinsic property of cohesion on the particle of interest. SPH particles interact with each other based on defined constitutive equations and internal friction between the particles.

4.4.4 Material constitutive model for silicon

The FE simulation of machining with different constitutive models suggests that the material response behaviour is sensitive to the employed material model [117, 316]. The chip geometry, cutting forces and other solution variables are highly dependent on the adopted constitutive models [153, 317]. Due to very limited research work on silicon in the finite element area, there is no specific constitutive model for silicon was identified. One of the most exploited constitutive models in machining studies is Johnson’s Cook (J-C) model (JC) [318] and its modified versions [319-321]. J-C model address strain, strain rate and temperature effect and is much suitable for evaluating the cutting parameters (speed, feed, etc.). However, it doesn’t incorporate pressure-dependent behaviour of material and cannot be used accurately to determine tool geometry effect. In contrary, DP model is much suitable to determine pressure-dependent material response behaviour during machining and tool geometry (rake angle, cutting edge) effect can be better predicted using this model. In this work, a pressure-sensitive Drucker-Prager (DP) model was considered an appropriate constitutive model to predict machining response behaviour of silicon during numerical simulations. DP model has been extensively used for granular-like soils, rocks and other alike pressure-dependent materials. The response behaviour of pressure-dependent materials can be expressed in terms of strength that increases with increasing pressure. The compressive strength of silicon is higher than its tensile strength [322] which is an elementary criterion of using DP model.

4.4.4.1 Drucker-Prager model

Drucker and Prager in 1952 [323] proposed a model to address the effect of mean (hydrostatic) stress for pressure sensitive materials which von Mises yield criterion failed to address. The proposition acknowledged as Drucker-Prager model (also known as extended von Mises model).

The Mohr-Coulomb and DP model with its yield surface are presented in Fig. 4-5. DP theory in principle is also a modified form of Mohr-Coulomb’s theory. The DP yield criterion is expressed as:

$$\mathrm{f}(\mathrm{I}_1, \mathrm{J}_2) = \alpha \mathrm{I}_1 + \sqrt{\mathrm{J}_2} - \mathrm{d} = 0 \qquad (4.17)$$

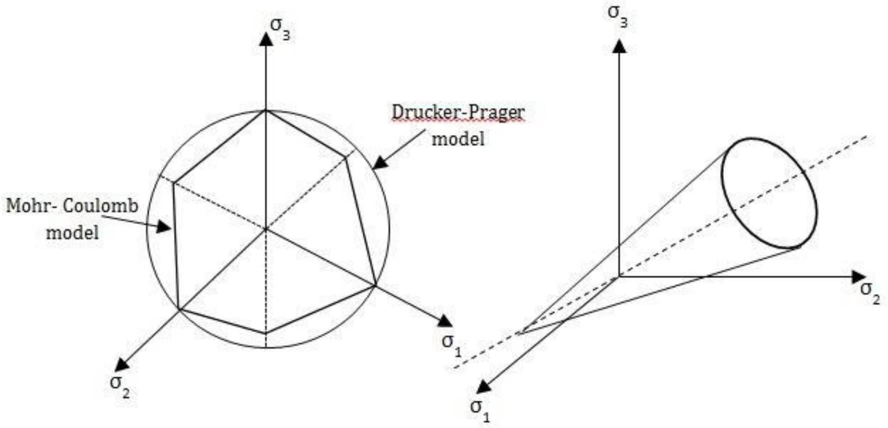

Figure 4-5: Drucker-Prager model: Mohr-Coulomb and DP model in deviatoric plane (left) DP yield surface (right)

Where I_1 is the first invariant of stress tensor and J_2 is the second invariant of the deviatoric stress tensor. α is the pressure-sensitivity coefficient, and d is known as the cohesion of the material. In DP model, the yield surface is the function of pressure and J_2.

The pressure-dependent linear DP yield function has also been expressed in three stress invariants [324] and inscribed as

$$f = t - p\tan\beta - c = 0 \qquad (4.18)$$

Where p is the equivalent pressure stress and c is the material parameter known as the cohesion of the material. The term $\tan\beta$ represents the yielding sensitivity to hydrostatic pressure, and β itself is the slope of the linear yield surface in meridional p-t stress plane and also known as friction angle of the material. The parameter t *is* deviatoric effective stress and expressed as

$$t = \frac{1}{2} q \left[1 + \frac{1}{k} - \left(1 - \frac{1}{k}\right)\left(\frac{R}{q}\right)^3 \right] \qquad (4.19)$$

and for uniaxial compression

$$C= (1 - \frac{1}{3}\tan\beta)\sigma_c \qquad (4.20)$$

Where *K* is the ratio of yield stress in the triaxial tension to triaxial compression, *q* is von Mises equivalent stress and *R* is the third invariant of deviatoric stress.

The evolution of equivalent plastic strain can be expounded using flow rule during deformation and provides the plastic strain relevance to stress components. Flow rule is stated in terms of plastic strain rate in the form of the following equation

$$d\varepsilon_{ij}^{p} = d\lambda \frac{\partial f}{\partial \sigma_{ij}} \qquad (4.21)$$

In Abaqus, the flow potential is written in the form as

$$g = t - p\tan\psi \qquad (4.22)$$

Where g is the flow potential and Ψ is dilation angle in the p-t plane.

4.4.4.2 Inverse analysis to find Drucker-Prager parameters

In order to employ DP model to predict machining response behaviour of silicon, DP parameters are required to be defined. However, no DP parameters were available for silicon. Inverse analysis method was adopted which is a reliable alternative to identify unique set of constitutive model parameters without undergoing extensive trials. In inverse analysis, the parameters were determined by attaining the best fit between experimental results and corresponding numerical simulation results. Due to highly controlled conditions, the experimental indentation tests are considered the most favourable process to characterize material properties at different scale. DP parameters were optimised to match load-displacement curve of finite element simulation model with the experimental results [325]. DP parametric evaluation was performed with more than 30 simulations by considering the effect of different values of friction angle, dilation angle and flow stress ratio.

Numerical simulation of the indentation process was carried out using FE code Abaqus. A 2D axisymmetric model with diamond indenter and silicon specimen was developed to circumvent the computational cost. In order to avoid size effect [326], the diamond indenter radius, silicon wafer thickness, indentation depth, loading and unloading conditions were kept identical to the experimental conditions.

The indented silicon was modelled as a deformable part using four-node axisymmetric element CAX4R. The diamond indenter was modelled as rigid part with 13.5 µm edge radius and 90° included angle similar to the one used in experimental indentation [325],. Fig. 4-6 shows the schematic of the 2D axisymmetric indentation test.

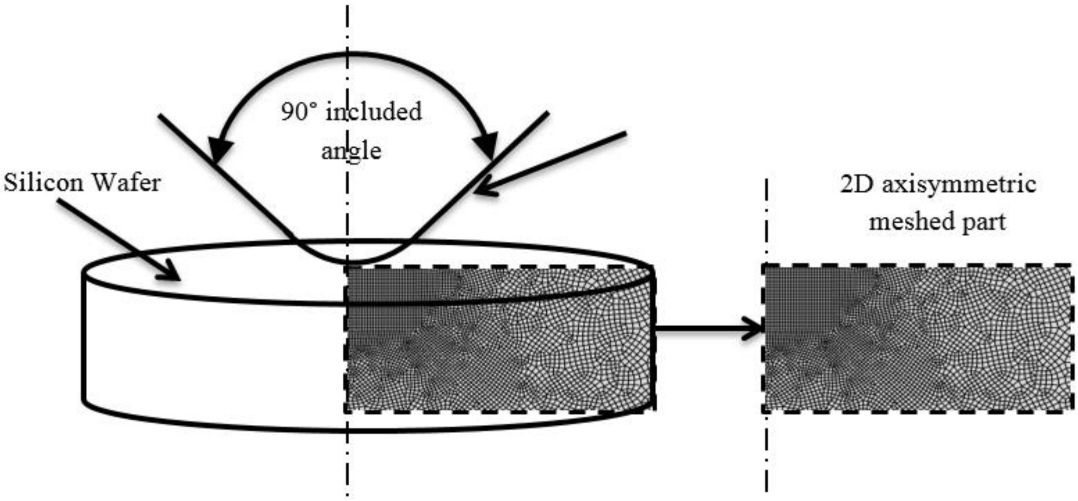

Figure 4-6: Schematic of 2D axisymmetric indentation simulation model

Very smooth refined mesh is selected at and near the contact area of the specimen to avoid any discrepancy in the computation. In order to reduce unnecessary computational time due to excessive mesh density while maintaining good simulation accuracy, a convergence test study was conducted. The von Mises stresses were used as an indicator to obtain satisfactory mesh refinement in the convergence test. The total number of elements recorded for silicon was 20,416. The material properties with elastic modulus of 146 GPa and Poisson's ratio of 0.2 were used. The silicon workpiece is indented at depth of 1100 nm to obtain and compare reaction forces with experimental results. Penalty friction formulation was adopted with coefficient of friction of 0.2 for diamond-silicon contact, and hard contact was chosen to define contact pressure-overclosure relationship with constraint enforcement method as default.

4.4.4.3 Determination of DP parameters

It was observed that by increasing the friction angle β results in increase in compressive strength of the material. Since the Flow stress ratio range is limited by the 0.78 ≤ K ≤ 1condition and found to have very little effect on load-displacement curve in this range, the most favourable K value of 0.82 was kept constant after verifying the effect. Table 4-2 lists different selected properties with favourable results out of many other properties tested in this simulation study. The relevant inverse analysis parameters were selected which influence the model behaviour and offer a reasonable reduction in error difference between experimental and simulation results. In order to assess the dependency of the model on a certain parameter, other parameters were kept constant and the model was tested for varied parameter values.

Table 4-2: Selected parameters of Drucker-Prager model

Simulation	DP Property	Friction angle	Flow stress ratio	dilation angle
		B	K	*Ψ*
1	Property1	20°	0.82	-10°
2	Property2	20°	0.82	-18°
3	Property 3	20°	0.82	-4°
4	Property 4	20°	0.82	-14°
5	Property 5	14°	0.82	-10°
6	Property 6	12°	0.82	-10°
7	Property 7	12°	0.98	-10°
8	Property 8	20°	0.82	10°
9	Property 9	24°	0.82	-16°
10	Property 10	26°	0.82	-20°
11	Property 11	28°	0.82	-20°

The dilation angle Ψ relates to the volumetric strain during plastic deformation, and it remains constant during plastic yielding. For Ψ=0 corresponds no volumetric strain, Ψ>0 shows volume increase and Ψ <0 signify a reduction in volume. Silicon exhibit volume reductions of 20-25% [62] under loading when enduring pressure-induced phase transformation corresponding to negative dilation angle. Stress, strain and other internal state variables are evaluated to characterise the material behaviour under loading and unloading conditions.

The hydrostatic pressure was measured for different DP parameters β and Ψ values in all the indentation tests. Those DP parameter values were chosen for which the hydrostatic pressure lies within the range of 8-16 GPa. Since this range lies in the structural transformation zone of silicon, plastic deformation would be the possible outcome leading to phase transformation in high-pressure range with little brittle fracture at low pressures. Indentation of silicon results in cracks generation as well as plastic deformation under pertained hydrostatic pressure. Crack generation in indentation test instigated at the point where the fracture strength of the material dissolved by increased local maximum principal tensile stress.

Fig. 4-7 shows the hydrostatic pressure for the DP parameters of property 10. Hydrostatic stress is the measure of average of three principal stress components and described as

$$\sigma = \frac{1}{3}(\sigma_1 + \sigma_2 + \sigma_3) \qquad (4.23)$$

Where σ is the hydrostatic stress and $\sigma_1, \sigma_2 \text{ and } \sigma_3$ are the stress components in three principal axes *x, y,* and *z,* respectively. The hydrostatic stress gradient in the indentation zone was found the highest under the indenter tip and reaches to 14 GPa for full indentation depth.

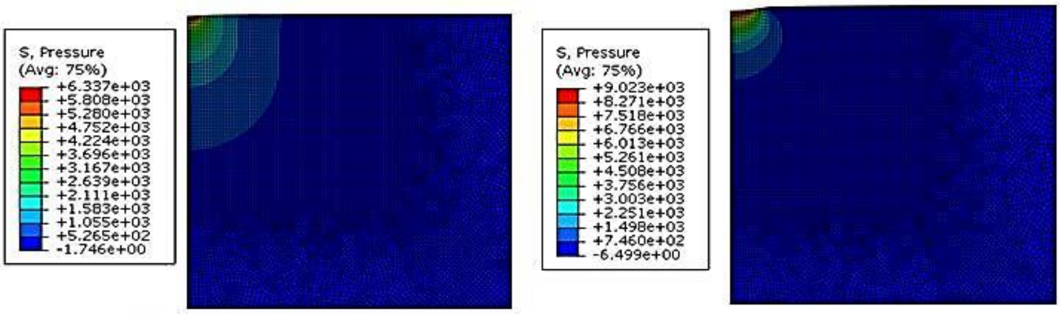

(a) Indentation depth of 153nm

(b) Indentation depth of 411nm

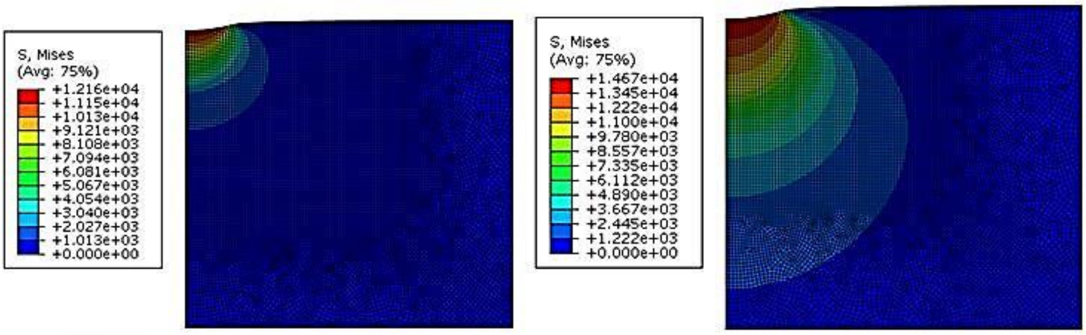

(c) Indentation depth of 764nm

(d) Indentation depth of 1100nm

Figure 4-7: Hydrostatic pressure (MPa) at different indentation depths

The variance effect in dilation angle Ψ and friction angle β on the hydrostatic pressure was observed, and it was found that the hydrostatic pressure decreases with the increase in the negative dilation angle. Also with the increasing friction angle β, the hydrostatic pressure was found to increase.

Fig. 4-8 presents load-displacement plot for different DP constitutive parameters. The values of each DP parameters were optimised periodically using trial and error method to remove the error difference between experimental and simulation results. Although there are other simple computational methods for curve fitting, the trial and error method using FEM was chosen to evaluate generated stresses and pressure contour of silicon during the indentation. The values of dilation angle changed between the two extremes to find the material load behaviour. Any increase in the negative dilation angle was found to decrease the reaction forces and any increase of friction angle was found to increase the reaction forces as well as the computational cost. In the simulation study, DP parameters of property 10 were found as unique parameters to achieve the required agreement (less than 4% error) to the experimental curve.

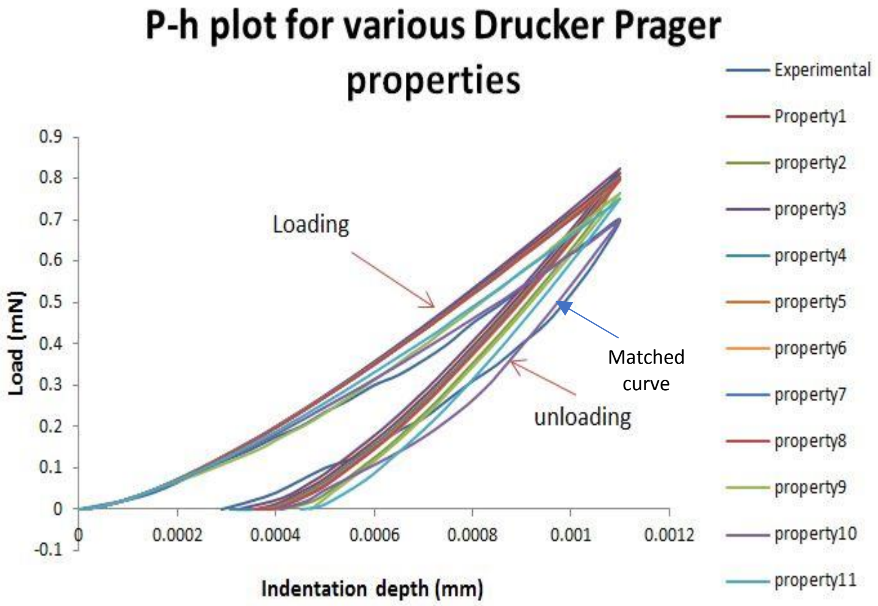

Figure 4-8: Load-displacement behaviour for different DP parameters

4.4.5 Output variables in SPH

Since Abaqus thermal analysis cannot be incorporated into the SPH simulation in Abaqus, the element output variables comprise of mechanical based output variables. For the nodal output variables, all output variables available in Abaqus/Explicit can be obtained in SPH analysis. Abaqus doesn’t offer any direct field output variable to get the relevant information about the mass and volume of the particles. In order to compute the volume associated with SPH particles, it is important to specify the characteristic length. The mass of the particles can be computed from the particle volume.

4.4.6 Summary

This chapter provides a detailed introduction of smoothed particle hydrodynamics approach and its implementation for the simulation of SPDT of silicon. The chapter discusses the limitations of the SPH approach and provides the advantages and justification of using SPH method to simulate the machining of silicon. SPH kernel approximation along with equations of continuity and momentum and the concept of smoothing length are presented in detail. The SPH approach can be implemented in FE code ABAQUS in CAE environment as well as by modifying the input files out of CAE environment. The advantages and limitations of these two methods along with their implementation procedure are described. The steps from the modelling of parts geometry to the selection of output variables and analysis are discussed in detail. Drucker Prager model was selected as an appropriate constitutive model for silicon and its parameters were determined using inverse analysis.

Chapter 5- Determination of Johnson-Cook model constants for silicon

5.1 Introduction

Numerical simulations of cutting process provide a cost-effective way to predict material response behaviour of silicon under different cutting conditions. These simulations can be used to optimize tool geometry and machining conditions without undergoing time consuming “trial-and-error” approach. However, to evaluate the true machining response behaviour of any material, an appropriate constitutive model with its material constants are required to be identified. Johnson-Cook (J-C) model is one of the most exploited thermo-viscoplastic material constitutive models used in the machining process simulations of metals [319, 320, 327]. The aptness of J-C model to predict the elastic-plastic behaviour of silicon and other brittle materials in SPDT has been successfully demonstrated [328-330]. Although J-C parameters of silicon exist in the literature [331, 332], these parameters are obtained through computational methods. There are no J-C constants available for silicon based on an established experimental studies (in the author’s knowledge).

For the rate-independent plasticity models, quasi-static tension, compression and torsion tests are required to obtain material parameters. However, for thermo-viscoplastic models, the parameters are generally obtained through both quasi-static and high dynamic (Split Hopkinson Pressure Bar, Taylor’s impact, etc.) tensile, compression, torsion and shear tests at different temperature and strain rates [333-338].

In this chapter, Johnson-Cook (J-C) constitutive model constants are determined experimentally. Well-established split Hopkinson pressure bar (SHPB) test method was adopted to perform high strain rate tests. Compression tests on the order of 300-1800 s^{-1} were conducted at room temperature to determine strain rate dependent J-C constant. Quasi-static compression tests on the order of 10^{-3}-10^{-1} s^{-1} were performed at room temperature and at elevated temperature to determine model constants related to yielding, strain hardening and thermal softening.

5.2 Johnson-Cook model

Johnson and Cook [318] in 1983 developed a constitutive model to predict the material response behaviour of materials at large strain, high strain rate and at high temperatures. The classical J-C model represents strain hardening, strain rate and temperature.

$$\sigma = [A + B(\varepsilon^{p})^{n}][(1 + C \ln \dot{\varepsilon}^{*})][1 - (T^{*})^{m}] \qquad (5.1)$$

Where σ and ε^{p} are material flow stress and equivalent plastic strain respectively. *A, B, C, m* and *n* are the material constants of J-C model. The constant *A* represents the yield stress at low strain and, *B* and *n* are the strain hardening constant and hardening exponent respectively. The constant *C* represents strain rate effect and *m* is thermal softening constant.

The term $\dot{\varepsilon}^{*}$ is the ratio of non-dimensional plastic strain rate $\dot{\varepsilon}^{p}$ and reference strain rate $\dot{\varepsilon}_0$.

$$\dot{\varepsilon}^{*} = \frac{\dot{\varepsilon}^{p}}{\dot{\varepsilon}_0} \qquad (5.2)$$

and T^* is the dimensionless term known as homologous temperature and described as:

$$\mathrm{T}^* = \frac{\mathrm{T} - \mathrm{T_r}}{\mathrm{T_{melt}} - \mathrm{T_r}} \qquad (5.3)$$

Where T_r and T_{melt} are the reference and melting temperature respectively and T is the current temperature of the material.

In Eqn (5.1), the expression within the first bracket in the model represents stress-strain behaviour at reference strain and temperature. The expressions in the second and third brackets represent strain rate and temperature effect respectively.

5.3 Experimental study

5.3.1 Split Hopkinson Pressure Bar (SHPB) test

The split Hopkinson pressure bar (SHPB), also referred to kolsky bar [339, 340] has been frequently employed to investigate the material response behaviour at high strain rates. For similar values of strain, stresses developed within the material will vary at different strain rates. In this study SHPB compression tests were conducted to obtain the stress-strain response of silicon at strain rates of 300-1800 s^{-1}. A schematic diagram of SHPB test equipment is shown in Fig. 5-1. It consists of a mechanism of a striker bar, an incident bar and a transmitted bar.

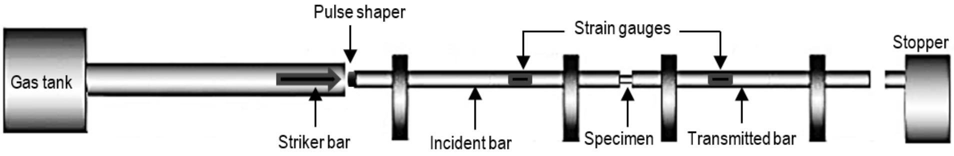

Figure 5-1: Schematic of split Hopkinson pressure bar test equipment

In the study, a pneumatic accelerator was used to fire the cylindrical striker bar of 100 mm with the required velocity. The launcher consists of a high-pressure air reservoir and a 3 m long gun barrel with a bore of 45 mm. The incident bar, transmitted bar and the gun barrel were aligned sufficiently well to provide longitudinal impact. When striker bar is fired, it generates compressive longitudinal stress waves along the incident bar which partially transmits through the test specimen to the transmitted bar and rest reflect back along the incident bar. The principle of the pressure waves generation in SHPB is illustrated in Fig. 5-2

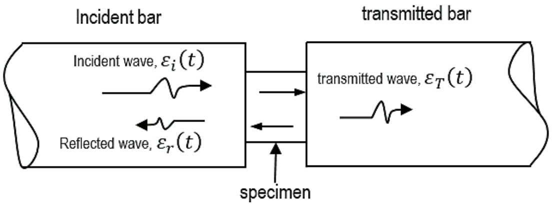

Figure 5-2: Principle of stress waves in SHPB

The transmitted strain ε_T can be calculated from the following relation.

$$\varepsilon_T(t) = \varepsilon_i(t) + \varepsilon_r(t) \qquad (5.4)$$

Where ε_i , and ε_r are incident and reflected strains measured by the strain gauges.

Half-bridge configured Wheatstone bridge with two active foil strain gauges of 3 mm length and a resistance of 120 ± 0.3 Ω and 2.10 ± 1%-gauge factor was used to measure the uniaxial strains. The strain gauges were installed in the middle of the bars to record the strain histories along the incident and transmitted bar and placed in diametrically opposite positions to neutralise the bending movement. The output from the Wheatstone bridge circuit was fed to a voltage amplifier (Fylde Transducer Amplifier type FE-379-TA). The voltage amplifier had an input voltage of 5 V and its gain was set to 1000. The output of the voltage amplifier was fed to the high-speed digital acquisition system module PCI-5105 from National Instruments™. LABVIEW™ programme was used for data acquisition while MATLAB was used to analyse the acquired data. For the half-bridge Wheatstone bridge, the compressive strain (ε_c) can be obtained from the following formula:

$$\mathrm{\varepsilon_c} = \frac{2\mathrm{V_o}}{\mathrm{F.V_{in}}} - \mathrm{\varepsilon_n} \qquad (5.5)$$

Where V_o and V_{in} are the output and input voltages respectively, F is the strain gauge factor and ε_n is the shear strain which was assumed negligible. When introducing the gain effect, the voltage to strain factor was calculated from the following relationship

$$\frac{\mathrm{\varepsilon_c}}{\mathrm{V_o}} = \frac{2}{\mathrm{F.V_{in}.G}} \qquad (5.6)$$

Cylindrical specimens of silicon with 14 mm diameter and 10mm length were used in the tests. Silicon specimens with 99 % purity and with (111) crystal orientation were selected. In order to substantiate the true material response behaviour, three specimens were tested for each strain rate to affirm repeatability of the SHPB test. The specimens were placed between the incident and the transmitted bars. Lubrication was applied on both ends of the specimens to reduce the influence of friction. In SHPB test, it is very important to make the specimen deform homogeneously which help attain the stress data in dynamic equilibrium. The incident and transmitted bars were aligned precisely. The specimen-bars contact surfaces were kept exactly flat. These measures can eliminate any unwanted stress concentration on the specimen edges and help to obtain real failure strength of silicon. as well as The bars were supported with nylon bushes to allow approximately free longitudinal movement. In order to achieve the dynamic stress equilibrium and to achieve the specimen deformation at constant strain rate, a pulse shaper was placed between the striker and the incident bar.

The properties of the incident and transmitted bars and silicon specimen are presented in the Table 5-1.

Table 5-1: SHPB bars and silicon specimen material properties

	Wave speed	Elastic modulus	Density	Fracture toughness	Poisson’s ratio, *v*	Impedance
	(m/s)	(GPa)	Kg/m^3	(MPa m$^{1/2}$)		MRayls
SHPB bars	5000	200	8000			45.7
Si specimen	8025	146	2330	0.83-0.95	0.17	19.7

When specimen deformed uniformly, the amplitude of the reflected wave relates to the strain within the specimen. The average strain ε_s can be determined from the following formula:

$$\varepsilon_s = -\frac{2c_b}{L_s}\int_0^t \varepsilon_r dt \qquad (5.7)$$

The average strain rate $\dot{\varepsilon_s}$ can be calculated using the following formula

$$\dot{\varepsilon_s} = -\frac{2c_b\varepsilon_r}{L_s} \qquad (5.8)$$

Where c_b is the wave speed of the incident and transmitted bars and L_s is the length of specimen before the test. The amplitude of the transmitted wave governs the average (σ_s) stress in the specimen and can be described as:

$$\sigma_s = \frac{EA_b}{A_s}\varepsilon_T \qquad (5.9)$$

Where E is the Young's modulus of the steel bars and A_b and A_s are the cross-sectional area of the bars and the specimen.

5.3.2 Quasi-static compression and tension test

As material properties vary with temperature, quasi-static compression tests at room and elevated temperatures were carried out on material testing machine Instron 8801 with the servohydraulic system. The compression tests were performed at strain rates of 10^{-3} and 10^{-2} s^{-1}, respectively. In the low strain rate test at elevated temperature, the specimens were heated to 360°C in a temperature control oven chamber. The elevated temperature was maintained during the test.

Similar cylindrical specimens tested in SHPB test with 14 mm diameter and 10 mm length were used in low strain rate experiments. All specimens were carefully analysed for any prior damage to avoid any erroneous behaviour.

Three specimens were tested at each strain rate to verify the material deformation behaviour. During the tests, the load was applied continuously at a specified strain rate until material fracture to obtain strain to fracture trend.

5.4 Results and discussion

The sample data obtained from SHPB and quasi-static tests was analysed to determine material response at different strain rates and temperature. In SHPB testing of ductile materials, incident, reflected and transmitted pulses show a plateau after the rise [341]. Fig. 5-3 presents the output signals from the strain gauges attached to the incident and transmitted bars. No significant oscillation was observed on the incident and reflected pulses showing low dispersion effect. The incident, transmitted and reflected pulses were obtained with sharp edges without any plateau. Reflected pulse was obtained before the incident pulse reaches zero in the incident bar. This behaviour attributed to very low pulse flow duration within the specimen due to high stiffness and brittleness of the material.

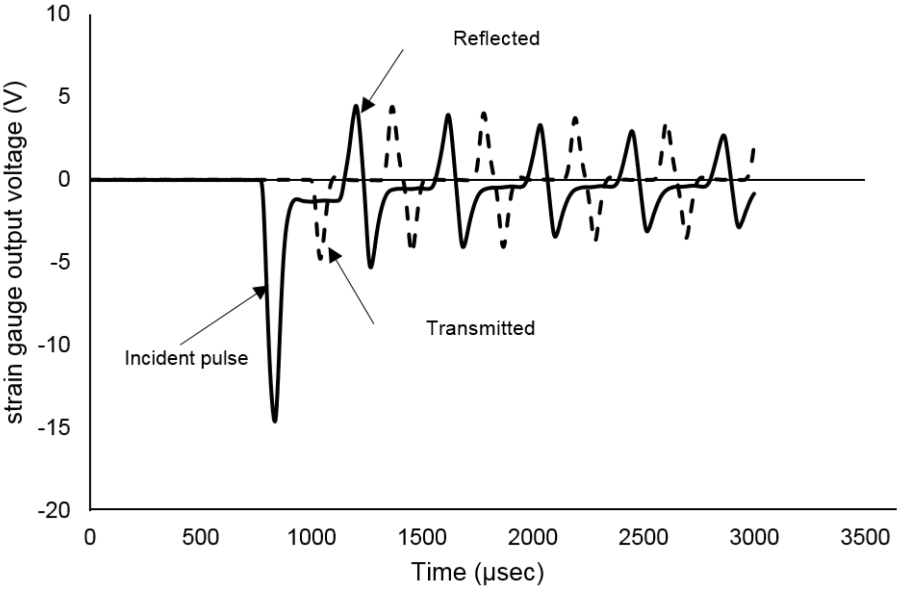

Figure 5-3: Incident and reflected pulse history during SHPB test of silicon

The stress-strain curve trend obtained during the high dynamic tests is presented in Fig. 5-4. The stress in the specimen increases linearly until reaching a peak value. The material fails after undergoing slight plastic deformation,and stresses drop to zero.

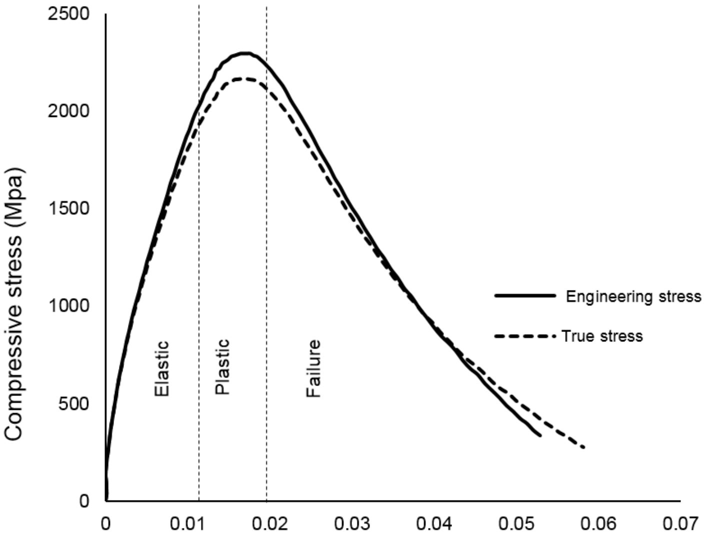

Figure 5-4: Compressive stress trend during SHPB test

In this study in order to get true deformation characteristics of the tested specimens, engineering stress-strain data was converted to true stress-strain data. Fig. 5-5 shows the true stress-true strain behaviour of silicon specimen for the strain rates ranging from 300 s^{-1} to 1800 s^{-1}. It can be seen that with a slow increase in strain rate, the failure strength of silicon increase significantly. The yield strength of silicon increases from 1.6-2.8 GPa with the increasing strain rate. The specimen fails catastrophically after small plastic deformation. Failure strain of the specimens was initially found to increase from 300 to 800 s^{-1} and then decrease when the strain rate is above 800 s^{-1}. Also, with the increase of strain rate, the fragmentation of the silicon specimen increased. The silicon material failed in small fragments in the end.

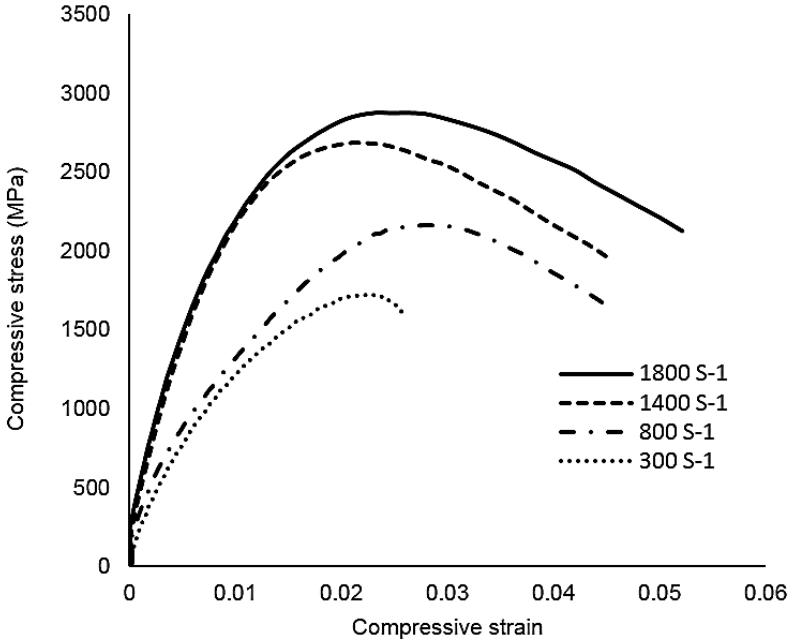

Figure 5-5: Stress strain behaviour of silicon during the SHPB test

The stress-strain behaviour of silicon at room and elevated temperature in the quasi-static compression test is shown in Fig. 5-6. During heating, silicon specimen undergoes thermal expansion in all directions. A great care should be taken when heating the specimens as any applied load (even micro-level) can damage the specimen. In all the compression tests performed, a linear elastic trend was observed under all the strain rates except the thermal test with a slightly curved elastic curve. The specimen experienced very little plastic deformation due to strain hardening until reaching fracture. The observed plastic deformation with strain hardening attributed to the phase transformation from diamond cubic structure to β-tin metallic phase.

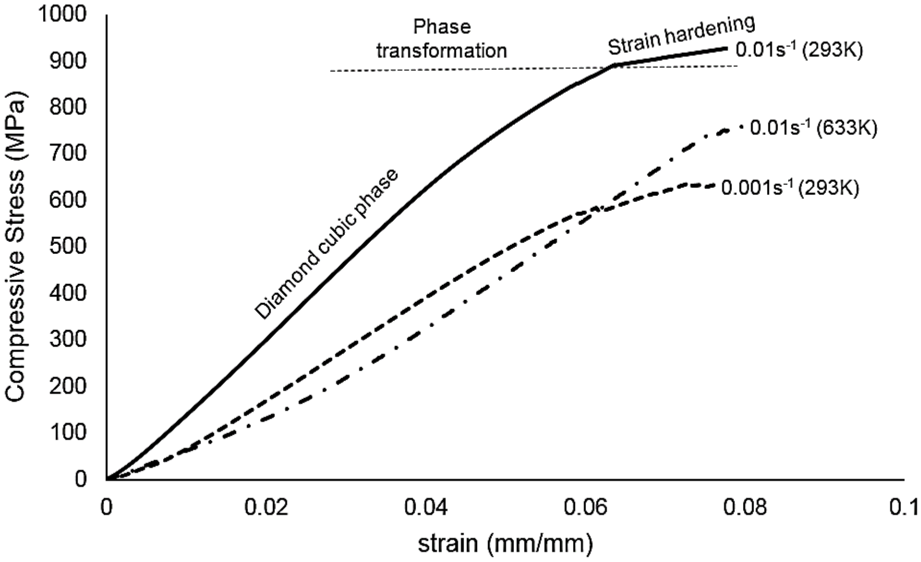

Figure 5-6: Quasi-static stress strain response of silicon at room and elevated temperature

Fracture toughness of silicon was found to reduce with the increase of temperature. Due to thermal softening, under the same strain rate, the specimen endured slightly increasing strains at elevated temperature compared to those at room temperature.

5.5 Determination of Johnson-Cook model constants

J-C constitutive model requires five material constants, i.e. *A, B, C, n,* and *m* to predict the plastic response behaviour of the simulated material. Different methods adopted to obtain J-C model parameters include experimental and computational inverse parameter identification methods [334, 342, 343]. The experimental procedures to obtain these five J-C constants are detailed in Johnson and Cooks's studies [344, 345] . The test data of material response at high strain rate as well as quasi-static strain rate under room and elevated temperatures is needed to determine J-C parameters. The required stress-strain curves can be obtained by tensile, torsion or compression tests. In this study, these constants were determined from the compression tests data obtained through the SHPB test at room temperature, and quasi-static compression tests at room and elevated temperatures. The stress-strain behaviour of silicon as a function of strain, strain rate and temperature was determined.

5.5.1 Determination of J-C model constants A, B and n

The constants *A, B* and *n* from the first bracket $[A + B(\varepsilon^p)^n]$ of J-C model were determined from the quasi-static compression test. The parameter *A* was determined from the yield point in the true stress-strain curve at ambient temperature. To determine the constant *B*, the elastic deformation part before the yield strain was removed from the stress-strain and only the plastic deformation stress strain data was plotted in a log-log graph. The J-C Constant

B and *n* were then obtained by fitting the $(A+B(\varepsilon^p)^n)$ curve with the effective plastic stress-strain curve on the log-log graph in Fig. 5-7.

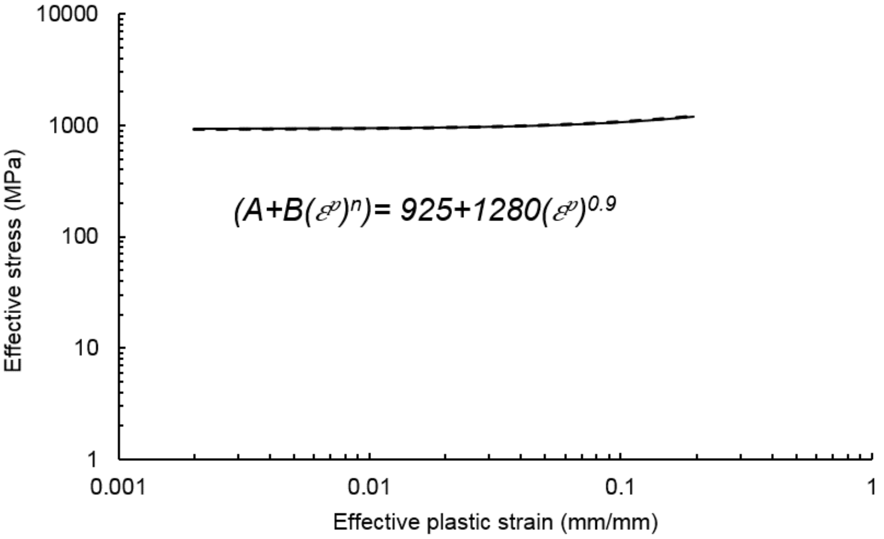

Figure 5-7: Log-log plot of true effective plastic stress-strain curve

5.5.2 Determination of constant C

The J-C constant *C* was determined from best fitting the SHPB stress-strain experimental curves with the J-C material model. Since dynamic tests were performed at room temperature, the thermal softening effect can be neglected in J-C model when specimen temperature is assumed at the same room temperature. The plastic stress-strain curves are then fitted with the following reduced J-C model

$$\sigma = \left[A + B(\varepsilon^{p})^{n}]\right[\left(1 + C\ln(\frac{\dot{\varepsilon}^{p}}{\dot{\varepsilon}_{0}})\right)\right] \qquad (5.10)$$

The values of *A, B* and *n* obtained in the previous section were introduced in Eqn (5.10) with the average and reference strain rate values.

5.5.3 Determination of constant m

In order to determine the thermal softening constant *m*, quasi-static compression tests were performed at the same strain rate ($\dot{\varepsilon}^p = 0.01$) and at room and elevated temperature. *m* was determined from the following formula:

$$\mathrm{m} = \frac{\log(1-\mathrm{k})}{\log\mathrm{T}^*} \qquad (5.11)$$

where *k* can be described as:

$$\mathrm{k} = \frac{\sigma_\mathrm{e}\,(\varepsilon_*^\mathrm{p}, \dot{\varepsilon}_*^\mathrm{p})}{\sigma_\mathrm{r}(\varepsilon_*^\mathrm{p}, \dot{\varepsilon}_*^\mathrm{p})} \qquad (5.12)$$

In Eqn (5.12) σ_r and σ_e are the stress value for a specific plastic strain (ε_*^p) and strain rate ($\dot{\varepsilon}_*^p$) at room and elevated (high) temperatures respectively. The values of *k* are determined for different plastic strains and an average value was taken in Eqn (5.11). The obtained J-C parameters are presented in the following table.

Table 5-2: The obtained Johnson-Cook parameter for silicon

J-C parameters	A	B	C	N	m
Silicon	925	1250	0.084	0.9	0.98

5.6 Validation of Johnson-Cook constants

In order to assess the validity of determined J-C constants, an experimental trial and finite element simulation study of diamond turning of silicon were performed in this work. Simulation of silicon was carried out using smoothed particle hydrodynamics (SPH) method. J-C constitutive model with experimentally determined constants was adopted to evaluate the cutting behaviour of silicon. Since the constitutive model does not account for brittle behaviour, negative rake angle tool was used to simulate the ductile material removal of silicon. Cutting tools with negative rake angle provide required high hydrostatic stress to achieve high-pressure phase transformation (HPPT) of brittle silicon into ductile metallic phase [7]. Results from the SPH cutting simulations were compared with diamond turning experiments.

5.6.1 Experimental setup

The single point diamond turning (SPDT) trial was performed on an ultraprecision diamond turning machine (Precitech Nanoform 250 ultragrind). The machine has air bearing spindle, hydrostatic oil bearing slideways of high stiffness and liquid cooled slides to maintain thermal stability. A three-component force dynamometer Kistler (9256C2) was used to monitor the cutting forces. The polished surface of P-type single-crystal silicon wafer with (111) crystal orientation and subnanometer surface finish was machined. A round nose single crystal diamond tool with dodecahedral orientation was used in the cutting trial. Table 5-3 lists the tool and workpiece data and machining conditions.

Table 5-3: Work/tool geometries and machining conditions in the cutting trial

Silicon wafer	Diamond tools	Cutting parameters
Diameter = 50 mm	Orientation = Dodecahedral	Spindle speed =1200 rpm
Thickness = 5 mm	Rake angle = -25 °	feed rate = 1µm/rev
Orientation = (111)	Nose radius = 2 mm	Depth of cut = 10 µm
Sample purity = 99.999%		Coolant = Distilled water

5.6.2 SPH model of machining

The SPH simulation setup of diamond turning of silicon is shown in Fig. 5-8. The tool was kept rigid and meshed with eight-node elements with reduced integration (C3D8R). The workpiece consisting of PC3D particles was modelled as a deformable part. In order to obtain true material response behaviour of silicon, the optimum SPH particle density was determined using convergence analysis based on von Mises stress criteria. The particles density was kept homogeneous in the chip formation zone to avoid any artificial stress concentration during cutting.

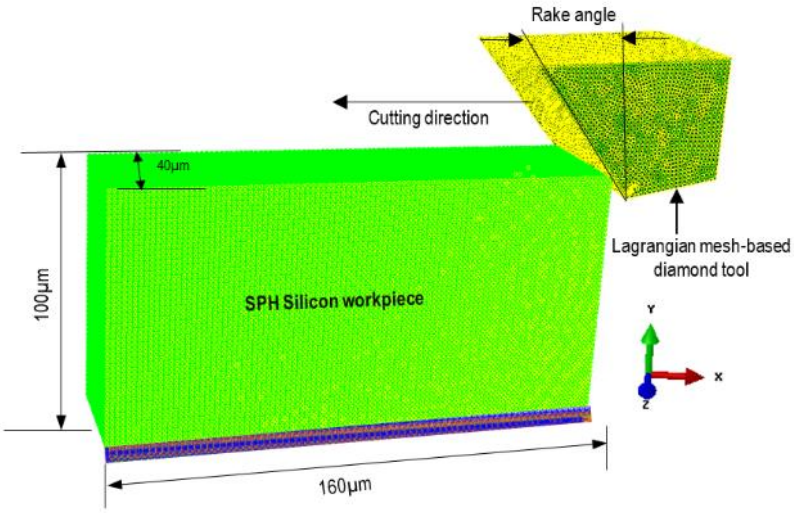

Figure 5-8: Cutting model of SPDT of silicon using SPH method

In order to achieve high stiffness during cutting, the bottom surface of the workpiece was fixed. The velocity was applied to the cutting tool in the negative X-direction. The tool motion was constrained in Y and Z-direction. In SPH simulation, tool rake angle, cutting speed and depth of cut were kept as the same values as those in the experiment. Table 5-4 lists the cutting parameters and conditions adopted in SPH simulation.

Table 5-1: Cutting parameters and conditions in SPH simulation

	Workpiece	Tool
Material properties and conditions	Dimensions = 160x100x40 µm Depth of cut = 10 µm SPH particles = 140143 Density, ρ =2.3 x10^{-9} tonne/mm3 Elastic modulus, E = 146 GPa Poisson's ratio = 0.2	Rake angle =-25° Clearance angle = 10° Cutting speed = 3.4 m/s

5.6.3 Experimental and simulation results

5.6.3.1 Von Mises and hydrostatic stress analysis

Fig. 5-9 shows the von Mises and hydrostatic stress components obtained during numerical simulation of silicon. At steady-state condition, the von Mises stress of 10 GPa was found in the primary deformation zone. Since, the stress level reached well beyond the yield strength of silicon [346, 347], plastic deformation was the dominant machining mode. The von Mises stress values obtained during SPH simulation were found similar to that seen in machining of silicon [328, 348].

During loading conditions, the threshold hydrostatic stress for the HPPT of silicon from diamond cubic to β-tin and other phases is ~10 GPa [56, 349, 350]. The high hardness of silicon contributes to this high hydrostatic stress during cutting. During the SPH simulations, the average value of hydrostatic pressure in the primary deformation zone was found to lie in the range of 12-14 GPa. The von Mises and hydrostatic stress results from the SPH simulation clearly match the machining conditions of silicon. This machining response behaviour during simulation justifies the appropriateness of J-C constants for silicon.

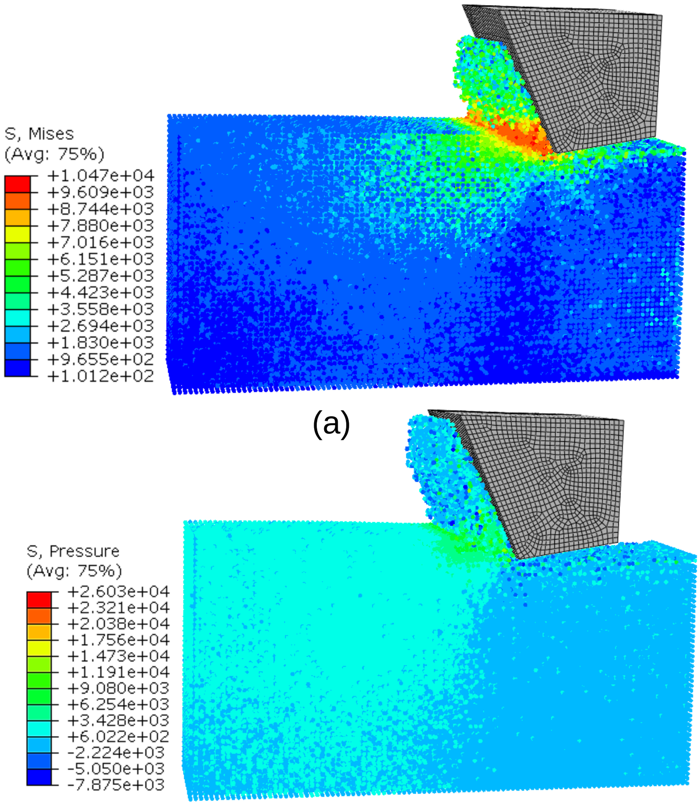

(a)

(b)

Figure 5-9: SPH simulation results: (a) Von Mises stress distribution (b) Hydrostatic stress distribution

5.6.3.2 Comparison of machining forces

Cutting force is an important factor in the cutting process to characterize the material resistance to cutting. Since experimental and corresponding simulated conditions were kept identical, machining forces can be a determining factor to validate the J-C models. Fig. 5-10 shows the comparison plot of normal forces obtained from the experimental trials and SPH simulation of machining.

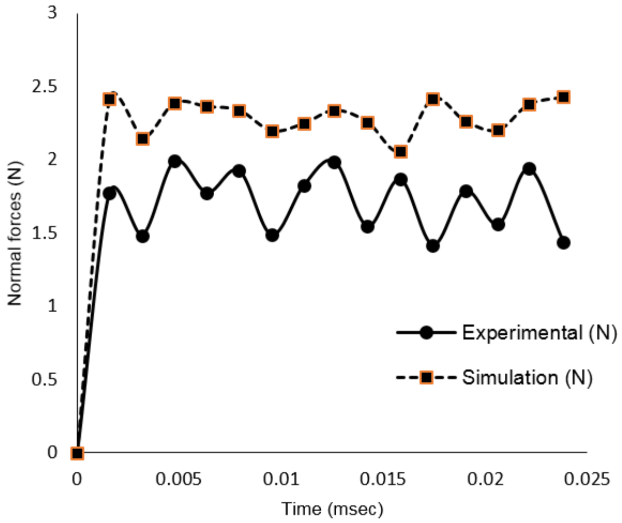

Figure 5-10: Comparison of cutting forces obtained from experimental and SPH simulation

A steady trend of forces was observed after the initial tool-workpiece contact in both the SPH simulation and experimental studies. The normal forces from the simulation were found slightly higher than the corresponding experimental forces. Since machine stiffness as well coolant effects has not been considered to avoid complexity of simulation, this difference is in reasonable agreement.

5.7 Summary

In order to predict the plastic deformation of silicon, the material constants of Johnson-Cook model were determined experimentally. Quasi-static as well as high strain rate tests were conducted to determine the failure behaviour of silicon at different strain rates. The J-C parameters related to yielding, strain hardening, strain rate and thermal softening were determined from the data obtained at high strain compression tests at room temperature and low strain compression test at room and elevated temperatures. A significant difference in the yield strength of silicon from 950 MPa to 2.8 GPa was observed when the strain rate increase from quasi-static to dynamic conditions. Very small plastic deformation with strain hardening was observed. The failure strain was found to reduce with the increase of strain during quasi-static tests. The determined J-C constants were validated using experimental and smoothed particle hydrodynamics study of machining. Von Mises stresses, hydrostatic stress and cutting forces obtained during SPH simulation compare favourably with experimental results.

Chapter 6: Investigation of tool rake angle effect in SPDT of silicon

6.1 Introduction

A comprehensive understanding of coherence of silicon machining mode and tool geometry is imperative to achieve cost-effective and efficient SPDT by realising prolonged ductile mode machining at reduced tooling cost. The major reported work in the past reveal the significance of HPPT as a function of tool geometry which facilitates plastic deformation of silicon and accordingly influence tool wear mechanism [7, 62, 351]. Although negative rake angle is commonly agreed to be very important in achieving brittle to ductile transition (BDT) of silicon, a clear disagreement pertaining to optimal rake angles for ductile mode machining can be found in the literature. Also, an important factor to consider is the capability of worn tools of different rake angle tools to maintain HPPT for longer ductile mode machining. Therefore, there is a need to recognize an optimal rake angle that could maintain HPPT-based longer ductile mode machining and at the same time offer reduced tool wear.

In this chapter, an investigation of the effect of tool rake angle in SPDT of silicon using experimental and simulation methods is presented. Machining trials under the same cutting conditions were carried out using three different rake angle tools. In order to delve further into the rake angle effect on the output parameters including material removal, hydrostatic pressure, stresses, and crack formation, at the onset of chip formation and steady-state conditions, a simulation study using SPH approach is performed.

6.2 Experimental study

The SPDT of silicon with high surface quality and minimal sub-surface damage is only possible with stiff machine tools. In this research, machining trials were carried out on an ultra-precision diamond turning machine – Nanotech 250 UPL (Moore Nanotech system) which is equipped with air-bearing spindle offering low friction and less heat generation and hydraulic motional slides of high stiffness.

Single crystal diamond tools in dodecahedral crystal orientation were used to machine P- type silicon wafers of (111) crystal orientation. Fig. 6-1 shows the machining setup and SEM image of negative rake round edge tool used in SPDT of silicon. Three different negative rake angle tools were used in order to investigate the effect of rake angle on surface generation mechanism of silicon.

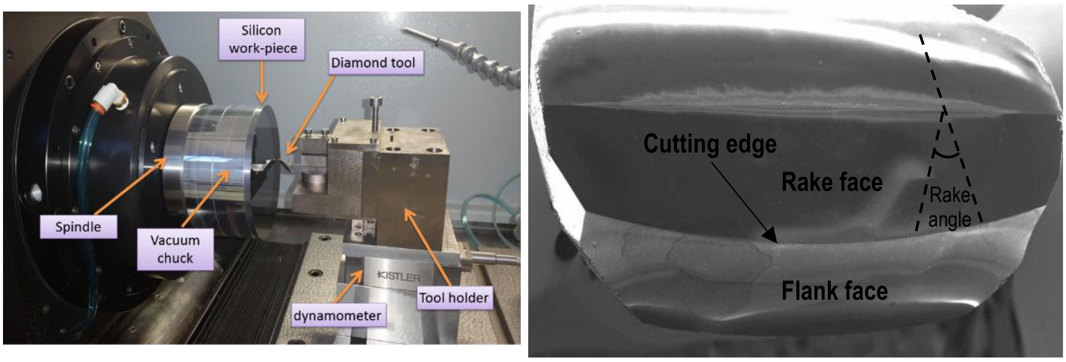

Figure 6-1: Experimental setup of SPDT of silicon and SEM image of new diamond tool

New diamond tools were examined under SEM for any prior damage on the cutting edges and rake and flank faces before machining silicon. The selection of cutting parameters and coolant was based on previous established research work of diamond turning of silicon to attain high optical quality machining [352]. Large nose radius tools were used as they provide strong edge geometry to withstand higher frictional resistance and higher cutting forces. Critical depth of cut as well as critical feed rate for brittle to ductile transition were also found to increase with increasing nose radius during SPDT of brittle materials [353, 354]. Table 6-1 presents tools and workpiece details and machining conditions adopted in the experimental work.

Table 6-1: Tool and workpiece data and machining conditions

Silicon wafer	Diamond tools	Cutting parameters
Optical grade silicon, polished Round Orientation = <111> +/-5 degree Diameter = 100mm Thickness = 5mm Sample purity = 99.999%	Orientation = Dodec Nose radius = 5mm Rake/Clearance angle: • Tool1= -25/10 • Tool2= -30/10 • Tool3 = -40/25	Spindle speed =1200rpm feed rate = 1µm/rev Depth of cut = 10 µm Coolant = Distilled water

Each silicon wafer was divided into two zones: facing and plunge zones. The cutting was performed with a reiteration of facing cuts by reduction of 1mm in retracting radius for each following facing cut. Each silicon wafer was repeatedly machined with the same 10 µm depths of cut and 1 µm/rev cross-feed until the onset of the brittle fracture.

Cutting forces were monitored and recorded using a three-component Kistler dynamometer 9256. An advanced data acquisition system with Dynoware software was used to get the Fx, Fy and Fz forces. Surface roughness was measured using a white light interferometry (Zygo Newview 5000) for each iteration of facing cuts. The tools were monitored after machining under SEM for any induced wear or damage caused by the machining trials. The cutting distance was calculated for each diamond tool before the onset of brittle fracture to measure tool performance.

Confirmation trials were also performed using the same tool and workpiece geometries, orientations and machining conditions. The methodology for monitoring tool conditions, cutting forces and surface finish were the same adopted in the first trial.

6.3 SPH simulation model

The tool was modelled with eight-noded C3D8R elements using Lagrangian element-based mesh and was kept rigid due to significantly high modulus of diamond compared to silicon. The workpiece was modelled as a deformable part with PC3D particles to handle large deformation during the cutting process. The workpiece dimensions were kept at (200x100x50) µm. The bottom of the workpiece was retained in all directions. In cutting simulation, the tool moves with similar experimental cutting velocity in the negative x-direction. Fig. 6-2 shows a cutting simulation model used in this study.

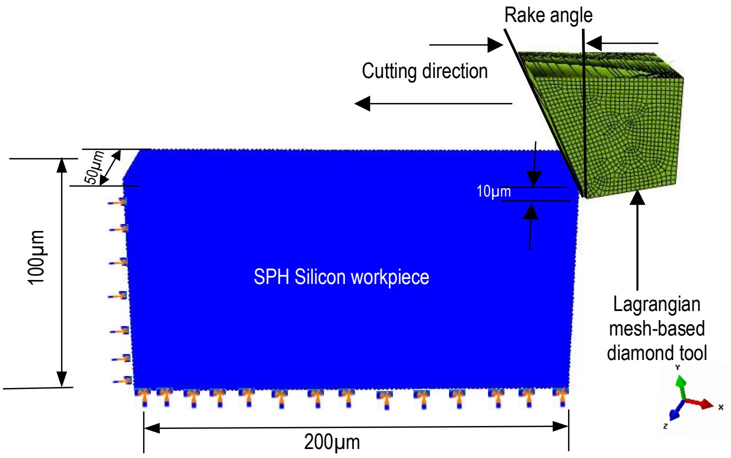

Figure 6-2: SPH cutting simulation model of silicon

In order to examine the rake angle effect, cutting simulations were performed with four different rake angle tools using the same cutting conditions adopted in experiments. Table 6-2 shows the cutting parameters used in the simulation study.

Table 6-2: Cutting parameters used in SPH simulations

	Rake/clearance angle	Workpiece dimensions (µm)	Cutting speed (m/s)	Depth of cut (µm)
1	+5/10	200x100x50	6.3	10
2	-25/10			
3	-30/10			
4	-40/10			

Table 6-3 lists the material properties of silicon along with DP model parameters used in SPH cutting simulation.

Table 6-3: Material properties of silicon

Density, ρ	2330 kg/m^3
Elastic modulus, E	146 GPa
Poisson's ratio,	0.2
Friction angle (β)	26
Dilation angle(Ψ)	20
Flow stress ratio, k	0.82

6.4 Results and discussion

SPDT of silicon using three different rake angle tools was carried out until the onset of brittle fracture. Due to the high anisotropy of silicon, machining mode is dependent on crystallographic orientation based on the orientation of dislocation and slip system relative to cutting direction. Fig. 6-3 shows the diamond turned silicon wafer with severe brittle fracture appeared in a three-fold symmetry pattern.

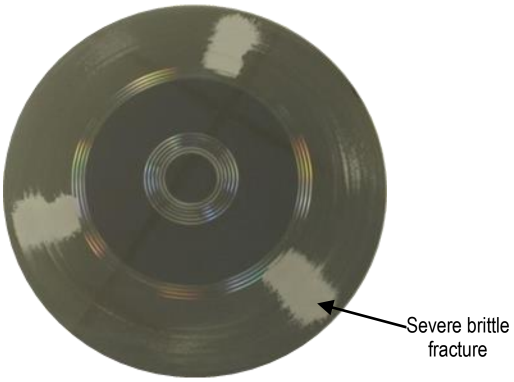

Figure 6-3: Brittle fracture in 3-fold pattern after SPDT of silicon

The results of output parameters obtained using different rake angle tools were recorded and discussed in the following sections. Tool rake angle is considered as a determining factor of surface generation mechanism in SPDT of silicon. In order to investigate the rake angle effect, cutting forces, stresses, hydrostatic pressure, chip formation and tool wear were measured and analysed for different rake angles.

6.4.1 Cutting forces

Cutting forces are considered as the most accredited indicator to characterise material removal modes, frictional resistance to cutting, as well as tool wear. Cutting forces were recorded in each facing cut for all rake angle tools. Although cutting temperature has a significant effect on cutting forces magnitude as high cutting temperature during machining results in softening of the material as well as change of machining mode, cutting temperature during SPDT of silicon didn’t recorded high enough [328, 355] to cause any softening of material, and therefore shouldn’t affect the cutting force magnitude significantly.

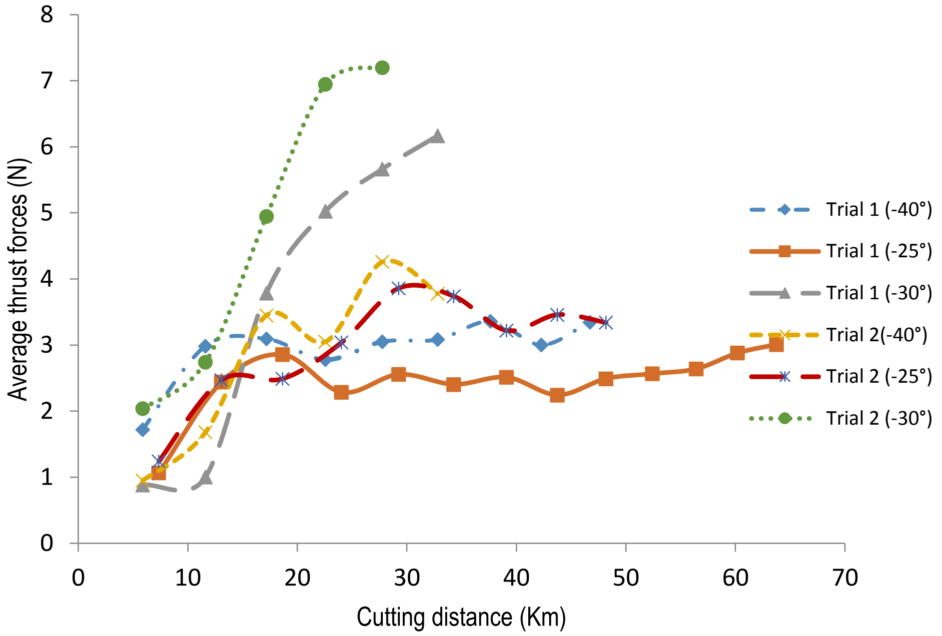

Figure 6-4: Thrust forces trend with cutting distance

Fig. 6-4 presents average thrust forces recorded in trial 1 and trial 2 with respect to cutting distance for different rake angle tools. In both the trials, diamond tools with -25° rake angle attained the longest cutting distance before the onset of brittle fracture followed by -40° rake tools. With the increasing cutting distance, tool wear develops which results in an increase of cutting forces. Cutting forces trend suggest the maximum tool wear rate from 0-20km and then gradual frictional wear for the rest of the cutting distance. This phenomenon substantiates the understanding of higher wear rate of sharp edges of new tools due to stress concentration in the cutting edge zone. For -30° rake angle, the tool achieved the least cutting distance with the sharp rise of cutting forces. Similar cutting forces behaviour of -30° rake tool was recorded during the confirmation trials.

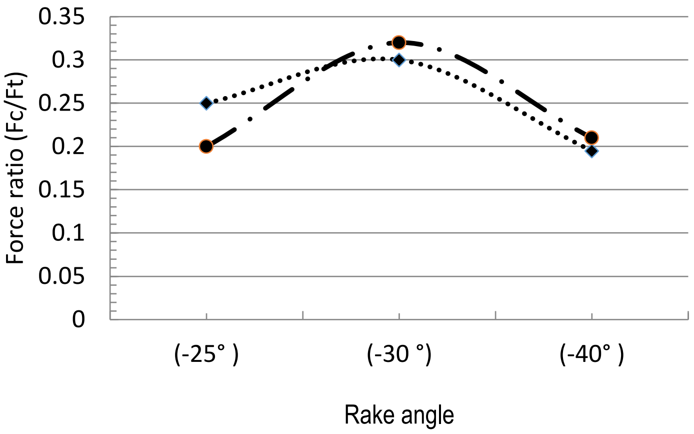

Figure 6-5: Force ratio trend with decrease rake angle

Fig. 6-5 presents the tangential to thrust force ratio for the three different rake angle tools. Although for the -30° rake tool, the thrust forces were found higher than tangential forces, the relative magnitude of the tangential force is higher than the other two tools. This explains the dominant cutting phenomenon with reduced compressive stresses and hence early brittle fracture.

Machining forces were measured in SPH cutting simulation of silicon using different rake angle tools. Fig. 6-6 presents a comparison of experimental and simulation-based mean thrust forces. A good correlation of forces can be seen for -25° and -40° rake angle tool except -30° rake tool for which the percentage difference increased to 30% between experimental and simulation values. This high difference could possibly due to the rake angle effect of -30° of large 5mm nose radius towards orientation dependent cutting direction during experimental machining trials of (111) silicon wafer and require further investigation.

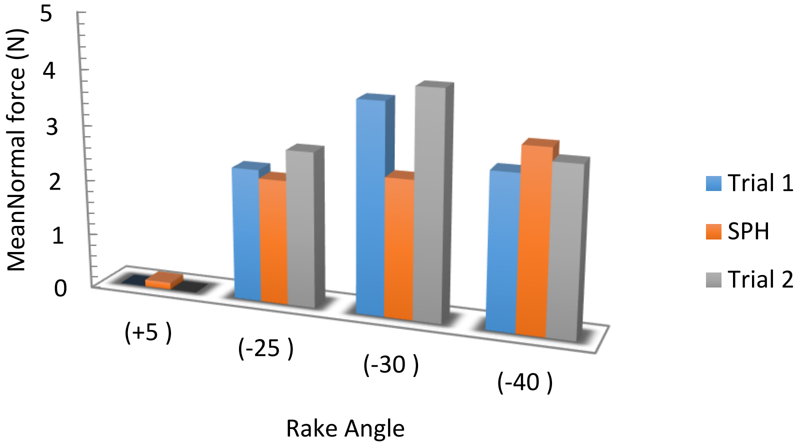

Figure 6-6: Comparison of experimental and simulation cutting forces

6.4.2 Stress distribution and chip formation

The geometry of the primary shear zone (PSZ) is governed by the shear plane angle ($\emptyset_s$) and the ratio of the length of PSZ (L_{AB}) to its thickness (t_p). Fig. 6-7 presents the change of shear plane length and shear angle with the change of rake angle. With the increase of shear zone area, the strength of the material increases and hence increases in deformation energy. It can be noted that shear angle reduces with the increase in negative rake angle from -25° to -40°. Although shear plane area and shear strain magnitude increase with increasing negative rake angle tool, the length of PSZ decrease from -25° to -30° and then increases for -40° tool.

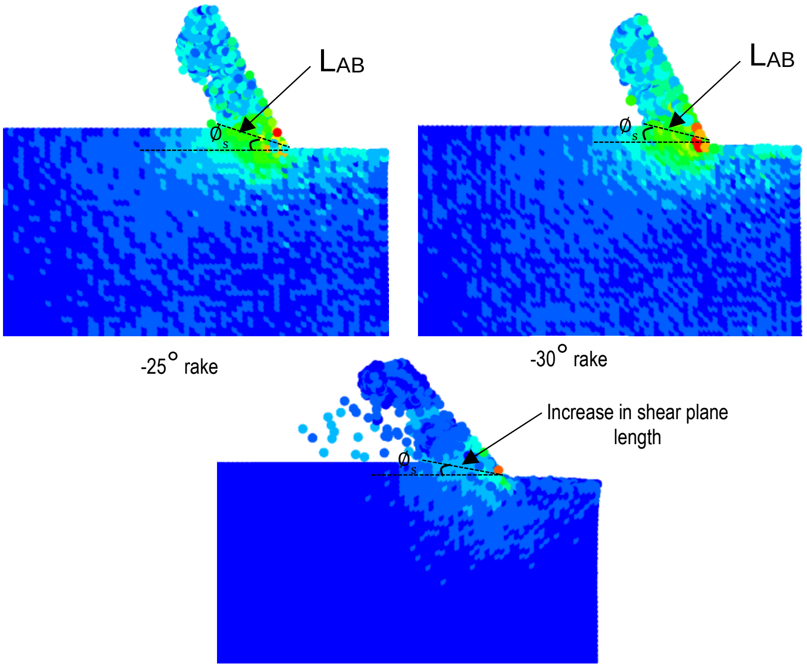

-25° rake

-30° rake

-40° rake

Figure 6-7: Change of shear plane length and shear plane angle

Stresses and pressure distribution and chip formations were also investigated in cutting simulation with different rake angle tools. Von Mises stresses were found to increase beyond the theoretical yield strength of silicon for all negative rake angle tools and continuous material removal observed throughout the cut. For the +5° rake angle tool, although, at first contact, the maximum von Mises stress reached 10GPa at tool-chip interface in the primary deformation zone, material separation initiated by a crack in front of tool tip propagating in the forward direction. Fig. 6-8 shows the crack formation and surface damage on the removal of chip segment using positive rake tool.

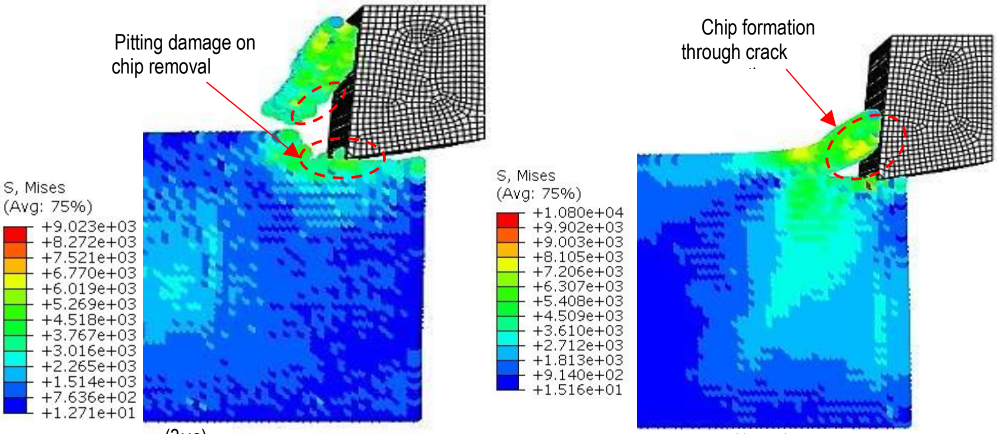

(3µs)

(1.5µs)

Figure 6-8: chip formation using +5° rake angle tool

Bending stresses develop at the bottom surface of the chip and broken chips can be observed from the initiation to the concluding stage of chip separation. An average hydrostatic static pressure of 4GPa was recorded during the chip formation at the steady-state condition. Due to lack of required hydrostatic pressure under the tool tip, chip separation occurs due to developed cracks and result in discontinuous material removal. On the removal of chip segment, surface ahead of the tool undergoes pitting damage under the cutting depth. The direction of developed crack also defines the final machined surface as any crack propagation angle towards the final machined surface result into brittle damage.

Fig. 6-9 shows the von Mises stresses and the variation of chip formation for different negative rake angle tools. An imperative aspect to notice was the variation of stresses with an increase in negative rake angle. In general, an increase in stresses is likely to be predicted with an increase of negative rake angle. Nevertheless, at contact stage, von Mises stresses were found higher for -25° rake than -30° and -40° rake tools. Since lower negative rake tools are likely to initiate chip formation along with compressive stress at first contact with the workpiece surface, shear stresses remain dominant than compressive stresses. With the increasing negative rake, compressive stresses surpass shear stresses at initial contact with the workpiece surface.

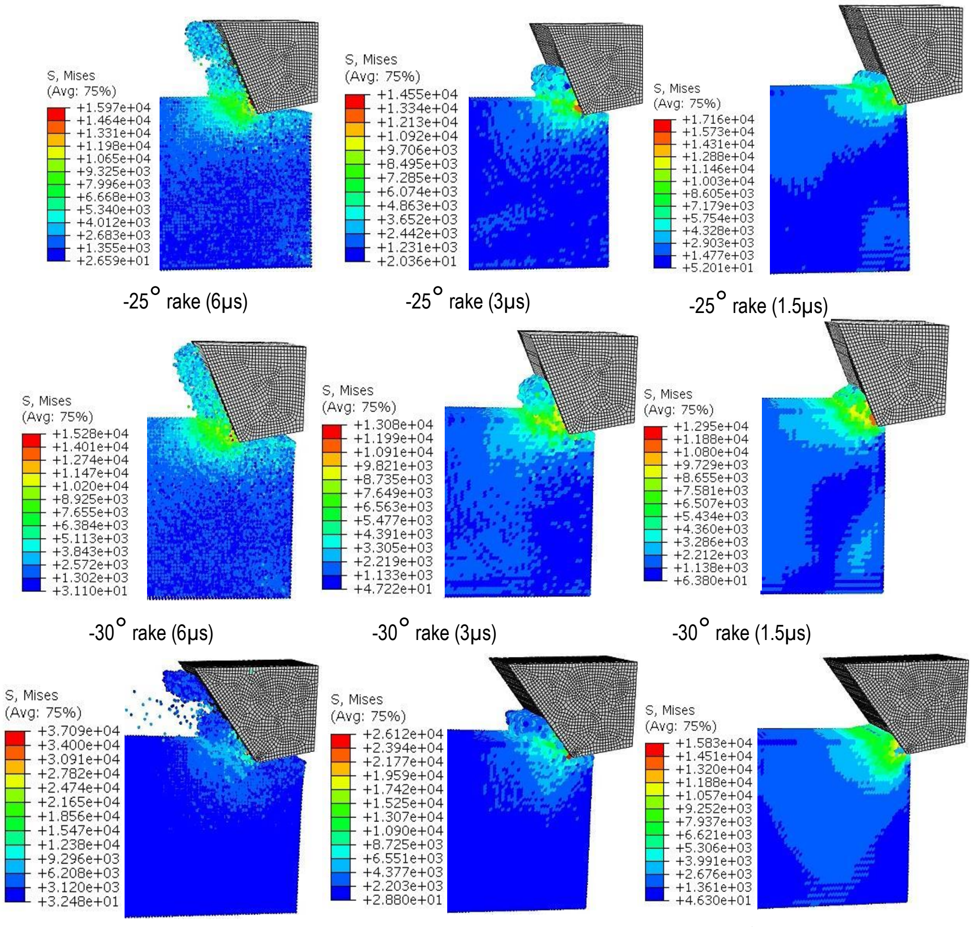

-25° rake (6µs) -25° rake (3µs) -25° rake (1.5µs)

-30° rake (6µs) -30° rake (3µs) -30° rake (1.5µs)

-40° rake (6µs) -40° rake (3µs) -40° rake (1.5µs)

Figure 6-9: Von-mises stresses and chip formation for different rake angle tool from initial to steady-state

At steady-state conditions, developed stresses for -40° rake tool significantly increased than other two tools. This phenomenon attributed to the increase of yield strength of silicon with increasing hydrostatic stress using higher negative rake angle tools. However, for -30° rake angle, von Mises stresses at initial and steady-state conditions were found lower than the -25° rake tool. This behaviour validates the shortening of shear plane length using -30° tool in Fig. 6-7 which results in a decrease of von Mises stresses. The failure stresses can also influenced by the intensity and sequence of compressive and shear stress from incipient to steady-state condition as a function of rake angle. Also, the type of chip formation ahead of the tool contributes to the normal and shear stress distribution on the tool rake face and cutting edge.

In SPDT of silicon, chip contour in secondary deformation zone (SDZ) also influence by the unloading conditions. In machining, the unloading mainly transpires at machined surface behind the tool edge as well reduce loading condition develop at tool-chip interface in SDZ. This change affects machined surface and chip contour in SDZ which can be observed in Fig. 6-9 For the -25° tool, the chip breaks into segments and particles in SDZ. The severity of the disintegration into particle was observed higher for -40° compared to -25° tool. For -30° tool, the chip remained continuous without breakage. In order to further investigate this behaviour, pressure distribution study was performed.

6.4.3 Chip geometry

A good correlation of chip formation was found in experimental and SPH machining studies of silicon. Fig. 6-10 shows the SEM images of silicon chips collected in the first facing cuts for the three rake angle tools. Chips were formed in the combination of continuous, broken and powder form with different thickness. For -25° rake angle tool, chips were mainly formed in combination of continuous and broken chips along with dominant powder form. Smoother and longer ribbon type chips were observed using -30° rake angle tool. Similar behaviour can be observed in SPH simulations where for -30° tool, chips remain continuous in the SDZ. Whereas for -25° and -40°, chips were found to break into particles due to unloading effect.

For both -25° and -40° tools, although the chips were found in the combination of ribbon, broken and powder form, the chip shapes were observed distorted using -40° tool. The distortion could possibly due to the flow of chip under the tool with high compressive stresses.

Tool wear in SPDT of silicon has previously been attributed to the formation of SiC and diamond-like carbon particles [356], or dynamic hard particles [357] scratching or ploughing on the tool flank face forming groove wear. The chemical reaction of diamond carbon and silicon at a high cutting temperature of 959k [355] in the presence of oxygen may lead to the formation of silicon carbide. The formation of SiC due to the silicon-carbon reaction is a significant factor to investigate as it affects material removal mechanism and tool wear. After machining, Energy-dispersive X-ray spectroscopy (EDX) analysis was performed on all the chips collected during all facing cuts using three different rake angle tools.

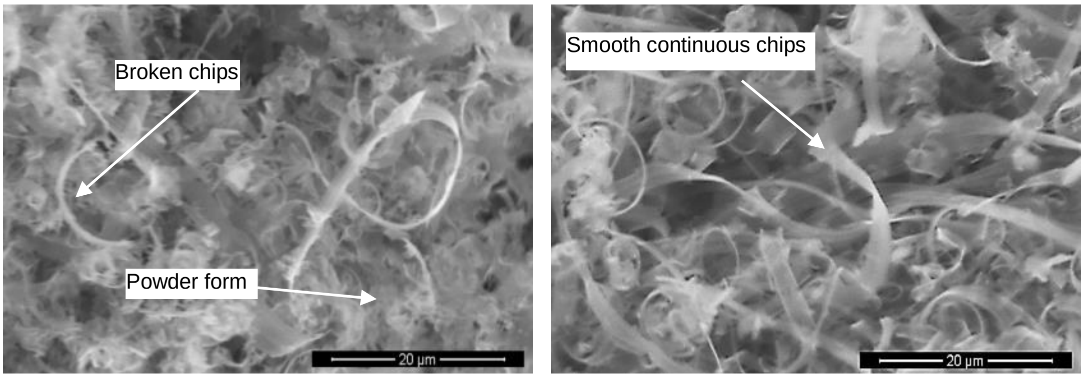

-25° rake tool

-30° rake tool

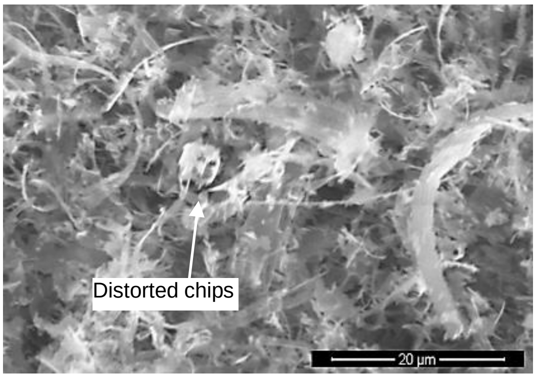

-40° rake tool

Figure 6-10: SEM images of silicon chips for different rake angle tools

Chips collected during both ductile machining and brittle machining were analysed for the presence of SiC. No trace of SiC formation detected in all the chips analysed during EDX analysis. Fig. 6-11 presents the EDX spectrum of collected silicon chips in SPDT study.

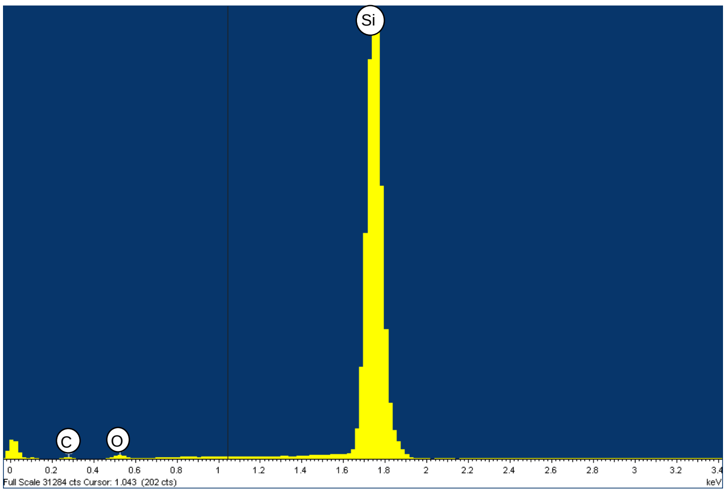

Figure 6-11: EDX spectrum of silicon obtained in SPDT

6.4.4 Tool wear

Tool wear study carried out using scanning electron microscopy (SEM) and diamond tools were inspected for any initial damage prior to machining. The results were evaluated by comparing before and after SEM measurements. Previous studies suggest that abrasive, chemical and thermal wear mechanisms are the possible wear in SPDT of silicon [84, 85, 356]. Typically, multiple tool wear mechanisms can be active but only one tool wear mechanism is dominant for a specific workpiece material and for a certain cutting regime. In both the trials of this study, mainly frictional groove wear at flank face was found dominant for all the tools. Tool wear started at the cutting edge shifting the edge towards the rake face and making grooves on the flank side of the tools. This is due to maximum stress intensity and maximum friction found at cutting edge and trailing flank surface. For the -25° diamond tool, the pitting damage was also observed at the rake face of the tool in both the trials.

The pitting damage was found mainly due to chipping phenomenon. For the other two tools, no crater wear was observed in both the trials. Fig. 6-12 shows the SEM images of diamond tool indicating crater wear and flank wear of -25° diamond tool.

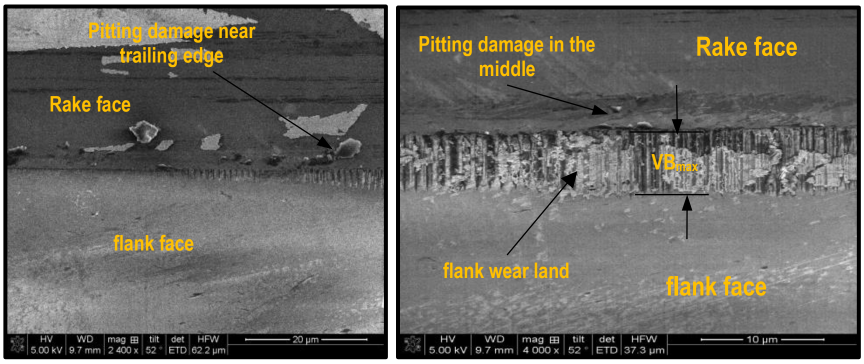

Figure 6-12: SEM image of flank and crater wear of -25° rake tool

Fig. 6-13 presents the frictional groove wear contour in all three tools appeared after machining silicon. Uniform width of flank wear land was found in the middle of cutting edge narrowing down in the form of the curve towards the edges. The flank wear land width for -40° rake tool was recorded 3µm much smaller than 6.5 µm and 7.5 µm for -30° and -25° rake angle tools respectively. This possibly due to the clearance angle of 25° compared to 10° for the other two tools.

A crack found to appear in the wear land area of -25° rake angle tool connecting rake and flank faces of the tool. Although high thermal conductivity of diamond tool and silicon along with coolant significantly contributes to reducing the cutting temperature, with the increased frictional resistance due to wear, cutting temperature may increase significantly.

Diamond tools tend to undergo thermal cracking and chemical wear at higher cutting temperatures. The crack appeared in the wear land of -25° rake tool can possibly be the result of thermal cracking, rapid heating and cooling, or fatigue in achieving the longest cutting distance.

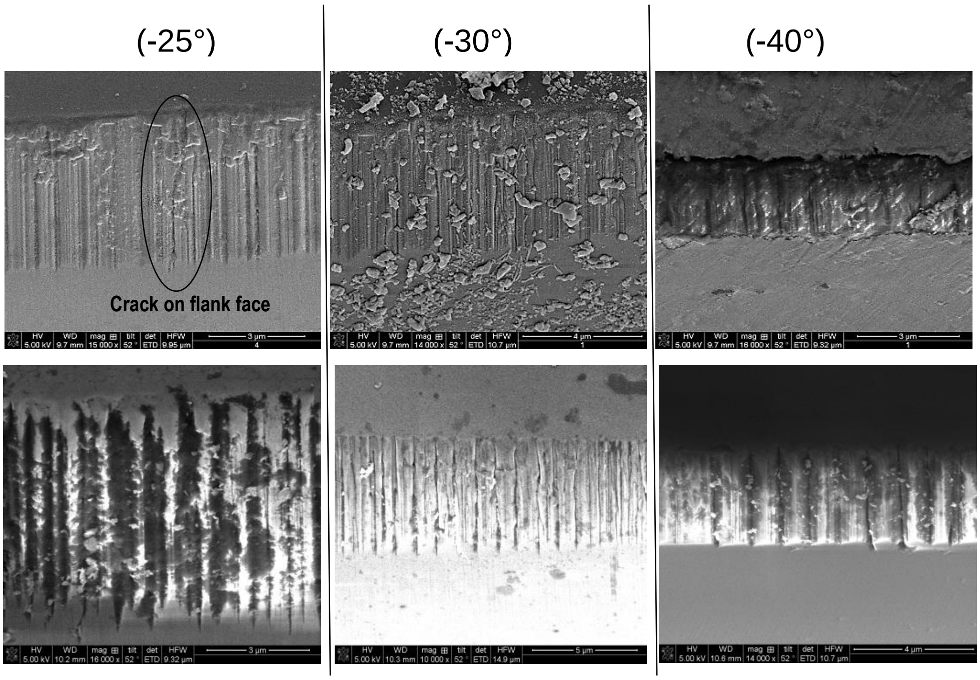

Figure 6-13: Tool wear pattern for different rake angle tools in trial 1(top) and trial 2 (bottom)

While considering tool wear, a significant factor to consider is gradual tool degradation as a function of cutting distance. Fig. 6-14 shows tool wear resistance performance based on the cutting distance where Wa/Cd is the ratio of tool wear area to cutting distance. Although the least ratio for (-40°) rake found in agreement with a previous study [358], which suggest less tool wear for large negative rake tools, the results don't constitute a direct proportionality relationship of decreasing tool wear with increasing negative rake angle. The tool with -30° rake found to undergo the highest tool wear than -40° as a function of cutting distance.

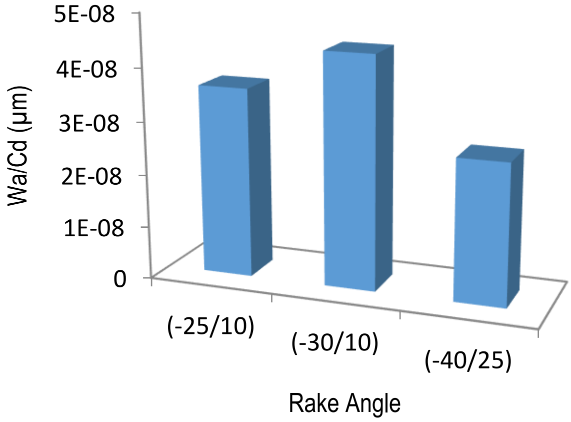

Figure 6-14: Tool wear resistance performance based on cutting distance

It was also noted that although observing the least frictional wear rate, diamond tool with -40° rake failed to maintain HPPT of silicon for longer cutting distance compared to -25° rake tool. This validates the importance of an optimal negative rake in machining brittle materials, where the worn tool can also machine in ductile regime using proper rake angle tool.

The effect of gradual tool wear can also be evaluated in the form of increased surface roughness of the machined surface. Fig. 6-15 presents the surface roughness variation with respect to cutting distance. With the increasing cutting distance, the tool edge deteriorates and affects the machined surface. It can be noticed from the cutting force plot that major wear for all rake tools transpired before 20km of cutting distance and then gradual frictional wear persisted for the remaining cutting distance.

It is also interesting to note that at similar tool wear area, the DBT point changes as a function of rake angle. Due to the tool wear, insufficient hydrostatic stress level along with stress disproportionality under the cutting edge result in DBT of the material. Unlike -30° and -40° rake tools, -25° rake angle tool was found to generate required hydrostatic pressure for HPPT of silicon even in worn conditions.

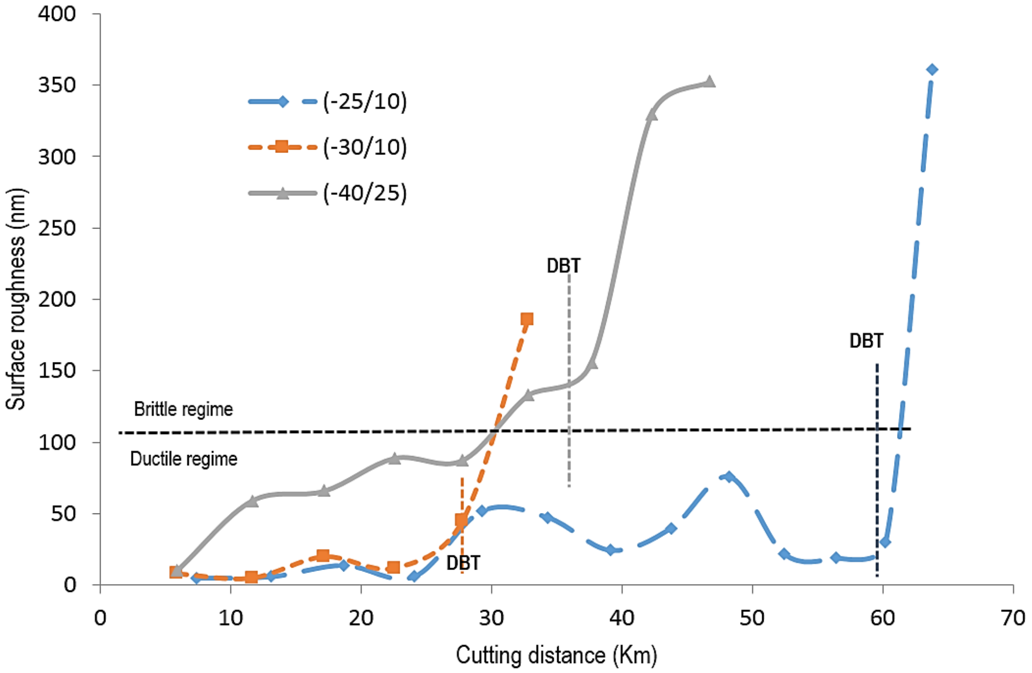

Figure 6-15: Surface roughness trend with respect to cutting distance

6.5 Summary

In this chapter, the investigation study of the effect of tool rake angles in SPDT of silicon was presented using experimental and simulation methods. The performance of diamond tools was analysed based on cutting forces, chip formation, surface roughness and tool wear studies. The study demonstrates that mechanism of plastic deformation in SPDT of silicon reliant on pressure induced continuous material removal using negative rake angle tools. The material removal using positive rake tools procured in the form of cracks rather than continuous chip removal and final machined surface quality is dependent on crack direction. Surface roughness deteriorates with the increase of tool wear. However ductile mode machining can still be achieved with the worn tool provided the required hydrostatic pressure is maintained for HPPT of silicon during machining and this performance was found highly dependent on rake angles. Diamond tool with -25° rake angle maintained the longest ductile mode machining even undergoing higher frictional wear rate than -40° rake tool. It was also found that any increase of negative rake beyond -25° rake angle result into the indeterministic machining. Also, the effect of rapid or progressive wear of diamond tool on HPPT of silicon varies for different rake angle tools. The tool with -30° rake angle was found to undergo the highest frictional resistance while cutting (111) silicon wafer and observed the shortest cutting distance than the other two tools. The relatively high tangential forces in experiments and reduction in shear plane length and lower von Mises stress in SPH simulation corroborate well for this behaviour. No direct correlation can be formed for tool performance with increasing or decreasing rake angle.

Chapter 7: Influence of tool wear on ductile to brittle transition

7.1 Introduction

This chapter presents the study of tool wear and its influence on ductile to brittle transition of silicon in SPDT. Based on critical chip thickness criteria by Black and Scattergood and other studies of diamond turning [9, 57, 70, 350, 352], when right tool geometry and cutting parameters are used, diamond turning of silicon can be achieved in ductile mode. Regardless of choosing right tool geometry and machining conditions, diamond tool wear still remains an ultimate criterion that governs plastic deformation or brittle fracture [42, 43]. In SPDT of silicon, the wear of diamond tool facilitates brittle fracture which in turn offers high cutting resistance to diamond tool promoting further tool wear. In order to prolong the ductile mode machining, it is crucial to understand the material removal mechanism during the DBT period as a function of progressive tool wear.

The progressive and final tool wear pattern and mechanism, as well as its influence on the plastic deformation and brittle fracture of silicon during plunging cut, are analysed in this chapter. In addition, a numerical simulation study using Smoothed particle hydrodynamics (SPH) approach is performed to investigate the influence of progressive tool wear on the machining mode and distribution of stresses on the machined surface along the cutting edge of the diamond tool.

7.2 Experimental study

Diamond turning experiments were carried out on an ultraprecision diamond turning machine (Moore Nanotech 250UPL) which possesses an air bearing work spindle and hydrostatic motional slides. Single crystal diamond tools with dodecahedral orientation were used in the experiment. A number of facing cuts were performed on the (111) surface of single crystal silicon until the onset of brittle fracture on the machined surface. Each facing cut covered an average cutting distance of 5 km. Before the first facing cut the diamond tool was plunged into the silicon surface at a distance of 6 mm to its centre to record the tool profile of the new diamond tool. Plunging cuts were performed after each iteration of facing cut to obtain progressive tool wear contour. Fig. 7-1 presents machining scheme of the facing and plunging cuts adopted in this study. Details of workpiece, tool geometry and machining conditions are presented in Table 7-1.

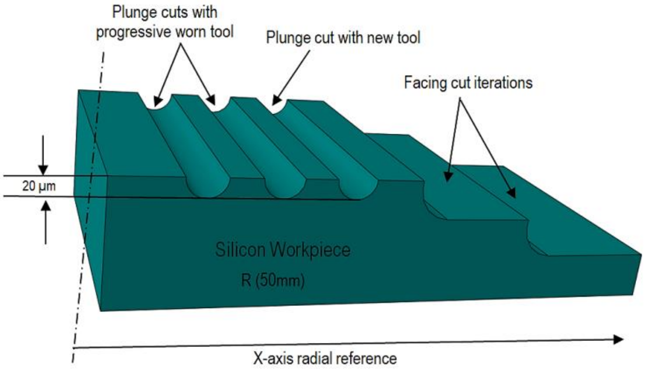

Figure 7-1: Experimental SPDT plan details

The cutting forces during facing and plunging cuts were measured by a Kistler dynamometer (9256C2). The machined silicon surface and plunge cuts were analysed using a 2D surface profiler (Taylor Hobson PGI 1240), a white light interferometer (Zygo Newview 5000) and an SEM (FEI Quanta 3D FEG) to study the material removal mechanics of silicon and diamond tool wear.

Table 7-2: Plunging cut experimental data and conditions

Silicon wafer	Diamond tools	Cutting parameters
Optical grade silicon, polished Round Orientation = <111> +/-5° Diameter = 100 mm Thickness = 5 mm Sample purity = 99.999%	Orientation = dodecahedral Rake angle = -25° Clearance angle: 10° Nose radius = 5 mm	Spindle speed =1200 rpm Cross-feed = 1 µm/rev In-feed = 0.1µm/rev Depth of facing cut = 10 µm Depth of plunge cut = 20 µm Coolant = water mist

7.3 SPH machining model

In experimental study, the localized chip formation and stress distribution in the chip formation zone and any change with the progressive tool wear cannot be truly determined. A numerical study using SPH approach was performed to address these experimental limitations.

A three-dimensional SPH diamond turning process model was developed by using general-purpose finite element software Abaqus. In order to study the influence of groove wear on material removal mechanism of silicon, plunging cuts were performed using new as well as worn diamond tools with groove flank wear. A similar groove tool wear contour observed in machining experiment by SEM was modelled with two different lengths of flank wear. Fig. 7-2 illustrates the new and worn diamond tools models adopted in SPH simulation study of silicon.

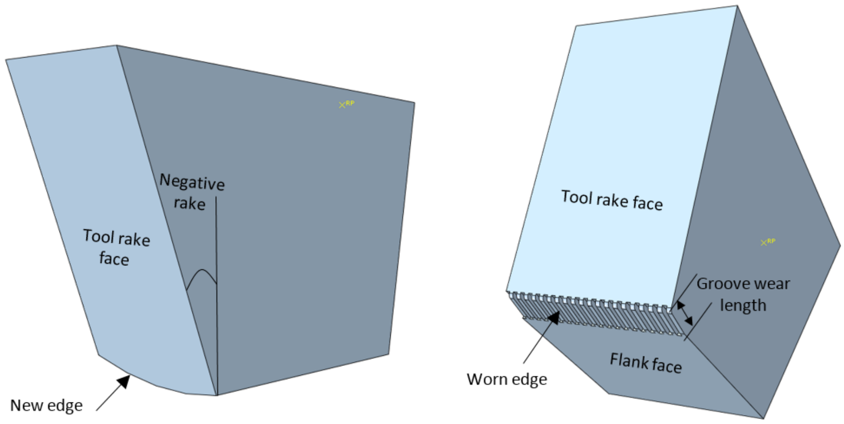

Figure 7-2: Diamond tool models in SPH study: new tool (left) and worn tool (right)

The SPH machining model of silicon with geometry and boundary conditions are presented in Fig. 7-3. The diamond tool was considered as a rigid body and modelled with Lagrangian mesh. The motion of the tool was constrained in the Y and Z directions. The velocity was assigned to the tool in the negative-x direction to obtain chip formation. The silicon workpiece was modelled as a deformable part consisting of SPH particles.

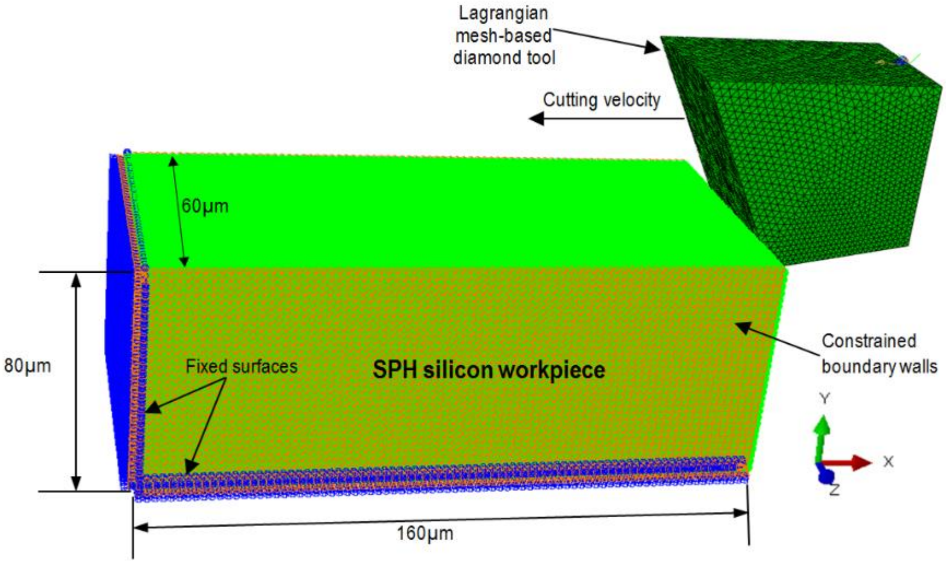

Figure 7-3: SPH machining model of SPDT process

The bottom surface nodes of silicon workpiece were fixed with encastre conditions to restrict the motion of the workpiece in all directions. The walls of the workpiece were constrained in the z-direction to achieve required material stiffness during chip formation.

Since all SPH particles in contact with the cutting tool are influenced by their neighbouring particles, it is crucial to define the nodal coordinates of these particles uniformly distributed in all directions. The sweep technique with medial axis mesh algorithm and minimized mesh transition features was adopted to produce the uniform mesh. The SPH particle density was selected based on convergence test study. The cutting parameters, tool and workpiece geometry adopted in the simulation study are detailed in Table 7-2.

Table 7-3: Cutting parameters used in SPH simulation

	Flank wear length (µm)	Rake/clearance angle	Workpiece dimensions (µm)	Cutting speed (m/s)	Depth of cut (µm)	SPH particles
Tool 1	0	-25°/10°	160x80x60	6.3	10	192580
Tool 2	4					
Tool 3	7					

Drucker Prager (DP) model [359] was adopted as a material constitutive model to predict the deformation behaviour of silicon during SPH simulation. Table 7-3 lists the material and contact properties adopted in SPH simulation study.

Table 7-4: Material and contact properties of silicon during SPH simulation

Density, ρ	2330 kg/m^3
Elastic modulus, E	146 GPa
Poisson’s ratio	0.2
Friction coefficient	0.05
Friction angle (β)	26°
Dilation angle (Ψ)	20°
Flow stress ratio, k	0.82

7.4 Results and Discussion

7.4.1 Measurement of tool wear in machining trials

Different dominant tool wear mechanisms have been reported in previous studies on diamond turning of silicon. These wear mechanisms include thermo-chemical wear [360], abrasive wear due to formation of dynamic hard particles or diamond-like carbon particles [85, 356, 357, 361], and abrasive wear due to the formation of silicon carbide (SiC) [355, 356]. The formation of hard particles has been attributed to phase transformation of silicon from monocrystalline to amorphous phase consisting of group of atoms with shorter bond length. While, the formation of SiC or diamond-like carbon particles caused by diffusion of carbons of diamond tools into silicon at high temperature and high hydrostatic pressure [356].

The new diamond tool was examined using the SEM for any existing damage on the cutting edge and on the rake and flank faces of the tool prior to machining. Fig. 7-4(a) shows SEM image of the new diamond tool which indicate a very sharp cutting edge between the rake face and flank face. In SPDT of silicon, diamond tools get worn even after machining a short cutting distance. This can be observed in Fig. 7-4(b) which shows thin groove marks appeared on the flank face of diamond tool after cutting distance of 5 km. The groove wear depth further increases with increasing cutting distance. The maximum flank wear of 7 µm was observed on the main cutting edge side reducing towards the apex of the tool and further to the trailing edge.

In cross-feed motion, when the tool approaches silicon workpiece, the main cutting edge comes in contact with the workpiece surface followed by the apex of the tool and subsequently trailing edge. The maximum stresses develop at the main cutting edge due to cutting maximum chip thickness which reduces towards the apex of the tool [9]. Hence high flank wear occurs towards the main cutting edge compared to apex and trailing edge. Abrasive wear mechanism was found dominant in the form of frictional groove wear as shown in Fig. 7-4(c) and 7-4(d).

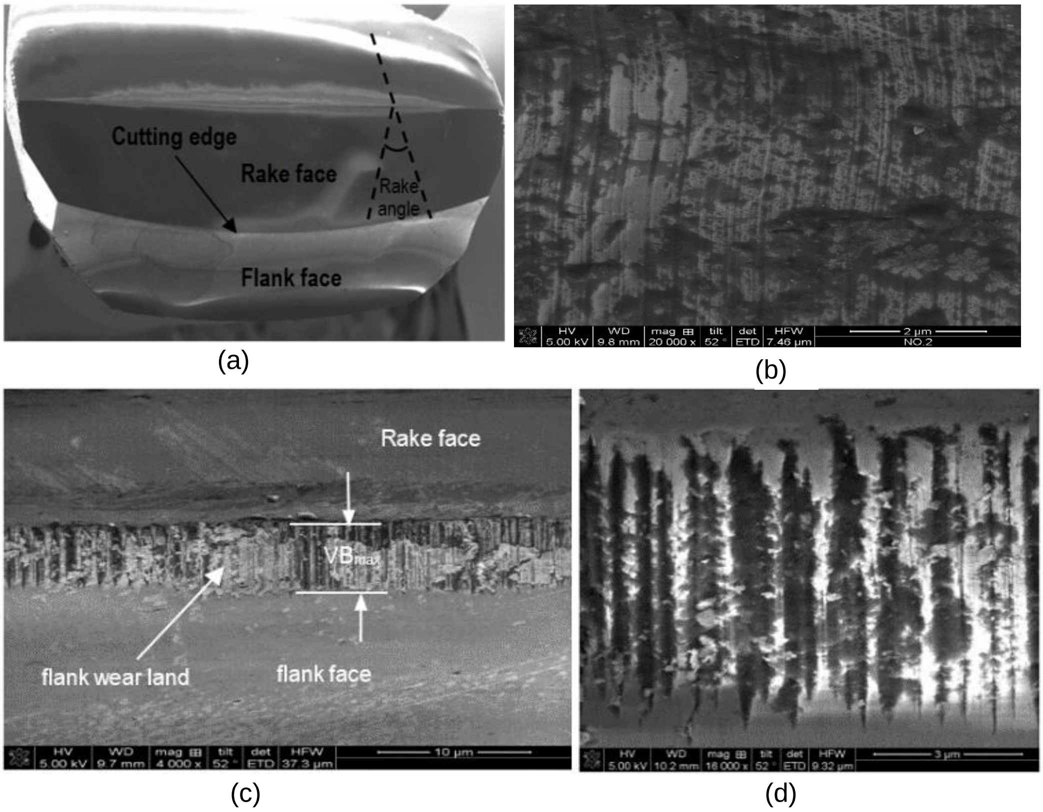

(a) (b)

(c) (d)

Figure 7-4: SEM images of diamond tool (a) new tool (b) flank wear (after cutting distance of 5 km) (c) Final tool wear when brittle fracture appeared on silicon surface (d) zoomed image of (c) shows groove and abrasive wear mechanism

Fig. 7-5 shows the schematic illustration of the degradation of tool radius and profile of the plunging cut of the diamond tool after 5km of cutting distance.

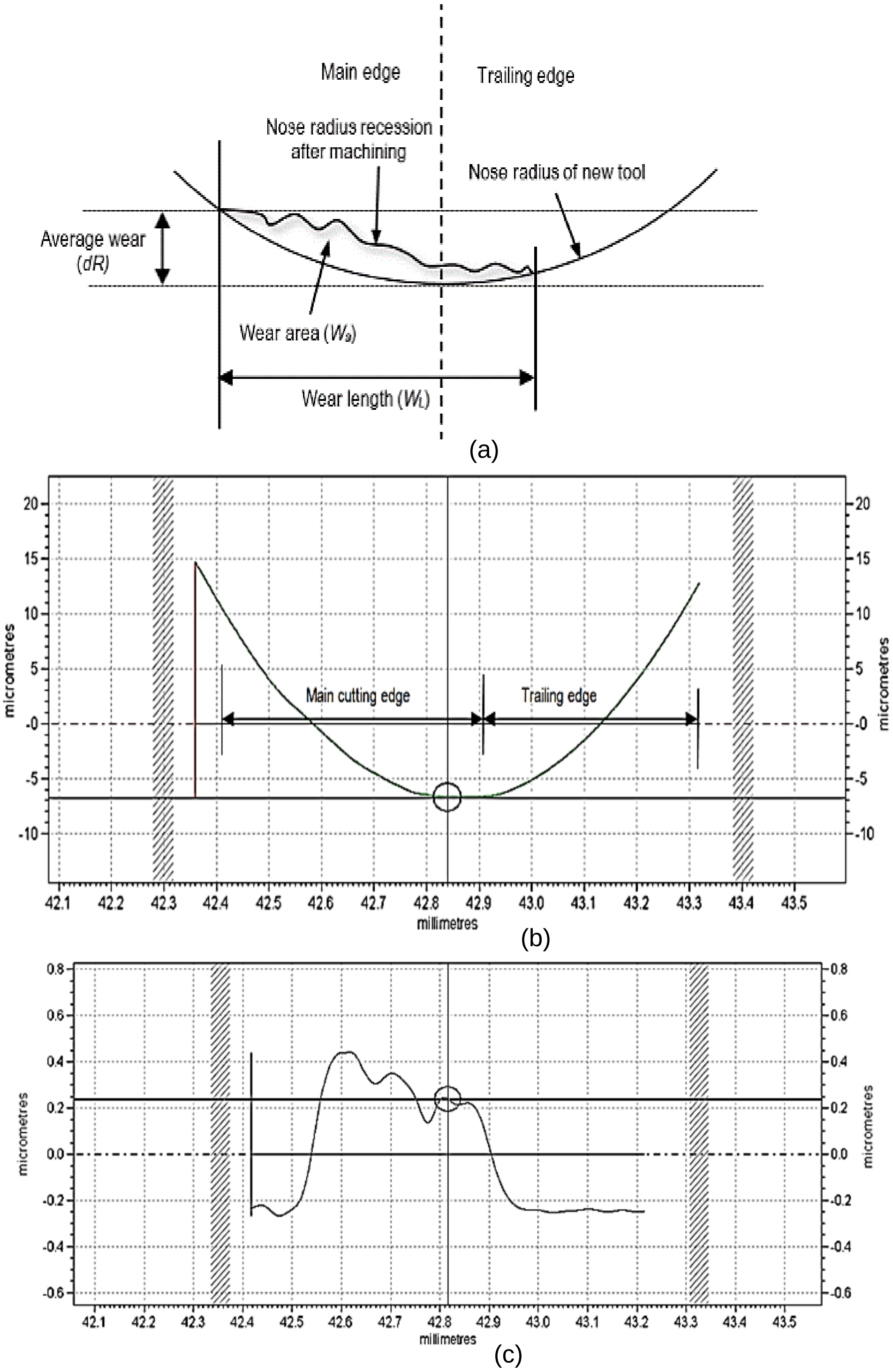

Figure 7-5: Estimation of tool wear (a) schematic illustration of the tool edge recession (b) Plunge profile of worn tool after 5km (c) Zoomed-in image showing worn area of the main cutting edge

The Least Square (LS) arc analysis [352] of the plunge profile by the worn diamond tool was performed to obtain the tool edge recession. Basically the analysis regards the plunge profile by the trailing edge as a datum (due to less wear on that side) and to LS fit it with the main cutting edge profile to obtain the whole wear area as shown in Fig. 7-6.

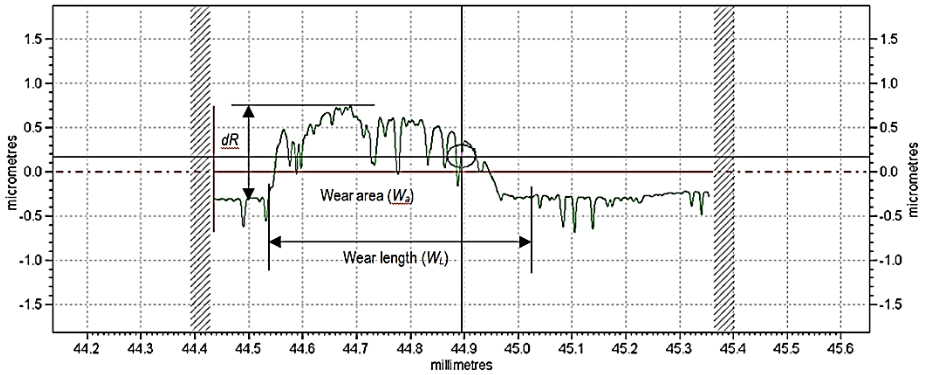

(After 15km)

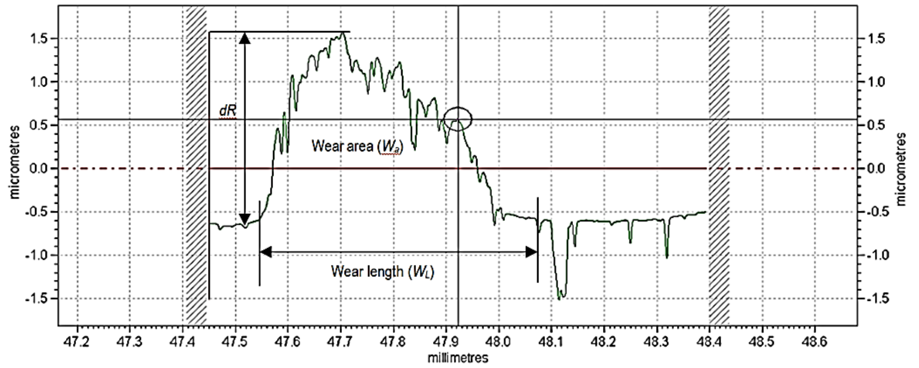

(After 30km)

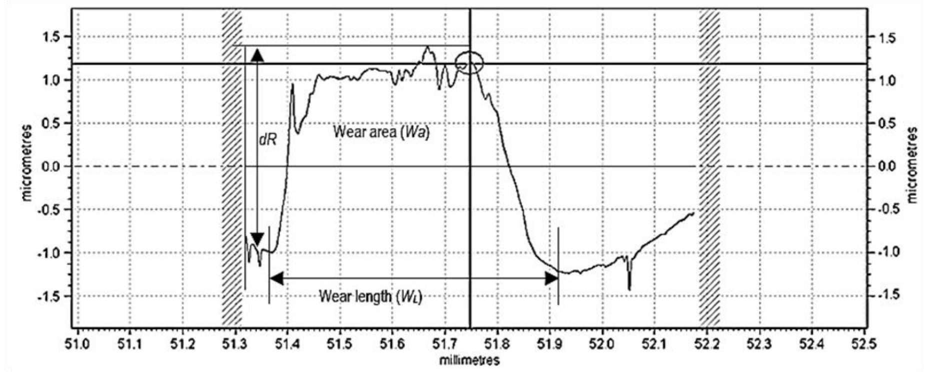

(After 40 km)

Figure 7-6: LS arc analysis to measure the edge recession of diamond tool

The wear area was calculated using the following relation:

$$w_a = (P_a \times P_{Lo}) - (P_{aN} \times P_{LoN}) \qquad (7.1)$$

Where P_a is the average height and P_{Lo} is the profile length of the modified profile in LS arc analysis method. They represent the average recession of round edge of the tool and increase in contact width respectively. The parameters P_{aN} and P_{LoN} are the average height and length of the new tool edge profile. The approximate recession of the rake face (w_{aR}) of the tool with the rake angle (α) can then be calculated by using following equation:

$$w_{aR} = \frac{w_a}{cos\alpha} \qquad (7.2)$$

Fig. 7-6 shows the result of LS arc analysis [352] of tool plunge profiles, i.e. the recession of tool along the cutting edge on the rake face after cutting distances of 15, 30 and 40 km respectively. A significant increase in the average tool recession can be observed from cutting distances from 15 km to 40 km.

Fig. 7-7 shows the progression of tool wear area with the increasing cutting distance and the variation of average cutting forces during face turning and the maximum thrust force during plunging cuts. With the increase of the cutting distance, tool wear area as well as the magnitude of cutting forces increases. A sharp increase of the tool wear rate was found during initial cuts (between cutting distances of 5 km and10 km). Tool wear rate showed steady behaviour during middle phase (cutting distances from 10 km to 25 km), and endured severe tool edge degradation after cutting distance of 30 km until the onset of brittle fracture. The higher tool wear rate during the initial cuts attributed to a general trend of quick edge recession of sharp cutting edges. The tool maintains its strength and tool edge degrade with the lower wear rate during the middle phase. With the increase in brittle fracture of silicon, the frictional resistance increases, and the tool undergoes severe abrasive wear in the final phase. A good correlation of the tool wear area and cutting forces can be observed in Fig. 7-7.

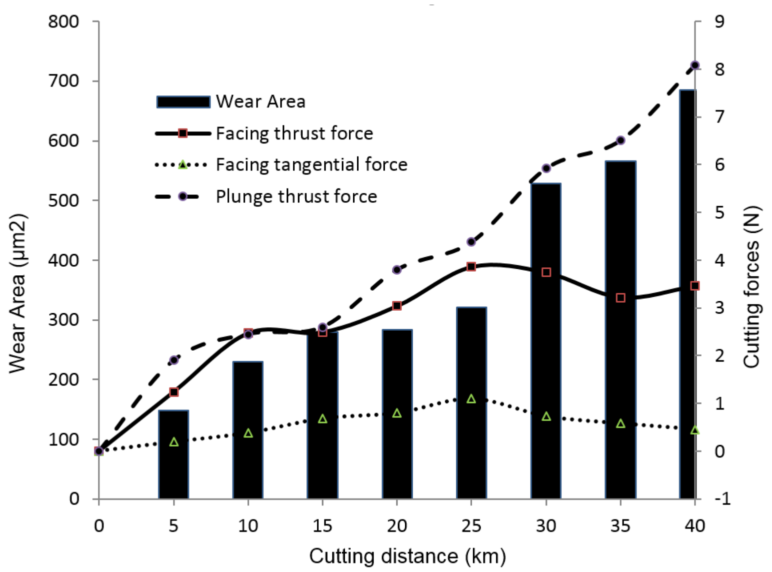

Figure 7-7: Progression of tool wear area and cutting forces with increasing cutting distance

The contact pressure between the tool and the workpiece drops with the tool edge recession since the input depth of cut (z-axis travel) for all plunge cuts remains the same. However, frictional resistance between the tool and the workpiece increases with the dullness of the diamond tool and hence increase of cutting forces. The reduction in tangential and thrust forces in the final phase of facing cut attributed to the superimposition of effect of contact pressure reduction over frictional resistance with further edge degradation. In plunging cut, due to full tool edge contact, the frictional resistance superimposes the effect of contact pressure reduction and hence the cutting forces continuously increase until the onset of brittle fracture on the silicon surface.

7.4.2 Ductile to brittle transition

The machined surfaces of silicon obtained by plunging cut were observed by SEM in this study. The transition of machining mode from ductile to brittle fracture can be observed with the formulation of lateral cracks along with the ploughing marks leading to brittle removal of material. Series of lateral cracks appeared across the tool path in the initial stage of tool wear at 15 km as shown in Fig. 7-8(a). They propagated deep into the surface at 25 km (Fig. 7-8(b)) with further wear and ensued into severe brittle damage at 35 km as shown in Fig. 7-8(c). The initiation of lateral cracks can be attributed to the local uneven stress distribution along the tool path due to unloading and tool wear. When the tool cutting edge is sharp, it remains in contact with the machined surface; and due to high cutting speed, unloading phenomenon doesn’t transpire completely. However, when the tool edge degrades, the irregular unloading occurs across and parallel to the tool path dependent on the wear contour. The local tensile stress develops behind the tool cutting edge during unloading in contrast to compressive stress in front of the cutting edge. When the stress difference is small, lateral cracks appear but brittle damage doesn’t occur completely as was observed in Fig. 7-8(a). With the increase of difference in pressure (at surfaces *a* & *b* in Fig. 7-8(b)), the surfaces (*a & b*) overlaps. Material removal through brittle fracture occurs in the next stage 3 (Fig. 7-8(c)) with further pressure difference due to high tool wear.

It is important to note that these lateral cracks and fracture were more severe in the middle and main cutting edge side. The analysis of brittle fracture in the plunging cut area suggests that mild ploughing occurs with frictional tool edge degradation, promoting lateral cracks to initiate first followed by the median cracks.

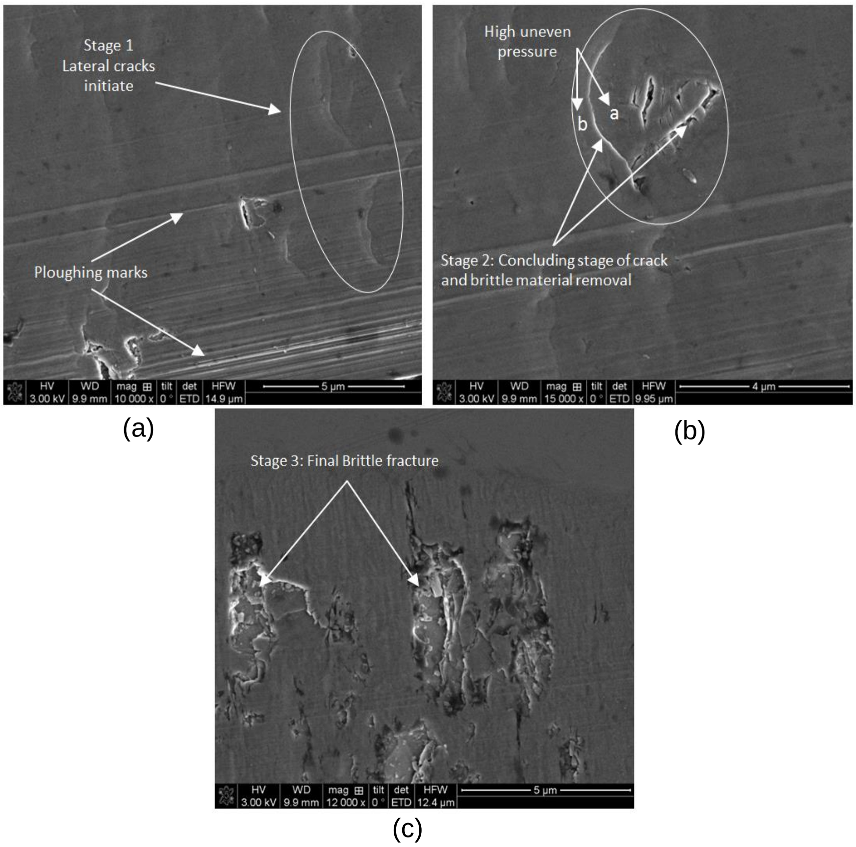

Figure 7-8: Surface damage and lateral cracks from (a) crack initiation stage (b) crack concluding stage (c) brittle material removal

The material removal along the edges was also found to occur due to the lateral crack turned into the chipping damage propagating into the optical smooth machined surface area as shown in Fig. 7-9.

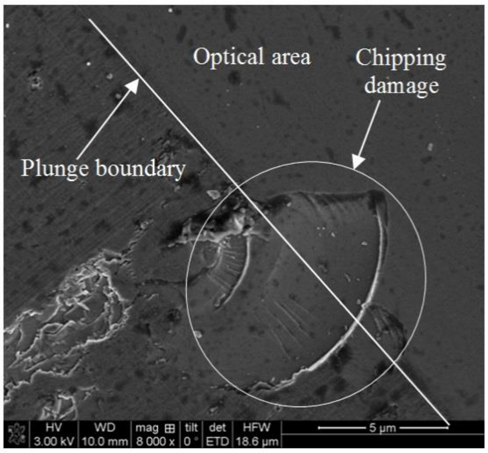

Figure 7-9: chipping along plunge boundary propagating into optical area

7.4.3 Plunge surface measurement

The machined surfaces topography obtained by plunging cuts were also analysed by using white light interferometry. The plunge profile geometry as well as surface topograhpy in the final plunging cut can be observed in Fig. 7-10. The depth, as well as the width of the plunge cut, was found to reduce due to increasing tool wear.

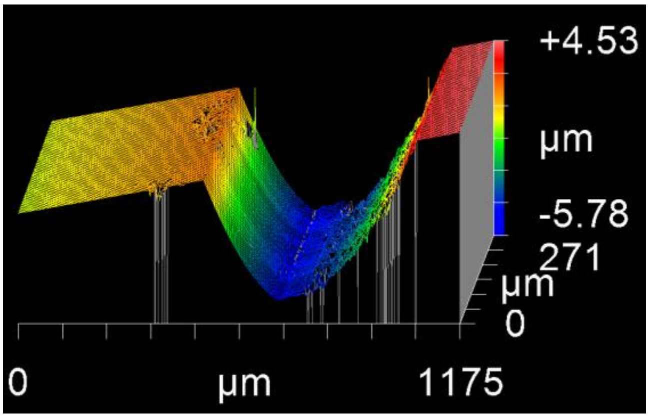

Figure 7-10: Plunge cut surface with final brittle fracture

The brittle fracture damage on the plunge surfaces was found to increase with the progressive tool wear, so did the surface roughness (R_a). Fig. 7-

11 presents the variation in plunge width as well as surface roughness with the increasing tool wear area. The maximum reduction in width was observed during phase 1. During phase 2, the plunge width remains stable with slight variation, and then sharply reduced in the final phase until the onset of brittle fracture.

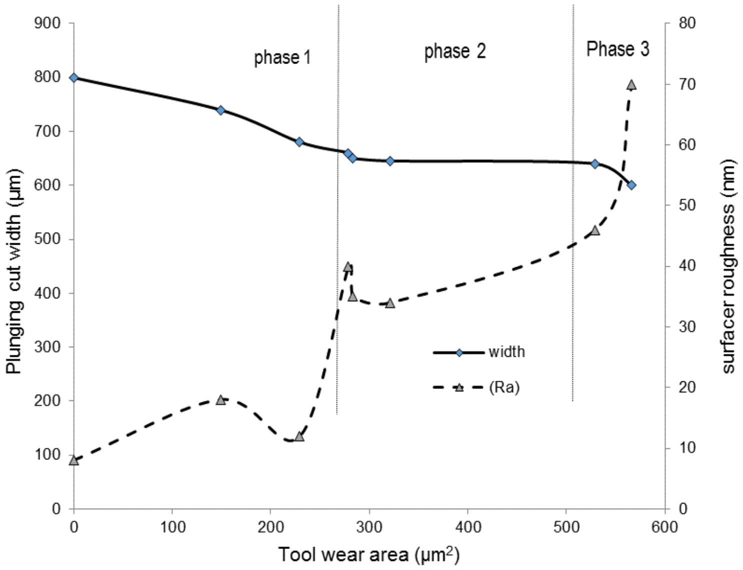

Figure 7-11: Variation of plunge width and surface roughness with progressive tool wear

The surface topography of the initial and final plunge cuts was presented in Fig. 7-12. During facing cuts, the maximum tool wear occurs at the main cutting edge of the tool. When plunging cuts are performed with a worn tool, the tool cutting edge governs the machining mechanism developed during the plunging cut. Due to main cutting edge wear during face turning, the material removal in the plunging cut was achieved by brittle fracture on the main cutting edge side. A better surface roughness profile can be observed on the trailing edge side in the plunging cut profile. The reduction in tool-workpiece contact width was also recorded from 800 µm to 580 µm in the initial and final plunge cuts respectively.

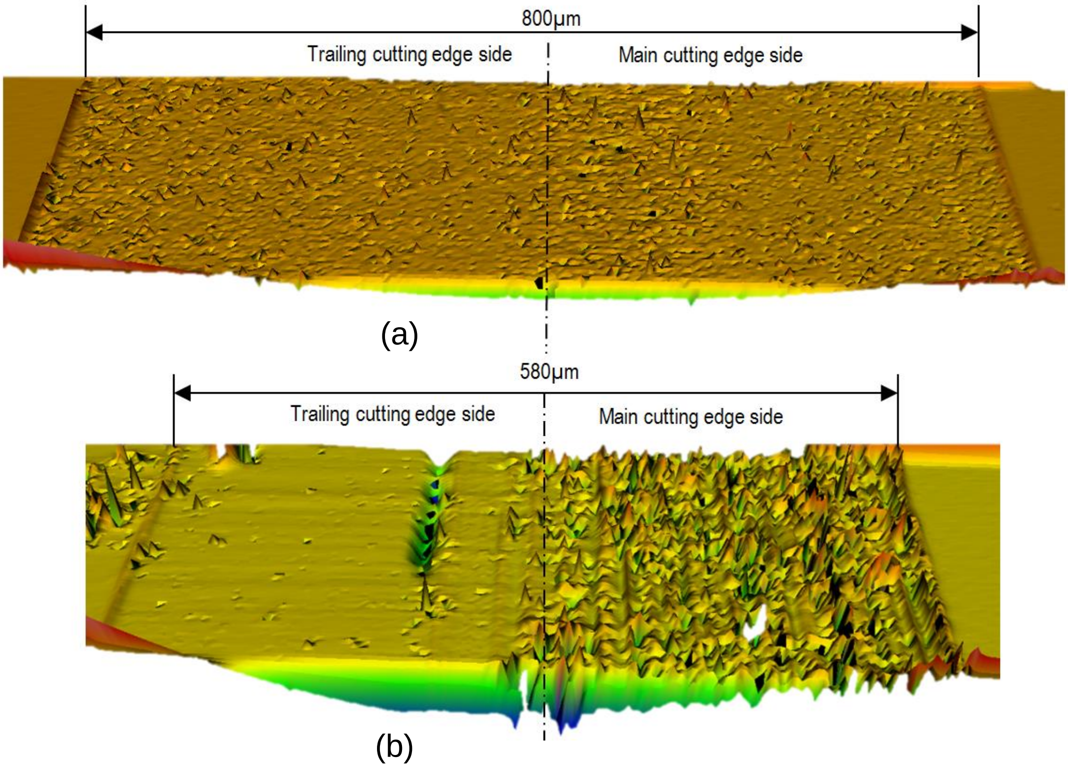

(a)

(b)

Figure 7-12: Surface topography of (a) initial plunge cut and (b) final plunge cut

7.4.4 Flank wear effect in SPH study

Cutting forces were calculated during simulations for the new and worn diamond tools. The SPH model was validated with experimental cutting forces. The normal cutting forces comparison of the new and worn diamond tools is presented in Fig. 7-13. Higher normal forces were observed for the worn tools compared to the new diamond tool indicating an increase in cutting resistance with tool wear. Although cutting forces during incipient stage of chip formation were found almost similar for both tools 2 and 3, for a significant period of cutting time, normal forces observed for tool 2 with smaller flank wear were higher than tool 3 with higher flank wear. This behaviour can be attributed to a reduction in cutting energy due to reduced cutting depth with higher flank wear.

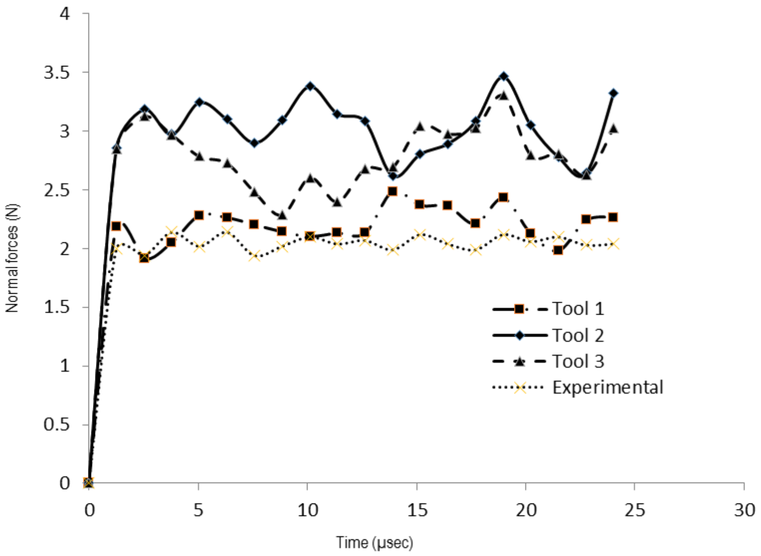

Figure 7-13: Cutting forces comparison for the new and worn tools in SPH study

Fig. 7-14 presents the von Mises stress distribution for the new and worn diamond tools. Von Mises stresses were observed significantly higher for the tool with lower flank wear width than the new as well as the tool with higher flank wear. For the new tool, the highest values of stresses were observed right underneath and in front of the cutting edge of the tool. However, when the tool is worn with the flank wear, the highest values of stresses were also observed right behind the worn edge of the tool. This behaviour exhibits a significant increase of frictional resistance to shear deformation due to rubbing of the flank worn area with the workpiece surface. For the worn tools, the offset distance of maximum values of stress from the main cutting edge is shown in Fig. 7-14. The displacements of maximum von Mises stress from the main cutting edge were measured as 4.6µm and 7.4µm for the tools with lower and higher flank wear width respectively. The maximum von Mises stress behind the worn edge towards the machined surface surely contributes to the deterioration of machined surface as was observed in the experimental study.

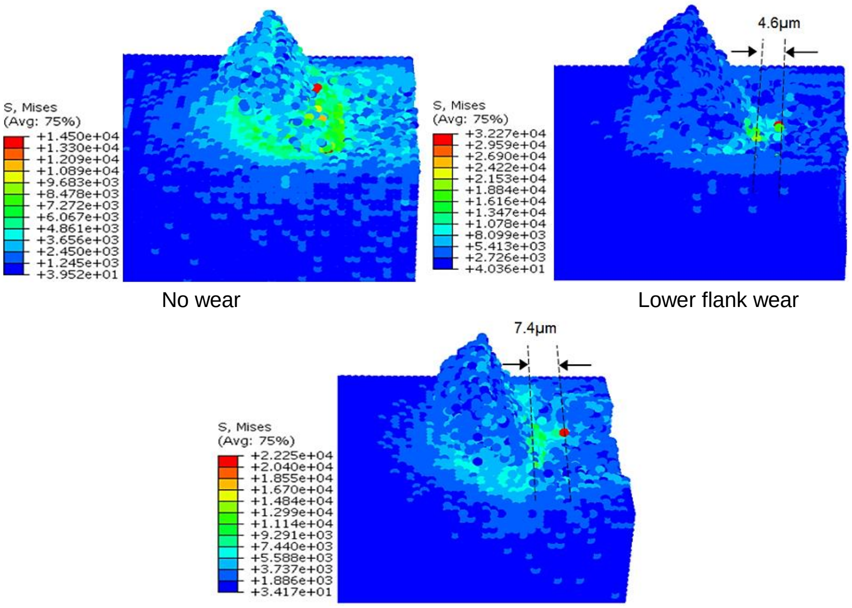

No wear

Lower flank wear

Higher flank wear

Figure 7-14: Von Mises stress (MPa) distribution for different tool wear conditions

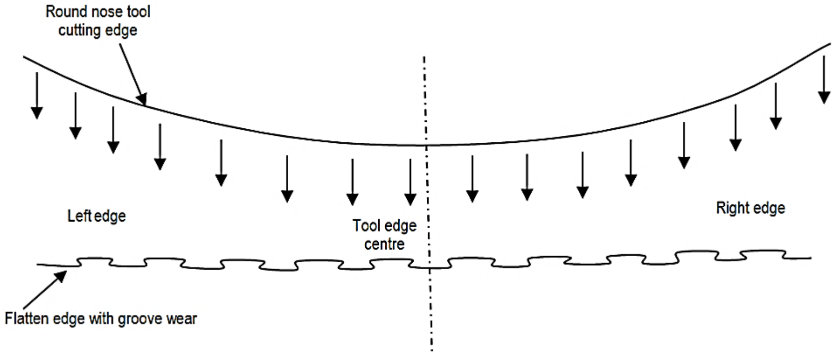

Figure 7-15: Schematic of tool edge variation from round to flat edge due to wear (arrows indicating hydrostatic pressure distribution)

With the tool wear, the shape of the cutting edge of the tool changes as shown in Fig. 7-15. The hydrostatic stress distribution on the machined surface along the cutting edge also varies with the change of tool-edge contour.

Due to practical limitations in high-speed machining environment, it is difficult to identify the magnitude of global as well as localized hydrostatic pressure during cutting. During the simulations, the maximum hydrostatic pressure of 18GPa, 32GPa and 36GPa was found in the plunge cut area for the tool 1, 2 and tool 3 respectively. The hydrostatic stress distribution in the plunge cut plane along the tool edge is presented in Fig. 7-16.

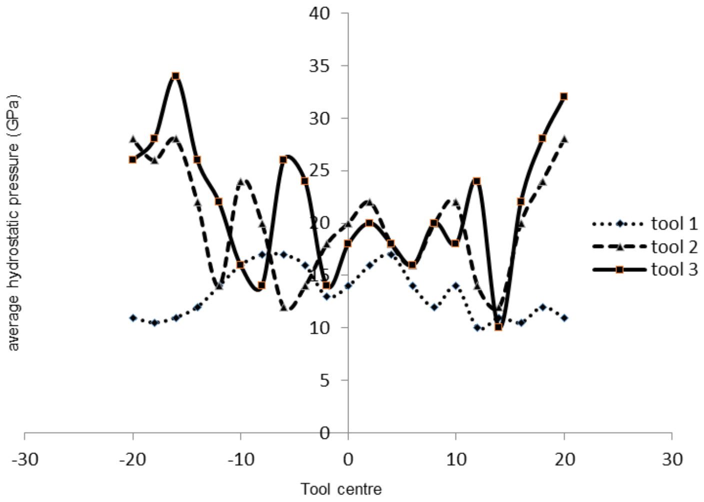

Figure 7-16: Hydrostatic stress distribution along the cutting edge

For the tool 1, the average hydrostatic pressure was found higher near the tool edge centre and reduced gradually towards the corners of the tool edge. However, for both tools 2 and 3, the average hydrostatic pressure was found increasing from the tool centre towards the corners of the tool edge on both sides. It was also noted that hydrostatic pressure between any two nearest positions fluctuate significantly for both tools 2 and 3, compared to the tool 1 for which the difference is much smaller. This high pressure difference leads to lateral crack generation and results in onset of brittle fracture as observed in the experimental study by the SEM.

7.5 Summary

Experimental and SPH based numerical simulation study were performed to investigate the influence of progressive diamond tool wear on material removal mechanics of silicon in SPDT. The correlative analyses of the tool wear profile and machined surface profile were performed. The transition of machining mode from ductile to brittle initiate with the formation of lateral crack at lower tool wear. It transforms into severe brittle damage with further increase of tool wear. For the sharp cutting edge, the location of maximum failure stress obtained in front of the main cutting edge. With the increasing flank wear length, the location of maximum failure stress displaces towards the machined surface behind the tool cutting edge results in the deterioration of the machined surfaces. The hydrostatic stress distribution underneath the tool cutting edge significantly varies with the change of cutting edge contour. The high fluctuation of hydrostatic stress between the two nearest points due to groove wear facilitates onset of brittle fracture on the machined surface. Since no traces of SiC were detected during the EDX analysis, groove wear on diamond tool is therefore, caused by the formation of hard particles.

Chapter 8: Surface defect machining in single point diamond turning of silicon

8.1 Introduction

This chapter presents the feasibility study of potential application of recently developed surface defect machining (SDM) method in SPDT of silicon. The SDM involves the generation of surface defects on the workpiece surface at a depth less than the uncut chip thickness using sophisticated mechanical, thermal or any other suitable methods before the actual machining. The basic principle of SDM is to reduce the surface strength of the workpiece in the chip formation zone. In SDM, material removal results in weak interface layer on the top face which is of critical importance in stress degradation. Material defects leads to discontinuous and broken chips and result in reduced cutting temperature and lower tool wear [362]. The SDM method offer reduction in the shear strength, reduced residual stresses and reduced temperature which motivates better surface finish and reduced tool wear.

Numerical simulations were performed for the conventional and SDM process and results were compared for chip formation, resultant machining forces, stresses and hydrostatic pressure with and without SDM.

8.2 Generation of surface defects

The choice of surface defects generation method is based on low cost and time, damage control and its dependence on material machinability. Surface defects can be generated using laser as well as different type of patterning tools with different structures. Different structures induce different chip flow type and direction and offer varied resistance to cutting and therefore carry significant importance in the deformation mechanism. The damage can be introduced on the workpiece surface in the form of holes, multi-shaped grooves, channels and various other structures. Shape of these defects or structures may significantly contribute to reduction in cutting temperature, cutting resistance and machining energy and therefore various defects should be tested for comparison.

8.3 SPH simulation model of SPDT

SPH simulation model of conventional cutting was developed with negative rake angle tool. Fig. 8-1 represents the SPH model of cutting process of diamond turning. The cutting tool was modelled as rigid tool using C3D8R elements. The silicon workpiece was modelled as a deformable part with dimensions of 360x180x100 µm using PC3D elements to handle high deformation in cutting process.

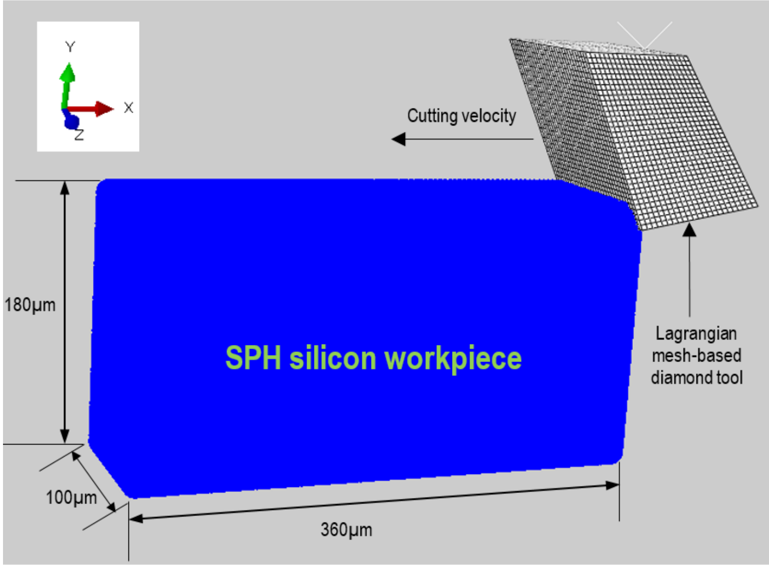

Figure 8-1: Conventional machining model of SPDT of silicon

A convergence study was carried out based on von Mises stress to determine the optimal particles density for obtaining accurate simulation results with computational efficiency. The SPH particle density was kept homogeneous throughout the workpiece part in order to avoid any undesirable stress concentration. The bottom surface of the workpiece was kept fixed in all directions to achieve required stiffness. The depth of cut was 10 µm, and cutting velocity of 6.3 m/sec was applied to the tool in the negative x-direction. Table 8-1 lists the elastic and plastic properties of the material. Elastic-brittle/perfectly plastic response behaviour of silicon was investigated using pressure-dependent DP yield criterion.

Table 8-1: Material properties of silicon used in SPH simulation

Density, ρ	2330 kg/m^3
Elastic modulus, E	146 Pa
Poisson’s ratio,	0.2
Friction angle (β)	26
Dilation angle(Ψ)	-20
Flow stress ratio, k	0.82

The material model parameters obtained through inversed analysis were used to simulate the cutting process. SPH can simulate the chip separation naturally without introducing any physical, geometrical separation criteria or damage model. The simulation model analyses the mechanical interaction between silicon work-piece and diamond tool. In cutting operation, the slip between different layers of atom results in chip formation and cutting is mainly subsidised due to the shearing action.

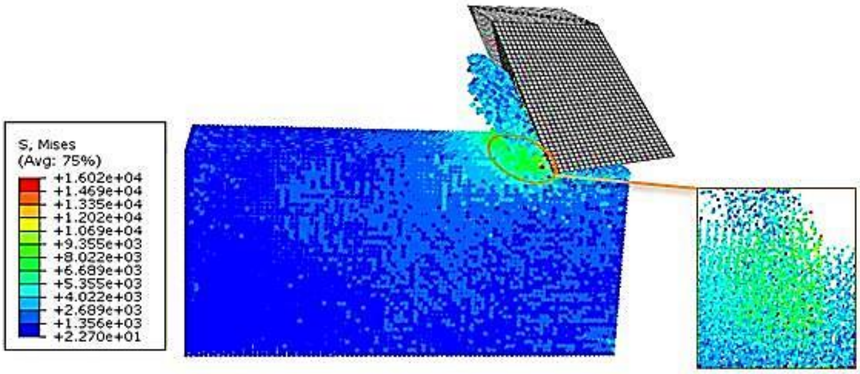

Figure 8-2: SPH cutting simulation of silicon with von mises stresses (MPa)

Fig. 8-2 illustrates chip formation of silicon at steady-state condition. The chip formation was observed with the combination of plastic deformation in the chip formation zone with minor brittle fracture on the free chip surface. The von-Mises stresses reaches beyond yield strength of silicon showing machining through plastic deformation.

8.4 Experimental validation of SPH model

In order to assess the validity of the developed SPH simulation model, diamond turning of single crystal silicon was performed and cutting forces results were compared with the simulation results. Silicon with crystal orientation (111) was machined using Precitech Nanoform 250 ultra-precision diamond turning machine.

Table 8-2: Experimental data: material specification and cutting parameters

Silicon	Crystal orientation Wafer Size	<111> Dia= 100mm, thickness = 5 mm
Diamond	Crystal orientation Rake angle Clearance angle Nose radius	Dodecahedral -25° 10° 5 mm
Cutting parameters	Speed Feed Depth of cut	1200 rpm 1µm/rev 10 µm

	coolant	Water mist

Single crystal diamond tool with round edge was used to machine silicon. Silicon is known to expedite high tool wear during machining ensuing shorter tool life and degradation of surface quality. Since the surface depreciation also attributed to pre-machining cracks and crack initiation in the primary shear zone and their propagation into the machined surface, the silicon wafer was carefully observed for any pre-machining defects and surface cracks.

Table 8-2 lists the specification of silicon wafer and diamond tool along with cutting parameters used in the machining experiments. Diamond tool was examined under SEM for any prior damage before diamond turning. Cutting forces developed during machining were monitored and recorded using three-component Kistler dynamometer 9256, charge amplifier and an advance data acquisition system with Dynoware.

8.5 Cutting forces comparison of experimental and SPH method

In order to avoid any inconsistency in machining and simulation model, the cutting velocity, depth of cut and rake and clearance angle are kept in the same values in both studies. In machining, cutting forces are significantly influenced by tool-chip interface friction parameters, material properties as well as tool geometry [363]. Classical Coulomb's friction model has been widely used in machining due to its simplicity and has significant effect in the magnitude of cutting forces. The friction coefficient between diamond and silicon in machining is always approximated and has not yet been identified [328]. In SPH, a tool-chip interface friction criterion is governed by the interaction of stressed particle and its effective neighbouring particles. SPH, therefore, offers internal friction criteria of the particles between the tools and the workpiece when both are modelled with SPH particles, and therefore, no Coulomb's friction coefficient is required. However, Abaqus does not allow the interaction of two different SPH particles parts; the tool was modelled with Lagrangian mesh-based approach. Penalty friction formulation with a friction coefficient of 0.2 was used in SPH machining model. Cutting forces were recorded for both experimental work and simulation model.

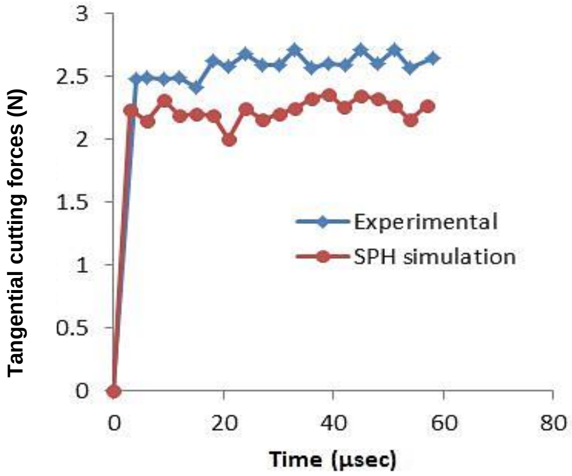

Figure 8-3: Tangential force comparison of experimental and simulation model

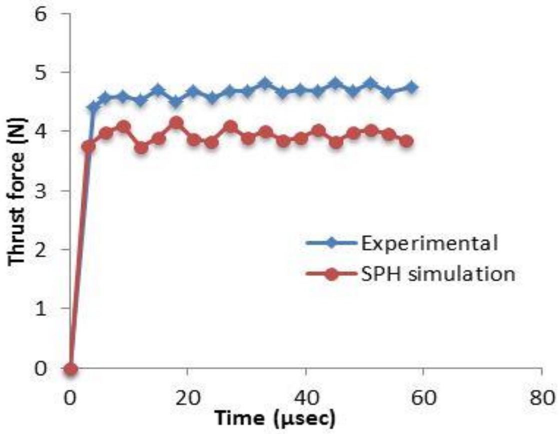

Figure 8-4: Thrust forces comparison of experimental and SPH simulation

Fig. 8-3 and 8-4 show the comparison of tangential and thrust forces, respectively, obtained through experimental and simulation studies. In both the experimental and simulation model, cutting forces increase sharply as tool makes contact with the workpiece. After the initial chip formation stage, the forces endure constant trend with slight variation indicating steady-state cutting. It can be seen that in experimental study, both tangential and thrust forces are slightly higher than the simulation model. The percentage difference in the average tangential and thrust forces obtained from experimental and SPH results was measured in equitable range of 12.8 and 13.2 % respectively. The differences between the simulated cutting forces with those obtained through cutting trials are due to ideal (no internal defects) diamond tool and silicon workpiece are assumed and machine stiffness effects were not considered in order to reduce the complexity of simulation model.

8.6 SPH simulation of SDM of silicon

A comparison study of SPH simulations of conventional and SDM machining of silicon were carried out and any transition in cutting forces, chip separation behaviour and stress distribution were investigated to evaluate the SDM approach. Surface defects of different types were introduced onto the workpiece top surface of validated SPH model.

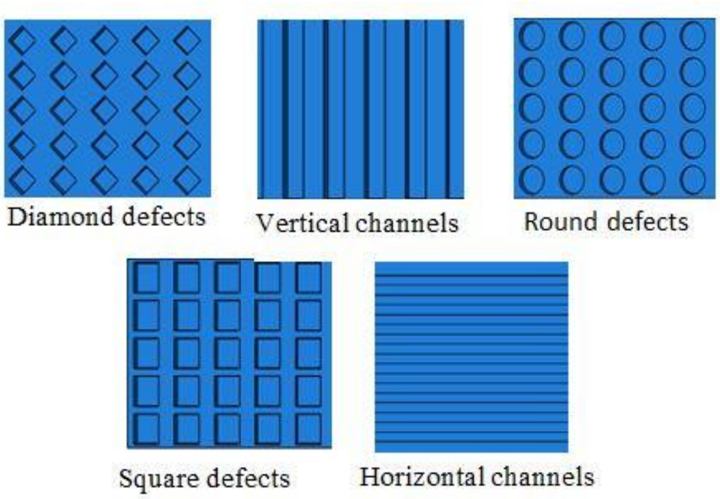
Diamond defects
Vertical channels
Round defects
Square defects
Horizontal channels

Figure 8-5: Surface defect patterns in SDM simulations

Both conventional and SDM machining simulations were carried out with similar cutting parameters and tool geometry. The particle density was maintained virtually homogeneous around the defects in order to avoid any artificial stress concentration as well as to maintain sufficient particle resolution around the defects.

Fig. 8-5 presents the different type of surface defects used to evaluate the surface defect machining of silicon. Surface defects were equally distributed on the top surface of workpiece with internal distance of 10µm. Table 5 lists the dimensions of defects exploited in SDM study along with model details.

Table 8-3: Specification of SPH conventional and SDM simulation models

Machining	Model dimensions (µm)	Width/ diameter (µm)	Defect depth (µm)	Depth of cut (µm)	SPH particles
Conventional	360x180x100	N/A			134877
Horizontal	360x180x100	15x360	8	10	134695
Vertical	360x180x100	15x100	8	10	136991
Diamond	360x180x100	15x15	8	10	140531
Square	360x180x100	15x15	8	10	147181
round	360x180x100	15	8	10	165123

8.7 Results and discussion

8.7.1 Chip formation

In the conventional metal cutting process, chip formation is due to the shearing action in which layer of front atoms slip over the subsequent layer of atoms [364]. In machining silicon, the chip formation is usually through a combination of plastic deformation and brittle fracture resulting in a mixture of continuous and discontinuous chips (dependent upon hydrostatic pressure). In diamond turning trial in this study, the depth of cut is controlled below brittle to ductile transition point. Silicon chips were therefore removed in ductile mode and good surface finish of 5nm was achieved. Fig. 8-6 shows continuous chips obtained during machining trials.

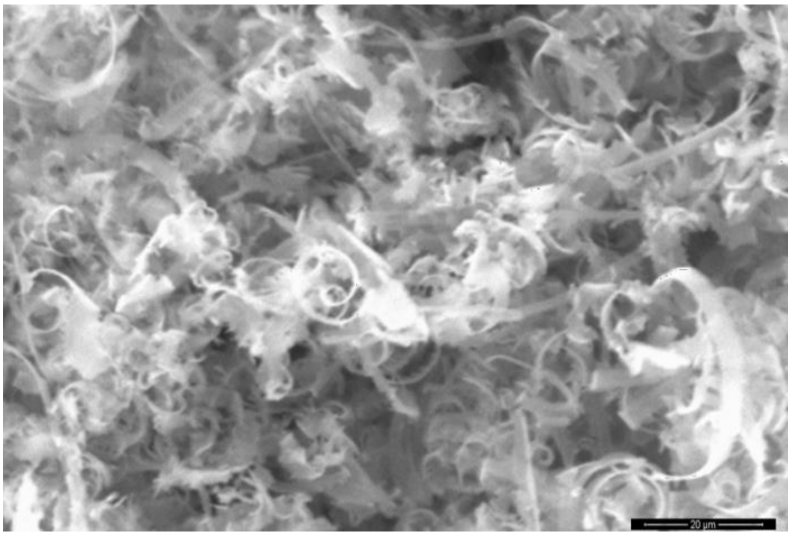

Figure 8-6: Continuous chips obtained in machining silicon

Fig. 8-7 shows the chip formation as well as the distribution of von Mises stress in conventional and SDM machining with different type of pre-formed defects. The maximum value of von Mises stress reached ~16 GPa in conventional machining whereas the stresses in SDM machining reduced for all the defects. The maximum reduction in von Mises stress was observed in vertical defects for which the highest value reached 14.6 Gpa. In conventional machining, when no defects are present, the atoms on the uncut chip layer intact with each other provide strength to the material. Due to this bonding strength, reaction to any induced stresses results in the resistance to deformation by the layer of atoms present in front of the tool cutting edge. The front atomic layer transfers the stress energy to the following unstressed layer of atoms and causes stresses to develop in the larger area in front of the tool as well as an increase in shear strength of material. This, therefore, results in brittle fracture in the weak zone due to anisotropic strength property of the material. Depending on the rake angle of the tool, this phenomenon transpires in the surface layer in front of the positive rake tool as well as front and under the surface in the negative rake angle tool.

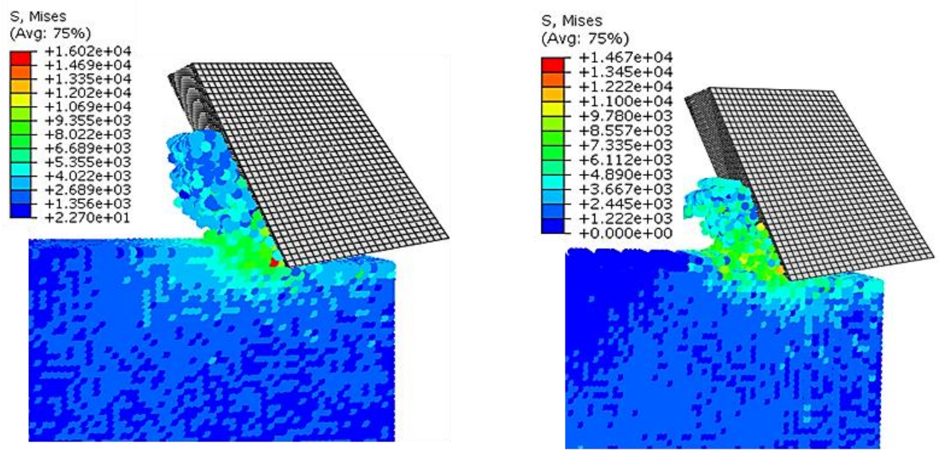

(No SDM)

(Vertical defects)

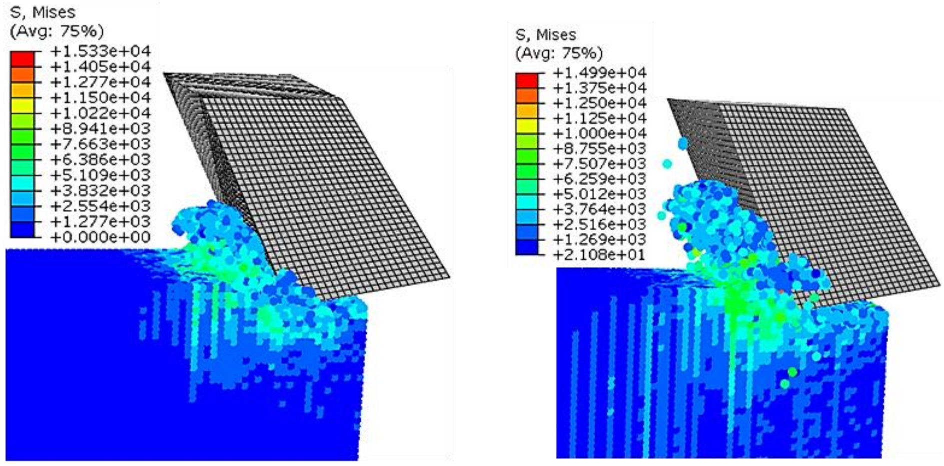

(Diamond defects)

(Square defects)

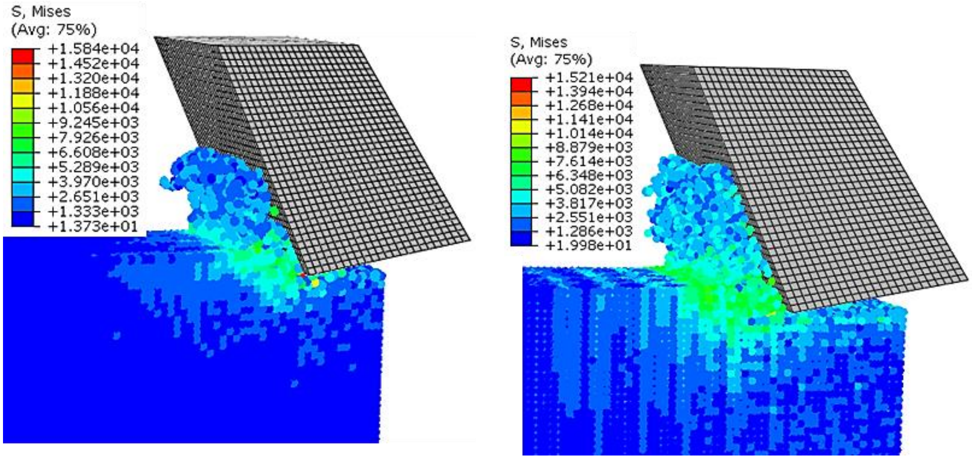

(Horizontal defects)

(Round defects)

Figure 8-7: Chip formation and von mises stress (MPa) in conventional and SDM machining

In SDM machining, this front atomic surface layer can only pass partial strain energy to the unstressed atoms due to the defects present between the layers results in chip formation with less cutting force and less influenced area. Depending on the defects type, stress distribution localises within chip formation zone which also facilitates chip reduction in the secondary deformation zone. In SDM machining, the material removal in front of the cutting edge remains continuous, whereas, on the free surface of the chip, it removes through brittle fracture. The disintegration of particles in SDM machining on the free surface side of the chip can be observed in Fig. 8-7 compared with conventional machining in which the particles of the chip are more compact and connected. This brittle failure on the free surface of the chip offers a reduction in cutting resistance. In conventional machining, where plastic deformation is dominant on both sides of the chip, silicon offers high resistance to plastic deformation and therefore requires high energy and result in higher cutting forces in plastic deformation than brittle fracture.

8.7.2 Primary shear zone

The schematic of conventional cutting with chip formation and illustration of primary and secondary shear zone is presented in Fig. 8-8. Shear stresses, strain rate and temperature are significantly influenced by the change in geometry of primary shear zone [365]. The geometry of the primary shear zone is governed by the shear plane angle ($\varnothing_s$) and the ratio of length of the primary shear zone (l_{AB}) to its thickness (t_p).

The shear strain prevails in primary shear zone area with maximum strain at plane AB. The strain AB is described in equation 8.1.

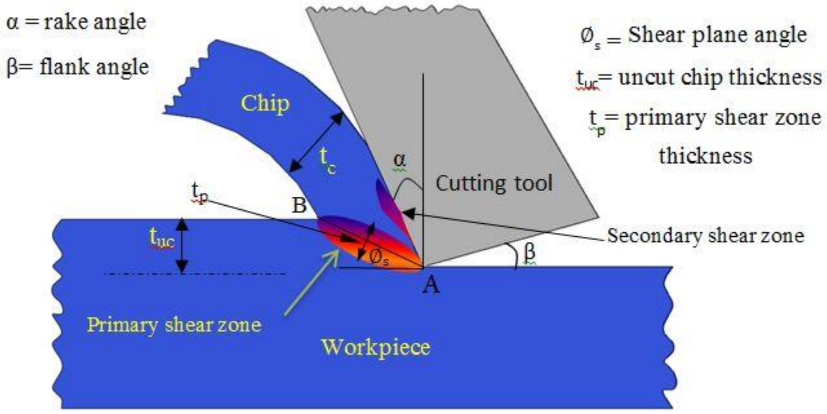

Figure 8-8: Schematic of chip formation conventional cutting

$$\varepsilon_{AB} = \frac{\cos\alpha}{2Sin\emptyset_s \cos(\emptyset_s - \alpha)} \qquad (8.1)$$

In equation (8.1), ε_{AB} is shear strain in the primary shear plane AB. The angle α is the rake angle of the tool and φ_S is the shear plane angle.

Fig. 8-9 shows the comparison of shear plane length for the conventional and SDM machining with vertical and square defects. A significant reduction in shear plane length can be observed from 14 µm in conventional to maximum of 8 µm and 11 µm when machining with vertical and square defects respectively. The shear plane length varies with reference to defect position and reduces to 4 µm near the defect area. Chip length in the secondary deformation zone was also found to reduce in SDM machining compared with conventional machining.

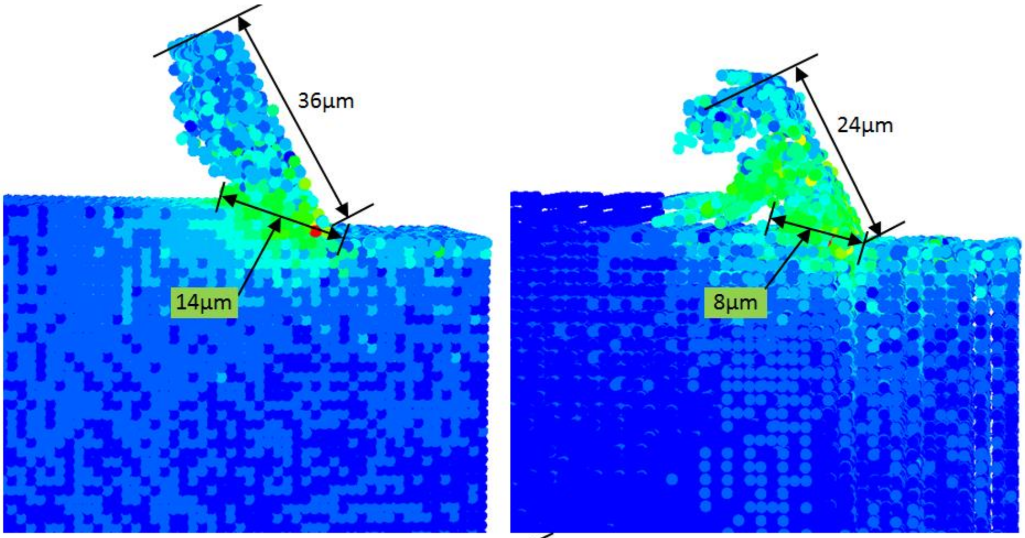

Conventional Vertical defects

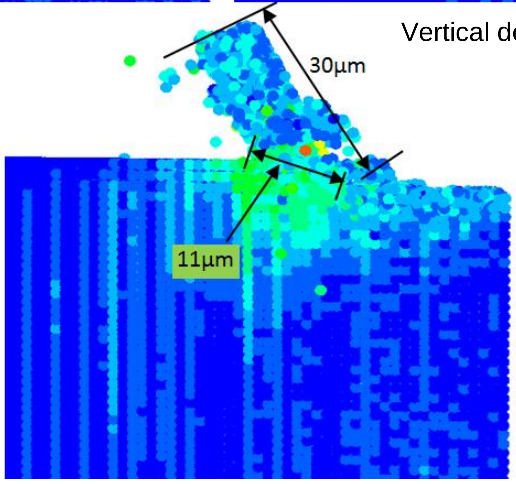

Square defects

Figure 8-9: Comparison of shear plane length in conventional machining and in SDM with vertical defects

The variation in primary shear zone geometry in three different types of defects (including analogous V-type defect for illustration purpose) is explained in Fig. 8-10. It can be seen that in all three types of surface defects, the length of the shear plane (l_{AB}) reduced in slight disparity as well as reduction in shear plane area. The shear plane length varies sequentially throughout the cutting distance travelling through continuous-defect-continuous areas, whereas in conventional machining, this length remains constant throughout the cutting distance. Shear plane area and shear strain magnitude increase when using negative rake angle tool [366] result in higher cutting forces.

In SDM, the depreciation in the shear plane area contributes to the reduction of shear strength of the material in the primary shear zone. The shortening of shear plane length in the primary shear zone also reduces the secondary shear zone eventually reducing cutting resistance. In the primary shear area, a-b-c in all three defects, the length of the upper region (l_{ab}) is shorter than the length of the lower region ((l_{ac}) and therefore endure high strain rate in upper regions than the lower region.

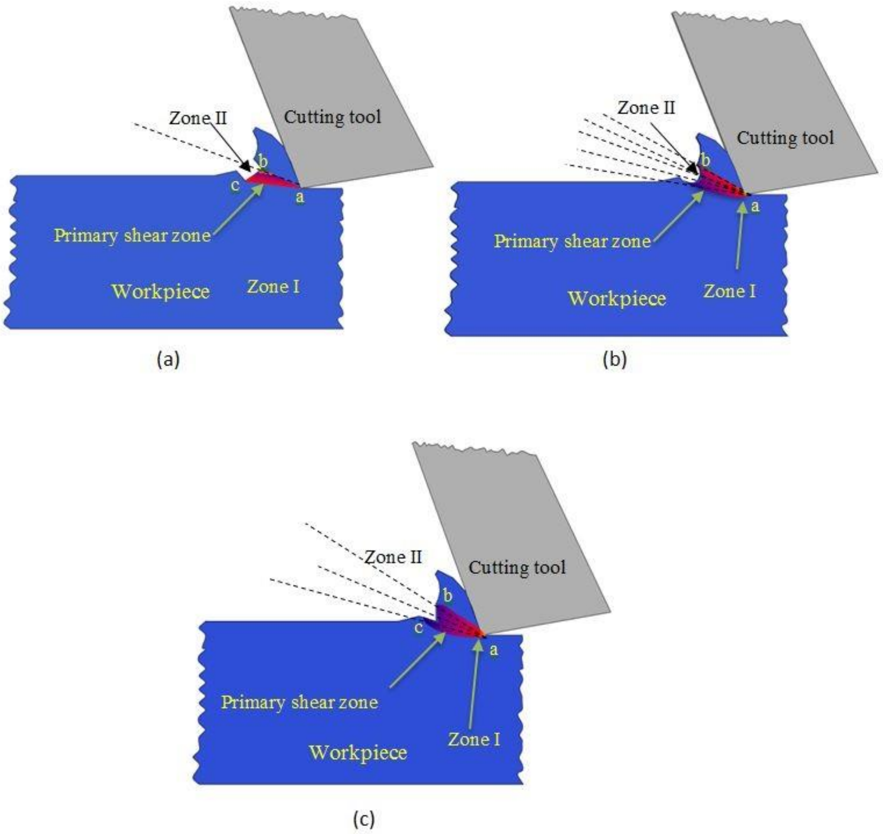

Figure 8-10: Primary shear zone geometry in SDM machining (a) square (b) round (c) V-type defects

Chip separation starts from smaller high-stress state region (zone I) towards larger region (zone II) with maximum stress concentration in both zones. The shape of the region II governs the chip thickness and length. The variation of zone II in square, round and v-type defects offers varied cutting resistance and therefore the difference in chip morphology.

8.7.3 Cutting forces

Fig. 8-11 encompasses the comparison of normal force for multiple surface defects recorded against regular time steps during cutting simulations. The variation in cutting forces trend for multiple surface defects ascertains varied cutting resistance offered by different defects type. The cutting resistance of the material is overwhelmed by the tangential cutting force component (F_c) whereas the negative rake angle of the tool compresses the material layer and causes increase in normal force component (F_n) on the tool [367]. In conventional machining, the cutting force originates with a sharp increase at initial tool contact with the workpiece. The magnitude of cutting force increases during material separation and results in preliminary chip separation from the workpiece and reaching a maximum value. The cutting force stabilises with little disparity due to continuous machined surface in the succeeding cutting.

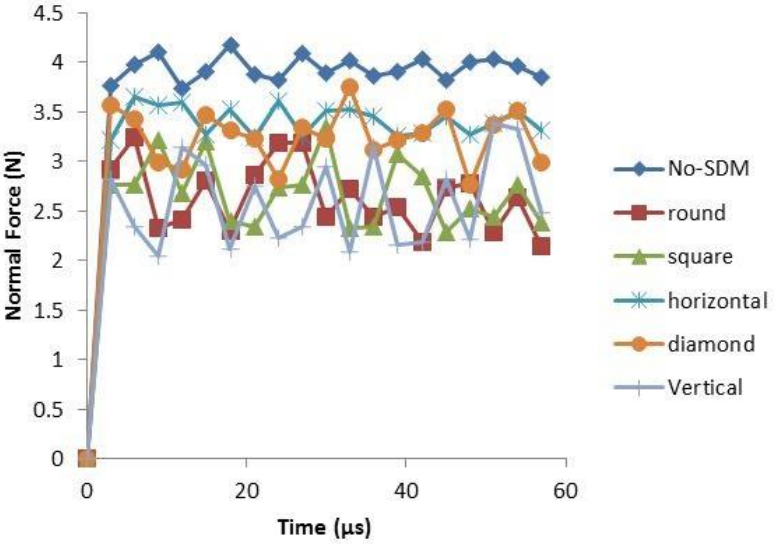

Figure 8-11: Normal force trend of conventional and SDM machining simulation

The SDM process characterised by unique defects forming variable contact pressure and cutting resistance and therefore undergo different cutting force trend. With the initial tool contact with the workpiece surface, the cutting force increases until tool reaches the defect area where the tool faces less resistance due to sporadic contact with the workpiece surface. The cutting force magnitude in all SDM simulations was established lower in comparison with conventional machining. In conventional diamond turning silicon, although the chip morphology is hydrostatic pressure dependent and obtains in the combination of ductile and brittle fracture, in SDM machining, brittle fracture is dominant on the free surface of the chip. This also reduces the secondary shear zone length which consequently reduces the cutting forces [368]. In the horizontal SDM simulation, the highest cutting forces were obtained from other defect type simulations. This is due to the defects existing parallel to the cutting direction which does not considerably affect primary and secondary shear zone area. It can also be observed from Fig. 8-11 that each defect offers a different force magnitude with square and round defects offering the lower cutting forces.

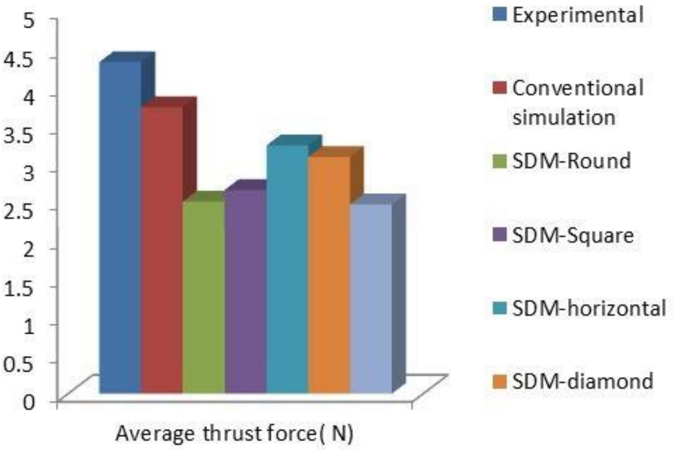

Figure 8-12: Average thrust force comparison of conventional experimental, simulation and SDM methods

A comparison of average thrust force magnitudes in all simulations and experiments was presented in Fig. 8-12, substantiating the effectiveness of SDM method.

8.8 Summary

SPH simulations of orthogonal cutting of conventional and SDM method have been carried out to establish the effectiveness of recently developed SDM method in diamond turning silicon. The efficacy of SDM method was demonstrated by evaluating the material response behaviour under conventional and SDM machining approaches. Cutting forces and steady-state chip formation in different defect type simulations were studied. The study reveals that SDM can be effectively exploited to attain better surface finish and reduced tool wear in single point diamond turning process. Surface defects on the workpiece surface reduce the shear plane area and shear plane length of the primary deformation zone. This phenomenon contributes to lowering the shear strength of the material in the chip formation zone which helps in relaxed chip formation and lower cutting temperature. SDM approach offers reduction in the cutting resistance of the material and therefore a decrease in the cutting energy. Consequently, it reduces diamond tool wear and improves surface finish. The decrease in chip length during SDM machining contributes in reducing the secondary deformation zone length and hence reduced tool wear. Generation of surface defects on the work-piece surface can be easily performed using laser or any other suitable techniques. However sub-surface damage can be accrued due to laser ablation or any other defects generation methods and cause unpredicted brittle fracture. Therefore, SDM method require defects generation at the micron level at which the subsurface defects are homogenized.

Chapter 9- Conclusions and future work

9.1 Assessment of research contribution

The research aimed to gain a deep understanding of cutting process in single point diamond turning of silicon. A numerical simulation model of SPDT of silicon was developed using smoothed particle hydrodynamics approach. The SPH approach adopted in this study provided an effective solution to long-standing mesh distortion issue in FEM. The capability of natural chip separation from the SPH workpiece solely based on particle interaction and material constitutive model provided a true insight of localized chip formation conditions. The cutting process in single point diamond turning of silicon was investigated using different tool geometry and by modifying the workpiece geometry. From the tool perspective, experimental machining along with numerical simulation of machining of silicon was investigated with different rake angle tools. Also, ductile to brittle transition phenomenon of silicon with varying tool edge conditions (progressive tool wear) was explored. This provided the path to optimize the tool geometry and control the ductile mode machining of silicon for better tool performance. From the workpiece geometry perspective, numerical simulation of machining of silicon with different predefined surface defects were found to improve the cutting performance in terms of machinability and tool performance.

The key advancement and improvement of this research work against the state of the art research are obtained through a comprehensive study of the completely ductile and brittle response of silicon during experiments, and analysis of localised information of the distribution of stresses in the primary, secondary and tertiary deformation zones during numerical simulations. The experimental work on different diamond turning machines and in different environments provided repeatability assessment and evaluation of machining process. The output variables including cutting forces, von Mises stress, hydrostatic stress and shear deformation zone conditions are predicted with high certainty. Overall, the thesis has provided further insight into the development of deterministic machining of silicon.

The contribution to knowledge and novelty of this research work is summarized as follows:

- The development of SPH model to simulate the SPDT process of silicon which can offer natural chip separation and predict the true stress-strain behavior of the material.
- Determination of Drucker-Prager constitutive model parameters for silicon that provides the basis for the exploitation of cutting mechanics of silicon by using numerical methods.
- Proposing a new quantitative evaluation parameter for the tool wear resistance performance.
- A very first experimental study of the determination of Johnson-Cook constants for silicon using high strain rate split Hopkinson tests and quasi-static test to predict the machining response behavior of silicon.

9.2 Conclusions

The combined experimental and smoothed particle hydrodynamics approach provided an in-depth understanding to establish the distinct conditions for the ductile to brittle transition (DBT) and brittle to ductile transition (BDT). The major findings meeting the research objectives are summarised as follows:

I. In the diamond turning of silicon, the uniform distribution of the required hydrostatic pressure under and in front of the cutting edge becomes a decisive criterion for DBT when the diamond tool gets worn. The uniform distribution highly relies on the tool geometry and significantly varies as a function of rake angle. For the similar tool wear pattern, diamond tool with (-25°) can maintain uniform hydrostatic stress for longer cutting distance compared to (-30°) and (-40°) tools.

II. The formation of multiple phases of silicon due to high hydrostatic pressure using higher negative rake angle tools increase indeterminism of the machining process. This is due to different physical and chemical properties of the transformed phases and different affinity towards the diamond tool that contribute to high frictional resistance and asymmetric hydrostatic pressure.

III. Surface defect machining approach is an effective approach to improve the machinability of silicon in SPDT. The pre-generated defects on the silicon surface can reduce the shear plane area and length and hence frictional resistance to cutting is reduced. As thus, tool wear is deferred and machined surface quality is improved.

IV. Abrasive wear is the dominant wear mechanism of diamond tools in SPDT of silicon, independent of rake angle. The groove wear is the common wear pattern found on the clearance face of the tool along with chipping damage on the tool rake face.

V. During SPDT of silicon, the ductile to brittle transition initiates due to low frictional wear of the tool. This leads to formation of lateral cracks which will transform into brittle damages with further increase of tool wear. Superficial ploughing due to the groove wear of the tool also deteriorates the machined surface.

VI. Tool wear changes the distribution of hydrostatic pressure on the silicon surface along the tool cutting edge. With the groove pattern, the magnitude of the hydrostatic pressure fluctuates significantly between two nearest points, results in the removal of material through brittle fractures.

VII. With the increase of flank wear, the stresses increase in the tertiary shear zone and the maximum failure stress travels from the front of cutting edge towards the machined surface, results in deterioration of the machined surface.

VIII. During the quasi-static and high dynamic compression test, the yield strength of silicon increases with the increment of the strain rate.

9.3 Recommendation for future work

During this research work, the capabilities and limitations of experimental diamond turning and smoothed particle hydrodynamics process were identified. The required critical future work is summarized in the following sections.

9.3.1 Development of dedicated module for SPH

Since the development of SPH in 1977, the method has been frequently adopted in FEM for various applications from metal machining and forming to impact testing. The method has been found very effective in predicting the deformation behaviour of materials in large deformation processes. However, the method has yet not been efficiently implemented in the currently available general-purpose FEM packages as well as dedicated machining software. The implementation of SPH method in FE codes lacks in terms of an interactive module or environment, computational efficiency, and thermo-mechanical analysis capabilities. The optimization of FE codes with the two and three-dimensional SPH modelling capabilities, the coupled mechanical and thermal analysis, as well as a user-friendly module can surely push for the research and commercial exploitation of SPH approach.

9.3.2 Development of material constitutive model and parameters

The FE simulation of machining of silicon and similar brittle material suffer the limitation of a sophisticated pressure-dependent material constitutive model. There is a strong need to develop a pressure-dependent constitutive model to accurately predict the failure of hard and brittle materials (silicon, silicon carbide, silicon nitride, etc.) and to implement it in FE software.

9.3.3 Determination of plasticity and damage model parameters

One of the main reasons of scarce evaluation of machining of silicon using FEM is the unavailability of material model parameters. The ductile deformation of silicon can be predicted using Johnson-Cook model as well as a pressure-dependent Drucker-Prager model. However, no material model parameters are available for silicon for both the plasticity models. There is a strong need to perform an empirical study of uniaxial and triaxial compression, tensile and torsion tests to determine the required parameter.

9.3.4 Coupled thermo-mechanical analysis and machining conditions

Due to the limitations of FE code, simulation of machining using SPH was based on mechanical analysis and the thermal effects during chip formation were not studied. The generation of temperature during chip formation certainly influences the tribo-chemistry of diamond tool. The SPH machining of silicon using coupled thermo-mechanical analysis provides an inclusive understanding of chip formation in SPDT. In addition, SPH simulations could be performed for the cryogenic, micro-laser assisted and vibration-assisted machining.

9.3.5 Surface defect machining method

The simulation study of surface defect machining of silicon demonstrated the optimization of SPDT process through improved surface quality and reduced diamond tool wear. Experimental trials are required to validate the simulation model with certainty. Surface defects can be generated using thermal and mechanical methods. It needs further investigation of optimized surface defects pattern to further improve the machining performance.

9.3.6 Optimization of tool geometry

The experimental study using different tool geometry demonstrated the effectiveness of lower negative rake angle (-25°) in obtaining longer ductile mode machining of silicon. However, the tool with (-30°) rake angle was found to undergo higher frictional resistance and the least ductile cutting distance in all the trials compared to (-40°). A high error difference of 30% between experimental and numerical cutting forces was observed. Further experimental trials are required to be performed to evaluate the performance of diamond tools with (-30°) rake angles with different crystal orientation of diamond tool and silicon workpiece as well as different tool nose radius.

References

1. Brinksmeier, E., R. Gläbe, and L. Schönemann, *Review on diamond-machining processes for the generation of functional surface structures.* CIRP Journal of Manufacturing Science and Technology, 2012. **5**(1): p. 1-7.
2. Sze-Wei, G., et al., *A fine tool servo system for global position error compensation for a miniature ultra-precision lathe.* International Journal of Machine Tools and Manufacture, 2007. **47**(7-8): p. 1302-1310.
3. Kim, H.-S. and E.-J. Kim, *Feed-forward control of fast tool servo for real-time correction of spindle error in diamond turning of flat surfaces.* International Journal of Machine Tools and Manufacture, 2003. **43**(12): p. 1177-1183.
4. Morris, J.C., et al., *Origins of the Ductile Regime in Single-Point Diamond Turning of Semiconductors.* Journal of the American Ceramic Society, 1995. **78**(8): p. 2015-2020.
5. Patten, J., W. Gao, and K. Yasuto, *Ductile Regime Nanomachining of Single-Crystal Silicon Carbide.* Journal of Manufacturing Science and Engineering, 2005. **127**(3): p. 522.
6. Mariayyah, R., J.P. Patten, and H.P. Cherukuri, *Relationship between Machining Forces and Diamond Tool Wear during Ductile Regime Machining of Silicon Nitride.* Machining Science and Technology, 2012. **16**(1): p. 53-70.
7. Goel, S., et al., *Diamond machining of silicon: A review of advances in molecular dynamics simulation.* International Journal of Machine Tools and Manufacture, 2015. **88**: p. 131-164.
8. Patten, J.A. and W. Gao, *Extreme negative rake angle technique for single point diamond nano-cutting of silicon.* Precision Engineering, 2001. **25**(2): p. 165-167.
9. Blake, P.N. and R.O. Scattergood, *Ductile-Regime Machining of Germanium and Silicon.* Journal of the American Ceramic Society, 1990. **73**(4): p. 949-957.
10. Blackley, W.S. and R.O. Scattergood, *Ductile-Regime Machining Model for Diamond Turning of Brittle Materials.* Precision Engineering-Journal of the American Society for Precision Engineering, 1991. **13**(2): p. 95-103.
11. Evans, C.J. and J.B. Bryan, *“Structured”, “Textured” or “Engineered” Surfaces.* CIRP Annals - Manufacturing Technology, 1999. **48**(2): p. 541-556.
12. Yu, D.P., Y.S. Wong, and G.S. Hong, *Ultraprecision machining of micro-structured functional surfaces on brittle materials.* Journal of Micromechanics and Microengineering, 2011. **21**(9): p. 095011.
13. Dou, Z., et al., *Fabrication of a micro-structured surface based on interfacial convection for drag reduction.* Chinese Science Bulletin, 2011. **56**(7): p. 626-632.
14. Cho, S.J., et al., *One-Step Fabrication of Hierarchically Structured Silicon Surfaces and Modification of Their Morphologies Using Sacrificial Layers.* Journal of Nanomaterials, 2013. **2013**: p. 1-8.

15. Hansen, H.N., R.J. Hocken, and G. Tosello, *Replication of micro and nano surface geometries.* CIRP Annals - Manufacturing Technology, 2011. **60**(2): p. 695-714.
16. Murray, J.W., et al., *Surface finishing of intricate metal mould structures by large-area electron beam irradiation.* Precision Engineering, 2013. **37**(2): p. 443-450.
17. Masuzawa, T., *State of the Art of Micromachining.* CIRP Annals - Manufacturing Technology, 2000. **49**(2): p. 473-488.
18. Leech, P.W., et al., *Fabrication of hologram coins using electron beam lithography.* Microelectronic Engineering, 2004. **71**(2): p. 171-176.
19. Zhong, K., et al., *Fabrication of continuous relief micro-optic elements using real-time maskless lithography technique based on DMD.* Optics & Laser Technology, 2014. **56**: p. 367-371.
20. R.J. Winfield, M.M., G.M. Crean, S. Paineau, *Excimer laser fabrication of diffractive optical elements.* Materials Science in Semiconductor Processing, 2000. **3**: p. 481-486.
21. Rudolf L., V.R., *A review of holograms and other microstructures as security features*, in *Optical Sciences*. 1999, Vanrenesse Consulting.
22. Heckele, M., et al., *<title>Large-area polymer replication for microfluidic devices</title>*, in *Design, Test, Integration, and Packaging of MEMS/MOEMS 2001*. 2001, SPIE-Intl Soc Optical Eng.
23. Kusko, M., Dinescu, A., Cristea, D., Apostol, D. and Schiopu, *design and fabrication with electron beam lithography of a diffractive optical element.* U.P.B Sci, 2009. **Bull Series, 71**: p. 135-142.
24. Gåhlin, R., et al., *Designed abrasive diamond surfaces.* Wear, 1999. **233-235**: p. 387-394.
25. Wilson, D.W., et al., *Recent advances in blazed grating fabrication by electron-beam lithography*, in *Current Developments in Lens Design and Optical Engineering IV*. 2003, SPIE-Intl Soc Optical Eng.
26. Evans, C.J., *Precision engineering: an evolutionary perspective.* Philos Trans A Math Phys Eng Sci, 2012. **370**(1973): p. 3835-51.
27. Taniguchi, N., *current status in, and future trends of ultraprecision machining and ultrafine materials processing.* CIRP Annals - Manufacturing Technology, 1983. **32**(2): p. 573-582.
28. Zhou, J., et al., *Fabrication of continuous diffractive optical elements using a fast tool servo diamond turning process.* J. Micromech. Microeng., 2013. **23**(7): p. 075010.
29. Glabe, R., Schonemann, L., Lunemann, B., Schotten, A. and Brinksmeier, E. (*Two novel diamond machining technologies for machining new types of optical structures*, in *Laboratory for Precision Machining LFM*. University of Bremen, Germany.
30. Brinksmeier, E., Lunemann, B., Glabe, R., von Kopylow, C., Falldorf, C. and Dankwart, C. *open loop fast tool servo with nanometer accuracy for diamond machining of diffractive structures*. 2008.
31. Barkman, M.L., et al., *Free-form machining for micro-imaging systems - art. no. 68830G.* Advanced Fabrication Technologies for Micro/Nano Optics and Photonics, 2008. **6883**: p. G8830-G8830.

32. Donaldson, R.a.P., S. , *Design and construction of a large vertical axis diamond turning machine.* SPIE's 27th Annual International Technical Symposium and Instrument Display, 1983. **433**: p. 62-67.
33. Thompson, D., Chrislock, J. and Newton, L. , *Development of an inexpensive high accuracy diamond turning machine.* Precision Engineering, , 1982. **II** p. 144--153.
34. Shinno, H., et al., *Structural Configuration and Performances of Machining Environment-Controlled Ultraprecision Diamond Turning Machine 'Capsule'.* CIRP Annals - Manufacturing Technology, 1992. **41**(1): p. 425-428.
35. Allen, W., et al., *A high performance embedded machine tool controller.* Microprocessing and microprogramming, 1994. **40(2)**(179-191).
36. Scheiding, S., et al., *Freeform manufacturing of a microoptical lens array on a steep curved substrate by use of a voice coil fast tool servo.* Opt. Express, 2011. **19**(24): p. 23938.
37. Liu, Q., et al., *Long-stroke fast tool servo and a tool setting method for freeform optics fabrication.* Optical Engineering, 2014. **53**(9).
38. Yu, D.P., Y.S. Wong, and G.S. Hong, *Ultraprecision machining of micro-structured functional surfaces on brittle materials.* Journal of Micromechanics and Microengineering, 2011. **21**(9).
39. Nakayama, K., *Topics on Fundamentals of Precision Machining.* Machining Science and Technology, 1997. **1**(2): p. 251-262.
40. Kanda, H. and S. Yamaoka, *Inhomogeneous Distribution of Nitrogen Impurities in (111) Growth Sectors of High-Pressure Synthetic Diamond.* Diamond and Related Materials, 1993. **2**(11): p. 1420-1423.
41. Kamo, M., et al., *Diamond Synthesis from Gas-Phase in Microwave Plasma.* Journal of Crystal Growth, 1983. **62**(3): p. 642-644.
42. Sharif Uddin, M., et al., *Effect of crystallographic orientation on wear of diamond tools for nano-scale ductile cutting of silicon.* Wear, 2004. **257**(7-8): p. 751-759.
43. Uddin, M.S., et al., *Performance of single crystal diamond tools in ductile mode cutting of silicon.* Journal of Materials Processing Technology, 2007. **185**(1-3): p. 24-30.
44. Cheng, K., et al., *Modeling and simulation of the tool wear in nanometric cutting.* Wear, 2003. **255**(7-12): p. 1427-1432.
45. King, R.F. and D.F. Tabor, *The strength properties and frictional behaviour of brittle solids.* Proceedings of royal society of London, 1954. **223**(1115): p. 225-238.
46. Huerta, M. and S. Malkin, *Grinding of glass the Mechanics of the Process.* journal of Engineering for Industry, 1976: p. 459-467.
47. Toh, S.B. and R. McPherson, *Plastic Deformation During the Abrasive Wear of Ceramics.* 1984: p. 723-732.
48. Moore, M.A. and F.S. King, *Fracture vs Plastic Deformation Processes in the Sliding Abrasive Wear of Ceramics.* wear, 1980. **60**: p. 123-140.
49. Bifano, T.G., T.A. Dow, and R.O. Scattergood, *Ductile-Regime Grinding - a New Technology for Machining Brittle Materials.* Journal of Engineering for Industry-Transactions of the Asme, 1991. **113**(2): p. 184-189.

50. Jamieson, J.C., *Crystal Structures at High Pressures of Metallic Modifications of Silicon and Germanium.* Science, 1963. **139**(3556): p. 762-4.
51. Gilman, J.J., *Insulator-Metal Transitions at Microindentations.* Journal of Materials Research, 1992. **7**(3): p. 535-538.
52. Gilman, J.J., *Mechanism of Shear-Induced Metallization.* Czechoslovak Journal of Physics, 1995. **45**(11): p. 913-919.
53. Jeong, S.-M., et al., *Phase Transformation of Single Crystalline Silicon by Scratching.* Japanese Journal of Applied Physics, 2003. **42**(Part 1, No. 5A): p. 2773-2774.
54. Zarudi, I., et al., *The R8-BC8 phases and crystal growth in monocrystalline silicon under microindentation with a spherical indenter.* Journal of Materials Research, 2004. **19**(1): p. 332-337.
55. Jasinevicius, R.G., J.G. Duduch, and A.J.V. Porto, *Investigation on diamond turning of silicon crystal - generation mechanism of surface cut with worn tool.* Journal of the Brazilian Society of Mechanical Sciences, 2001. **23**(2): p. 241-252.
56. Goel, S., et al., *Nanoindentation of polysilicon and single crystal silicon: Molecular dynamics simulation and experimental validation.* Journal of Physics D: Applied Physics, 2014. **47**(27): p. 275304.
57. Shibata, T., et al., *Ductile-regime turning mechanism of single-crystal silicon.* Precision Engineering, 1996. **18**(2-3): p. 129-137.
58. Jang, J.-i., et al., *Indentation-induced phase transformations in silicon: influences of load, rate and indenter angle on the transformation behavior.* Acta Materialia, 2005. **53**(6): p. 1759-1770.
59. Zhang, L.C., *Plasticity in monocrystalline silicon: experiment and modelling.* Advances in Engineering Plasticity and Its Applications, Pts 1 and 2, 2004. **274-276**: p. 1-9.
60. Bradby, J.E., et al., *Mechanical deformation in silicon by micro-indentation.* Journal of Materials Research, 2001. **16**(05): p. 1500-1507.
61. Juliano, T., Y. Gogotsi, and V. Domnich, *Effect of indentation unloading conditions on phase transformation induced events in silicon.* Journal of Materials Research, 2003. **18**(05): p. 1192-1201.
62. Kailer, A., Y.G. Gogotsi, and K.G. Nickel, *Phase transformations of silicon caused by contact loading.* Journal of Applied Physics, 1997. **81**(7): p. 3057.
63. Jasinevicius, R., Porto, A., Duduch, J., Pizani, P., Lanciotti Jr., F. and Santos, F. , *Multiple phases in silicon submicrometer chips removed by diamond turning.* J. Braz. Soc. Mech. Sci. & Eng., 2005. **27**(4): p. 440-448.
64. Zeng, Z., et al., *Phase transitions in metastable phases of silicon.* Journal of Applied Physics, 2014. **115**(10): p. 103514.
65. Pirouz, P., et al., *The martensitic transformation in silicon—I experimental observations.* Acta Metallurgica et Materialia, 1990. **38**(2): p. 313-322.
66. Lawn, B.R., T. Jensen, and A. Arora, *Brittleness as an Indentation Size Effect.* Journal of Materials Science, 1976. **11**(3): p. 573-575.

67. Lawn, B. and R. Wilshaw, *Indentation fracture: principles and applications.* Journal of Materials science, 1975. **10**(6): p. 1049-1081.

68. Leung, T.P., W.B. Lee, and X.M. Lu, *Diamond turning of silicon substrates in ductile-regime.* Journal of Materials Processing Technology, 1998. **73**(1-3): p. 42-48.

69. Yan, J., et al., *Ductile regime turning at large tool feed.* Journal of Materials Processing Technology, 2002. **121**(2-3): p. 363-372.

70. Chao, C.L.M., K. J.;Liu, D. S.;Bai, C. Y.;Shy, T. L., *Ductile behaviour in single-point diamond-turning of single-crystal silicon.* Journal of Materials Processing Technology, 2002. **127**(2): p. 187-190.

71. Astakhov, *Fundamentals of the selection of cutting tool geometry parameters geometry of single point turning tools and drills*. Springer. 2010, London.

72. Fang, F.Z. and V.C. Venkatesh, *Diamond Cutting of Silicon with Nanometric Finish.* CIRP Annals - Manufacturing Technology, 1998. **47**(1): p. 45-49.

73. Arefin, S., et al., *The effect of the cutting edge radius on a machined surface in the nanoscale ductile mode cutting of silicon wafer.* Proceedings of the Institution of Mechanical Engineers Part B-Journal of Engineering Manufacture, 2007. **221**(2): p. 213-220.

74. Cai, M.B., X.P. Li, and M. Rahman, *Study of the temperature and stress in nanoscale ductile mode cutting of silicon using molecular dynamics simulation.* Journal of Materials Processing Technology, 2007. **192-193**: p. 607-612.

75. Cai, M.B., et al., *Crack initiation in relation to the tool edge radius and cutting conditions in nanoscale cutting of silicon.* International Journal of Machine Tools & Manufacture, 2007. **47**(3-4): p. 562-569.

76. Khurshudov, A.G., K. Kato, and H. Koide, *Wear of the AFM diamond tip sliding against silicon.* Wear, 1997. **203**: p. 22-27.

77. Paul, E., et al., *Chemical aspects of tool wear in single point diamond turning.* Precision Engineering-Journal of the International Societies for Precision Engineering and Nanotechnology, 1996. **18**(1): p. 4-19.

78. Jia, P. and M. Zhou, *Tool wear and its effect on surface roughness in diamond cutting of glass soda-lime.* Chinese Journal of Mechanical Engineering, 2012. **25**(6): p. 1224-1230.

79. Zareena, A.R. and S.C. Veldhuis, *Tool wear mechanisms and tool life enhancement in ultra-precision machining of titanium.* Journal of Materials Processing Technology, 2012. **212**(3): p. 560-570.

80. Shimada, S., et al., *Suppression of Tool Wear in Diamond Turning of Copper under Reduced Oxygen Atmosphere.* CIRP Annals - Manufacturing Technology, 2000. **49**(1): p. 21-24.

81. Zhou, M., et al., *Tool wear and surface finish in diamond cutting of optical glass.* Journal of Materials Processing Technology, 2006. **174**(1-3): p. 29-33.

82. Wong, C.J., *Fracture and Wear of Diamond Cutting Tools.* Journal of Engineering Materials and Technology, 1981. **103**(4): p. 341.

83. Fang, F.Z., X.D. Liu, and L.C. Lee, *Micro-machining of optical glasses - A review of diamond-cutting glasses.* Sadhana-Academy Proceedings in Engineering Sciences, 2003. **28**: p. 945-955.
84. Yan, J., K. Syoji, and J.i. Tamaki, *Some observations on the wear of diamond tools in ultra-precision cutting of single-crystal silicon.* Wear, 2003. **255**(7-12): p. 1380-1387.
85. Li, X.P., T. He, and M. Rahman, *Tool wear characteristics and their effects on nanoscale ductile mode cutting of silicon wafer.* Wear, 2005. **259**(7-12): p. 1207-1214.
86. Kawasegi, N., et al., *Development of cutting tools with microscale and nanoscale textures to improve frictional behavior.* Precision Engineering, 2009. **33**(3): p. 248-254.
87. Obikawa, T., et al., *Micro-texture at the coated tool face for high performance cutting.* International Journal of Machine Tools and Manufacture, 2011. **51**(12): p. 966-972.
88. Sugihara, T. and T. Enomoto, *Development of a cutting tool with a nano/micro-textured surface—Improvement of anti-adhesive effect by considering the texture patterns.* Precision Engineering, 2009. **33**(4): p. 425-429.
89. Ravindra, D., M.K. Ghantasala, and J. Patten, *Ductile mode material removal and high-pressure phase transformation in silicon during micro-laser assisted machining.* Precision Engineering, 2012. **36**(2): p. 364-367.
90. Mohammadi, H., et al., *Experimental work on micro laser-assisted diamond turning of silicon (111).* Journal of Manufacturing Processes, 2015. **19**: p. 125-128.
91. Tang, X., et al., *Ultraprecision micromachining of hard material with tool wear suppression by using diamond tool with special chamfer.* CIRP Annals - Manufacturing Technology, 2013. **62**(1): p. 51-54.
92. Tanaka, H. and S. Shimada, *Damage-free machining of monocrystalline silicon carbide.* CIRP Annals - Manufacturing Technology, 2013. **62**(1): p. 55-58.
93. Suzuki, H., et al., *Development of micro milling tool made of single crystalline diamond for ceramic cutting.* CIRP Annals - Manufacturing Technology, 2013. **62**(1): p. 59-62.
94. Wang, Z.Y. and K.P. Rajurkar, *Cryogenic machining of hard-to-cut materials.* Wear, 2000. **239**(2): p. 168-175.
95. Ghosh, R., *Technology Assessment on current Advanced Research Projects in Cryogenic Machining*. 2006. p. 1-87.
96. Umbrello, D., F. Micari, and I.S. Jawahir, *The effects of cryogenic cooling on surface integrity in hard machining: A comparison with dry machining.* CIRP Annals - Manufacturing Technology, 2012. **61**(1): p. 103-106.
97. Kumar, M.N., et al., *Vibration Assisted Conventional and Advanced Machining: A Review.* Procedia Engineering, 2014. **97**: p. 1577-1586.
98. Skelton, R.C., *Turning with an oscillating tool.* International journal of mach. tool Des. Res, 1967. **8**: p. 239-259.

99. Brehl, D.E. and T.A. Dow, *Review of vibration-assisted machining.* Precision Engineering, 2008. **32**(3): p. 153-172.
100. Venkatesan, K., R. Ramanujam, and P. Kuppan, *Laser Assisted Machining of Difficult to Cut Materials: Research Opportunities and Future Directions - A Comprehensive Review.* Procedia Engineering, 2014. **97**: p. 1626-1636.
101. Xavierarockiaraj, S. and P. Kuppan, *Investigation of Cutting Forces, Surface Roughness and Tool Wear during Laser Assisted Machining of SKD11Tool Steel.* Procedia Engineering, 2014. **97**: p. 1657-1666.
102. Rahman Rashid, R.A., et al., *An investigation of cutting forces and cutting temperatures during laser-assisted machining of the Ti–6Cr–5Mo–5V–4Al beta titanium alloy.* International Journal of Machine Tools and Manufacture, 2012. **63**: p. 58-69.
103. Arrazola, P.J., et al., *Recent advances in modelling of metal machining processes.* CIRP Annals - Manufacturing Technology, 2013. **62**(2): p. 695-718.
104. Jawahir, I.S., et al., *Surface integrity in material removal processes: Recent advances.* CIRP Annals - Manufacturing Technology, 2011. **60**(2): p. 603-626.
105. Solar, M., et al., *Mechanical behavior of linear amorphous polymers: comparison between molecular dynamics and finite-element simulations.* Phys Rev E Stat Nonlin Soft Matter Phys, 2012. **85**(2 Pt 1): p. 021808.
106. Strenkowski, J.S. and J.T. Carroll, *a finite element model of orthogonal metal cutting.* journal of engineering for industry, 1985. **107**(4): p. 349.
107. Aspinwall, D.K. and S.L. Soo, *Developments in modelling of metal cutting processes.* Proceedings of the Institution of Mechanical Engineers, Part L: Journal of Materials: Design and Applications, 2007. **221**(4): p. 197-211.
108. Engelmann, B.E. and J.O. Hallquist, *NIKE2D: A non linear implicit two dimensional finite element code for solid mechanics*, in *User manual*, L.L.N. Laboratory, Editor. 1991.
109. Sadat, A.B., M.Y. Reddy, and B.P. Wang, *plastic-deformation analysis in machining of inconel-718 nickel-base superalloy using both experimental and numerical-methods.* International Journal of Mechanical Sciences, 1991. **33**(10): p. 829-842.
110. Bäker, M., J. Rösler, and C. Siemers, *A finite element model of high speed metal cutting with adiabatic shearing.* Computers & Structures, 2002. **80**(5-6): p. 495-513.
111. Chen, G., et al., *Finite element simulation of high-speed machining of titanium alloy (Ti–6Al–4V) based on ductile failure model.* The International Journal of Advanced Manufacturing Technology, 2011. **56**(9-12): p. 1027-1038.
112. Haddag, B., et al., *Finite element formulation effect in three-dimensional modeling of a chip formation during machining.* International Journal of Material Forming, 2010. **3**(S1): p. 527-530.

113. Gao, C.Y., *FE realization of thermo-visco-plastic constitutive models using VUMAT in ABAQUS/Explicit Program.* Computational Mechanics ISCM2007, 2007: p. 623-628.
114. Arrazola, P.J. and T. Özel, *Numerical modelling of 3D hard turning using arbitrary Lagrangian Eulerian finite element method.* Mechanical Engineering, 2008. **3**(3): p. 238-249.
115. Ozel, T., et al., *3d finite element modelling of chip formation process for machining inconel 718: comparison of fe software predictions.* Machining Science and Technology, 2011. **15**(1): p. 21-46.
116. Limido, J., et al., *SPH method applied to high speed cutting modelling.* International Journal of Mechanical Sciences, 2007. **49**(7): p. 898-908.
117. Schwer, L., *Optional Strain-Rate forms for theJohnson Cook constitutive model and the role of the parameter epsilon _ 01.* 6th European LS_DYNA Users' Conference, 2007: p. 1-17.
118. Majumdar, P., R. Jayaramachandran, and S. Ganesan, *Finite element analysis of temperature rise in metal cutting processes.* Applied Thermal Engineering, 2005. **25**(14-15): p. 2152-2168.
119. Bil, H., S.E. Kılıç, and A.E. Tekkaya, *A comparison of orthogonal cutting data from experiments with three different finite element models.* International Journal of Machine Tools and Manufacture, 2004. **44**(9): p. 933-944.
120. Branis, A.S. and D.E. Manolakos, *Finite element simulation of chip formation in orthogonal metal cutting.* Journal of Materials Processing Technology, 2001. **110**: p. 19-27.
121. Yen, Y.-C., A. Jain, and T. Altan, *A finite element analysis of orthogonal machining using different tool edge geometries.* Journal of Materials Processing Technology, 2004. **146**(1): p. 72-81.
122. Shih, A.J., *Finite Element Analysis of the Rake Angle Effects in orthogonal metal cutting.* International Journal of Mechanical Sciences, 1996. **38**(1): p. 1-17.
123. Özel, T., *Computational modelling of 3D turning: Influence of edge micro-geometry on forces, stresses, friction and tool wear in PcBN tooling.* Journal of Materials Processing Technology, 2009. **209**(11): p. 5167-5177.
124. Moriwaki, T., N. Sugimura, and S. Luan, C*ombined stress, material flow and heat analysis of orthogonal micromachining of copper.* CIRP Annals - Manufacturing Technology, 1993. **42**(1): p. 75-78.
125. Muraka, P.D., G. Barrow, and S. Hinduja, *Influence of the process variables on the temperature distribution in orthogonal machining using the finite element method.* International Journal of Mechanical Sciences, 1979. **21**(8): p. 445-456.
126. Davoudinejad, A., et al., *Finite element simulation and validation of chip formation and cutting forces in dry and cryogenic cutting of Ti–6Al–4V.* Procedia Manufacturing, 2015. **1**: p. 728-739.
127. Pu, Z., et al., *Finite element simulation of residual stresses in cryogenic machining of AZ31B Mg alloy.* Procedia CIRP, 2014. **13**: p. 282-287.
128. Mohammadpour, M., M.R. Razfar, and R. Jalili Saffar, *Numerical investigating the effect of machining parameters on residual stresses in*

orthogonal cutting. Simulation Modelling Practice and Theory, 2010. **18**(3): p. 378-389.

129. Ali, M.H., et al., *FEM to predict the effect of feed rate on surface roughness with cutting force during face milling of titanium alloy.* HBRC Journal, 2013. **9**(3): p. 263-269.
130. Korkut, I. and M.A. Donertas, *The influence of feed rate and cutting speed on the cutting forces, surface roughness and tool–chip contact length during face milling.* Materials & Design, 2007. **28**(1): p. 308-312.
131. Rotella, G. and D. Umbrello, *Finite element modeling of microstructural changes in dry and cryogenic cutting of Ti6Al4V alloy.* CIRP Annals - Manufacturing Technology, 2014. **63**(1): p. 69-72.
132. Shet, C., X. Deng, and A. E. Bayoumi, *Finite element simulation of high-pressure water-jet assisted metal cutting.* International Journal of Mechanical Sciences, 2003. **45**(6-7): p. 1201-1228.
133. Banerjee, N. and A. Sharma, *Identification of a friction model for minimum quantity lubrication machining.* Journal of Cleaner Production, 2014. **83**: p. 437-443.
134. Abolfazl Zahedi, S., et al., *FE/SPH modelling of orthogonal micro-machining of f.c.c. single crystal.* Computational Materials Science, 2013. **78**: p. 104-109.
135. Demiral, M., A. Roy, and V.V. Silberschmidt, *Strain-gradient crystal-plasticity modelling of micro-cutting of b.c.c. single crystal.* Meccanica, 2015. **51**(2): p. 371-381.
136. E. Ceretti, p.F., W. T. Wu , T. Altan, *Application of 2D FEM to chip formation in orthogonal cutting.* Journal of Materials Processing Technology, 1996. **59**: p. 169-180.
137. Chen, L., T.I. El-Wardany, and W.C. Harris, *Modelling the effects of flank wear land and chip formation on residual stresses.* CIRP Annals - Manufacturing Technology, 2004. **53**(1): p. 95-98.
138. Carroll, J.T. and J.S. Strenkowski, *Finite element models of orthogonal cutting with application to single point diamond turning.* International Journal of Mechanical Sciences, 1988. **30**(12): p. 899-920.
139. Lin, Z.C. and W.C. Pan, *A thermoelastic-plastic large deformation model for orthogonal cutting with tool flank wear - Part 1: Computational Procedures.* International Journal of Mechanical Sciences, 1993. **35**(10): p. 829-840.
140. Usui E, S.T., *Mechanics of machining- From descriptive to predictive theory, on the art of cutting metals-75 years later a tribute to F W Taylor.* ADME PED, 1982. **7**: p. 13-30.
141. Zhang, L., *On the seperation criteria in the simulation of orthogonal metal cutting using the finite element method.* Journal of Materials Processing Technology, 1999. **89-90**: p. 273-278.
142. Movahhedy, M., M.S. Gadala, and Y. Altintas, *Simulation of the orthogonal metal cutting process using an arbitrary Lagrangian–Eulerian finite-element method.* Journal of Materials Processing Technology, 2000. **103**(2): p. 267-275.

143. Sekhon, G.S. and J.L. Chenot, N*umerical simulation of continuous chip formation during non-steady orthogonal cutting.* Engineering Computations, 1993. **10**(1): p. 31-48.
144. Shih, A.J. and H.T.Y. Yang, *Experimental and finite element predictions of residual stresses due to orthogonal metal cutting.* International Journal for Numerical Methods in Engineering, 1993. **36**(9): p. 1487-1507.
145. Zanger, F., N. Boev, and V. Schulze, *Novel approach for 3d simulation of a cutting process with adaptive remeshing technique.* Procedia CIRP, 2015. **31**: p. 88-93.
146. Davim, J.P., *Machining of hard materials*. 2011, London: Springer.
147. Quiza, R., O. López-Armas, and J.P. Davim, *Finite element in manufacturing processes.* 2012: p. 13-37.
148. Klamecki, B.E., *Incipient chip formation in metal cutting a three dimension finite element analysis :PhD thesis.* University of Illinois, 1973.
149. Amrita Priyadarshinin, S.K.P., Arun K. Samantaray, *Finite element modeling of chip formation in orthogonal machining*, in *statistical and computational techniques in manufacturing*, J.P. Davim, Editor. 2012: London.
150. Komvopoulos, K. and S.A. Erpenbeck, *Finite element modeling of orthogonal metal cutting.* Journal of Engineering for Industry, 1991. **113**(3): p. 253.
151. Shih, A.J., *Finite element simulation of orthogonal metal cutting.* Journal of Manufacturing Science and Engineering, 1995. **117**(1): p. 84-84.
152. Shih, A.J.M., S. Chandrasekar, and H.T.Y. Yang, *Finite element simulation of metal cutting process with strain-rate and temperature effects.* ASME PED, 1990. **43**: p. 11-24.
153. Ducobu, F., E. Rivière-Lorphèvre, and E. Filippi, *Material constitutive model and chip separation criterion influence on the modeling of Ti6Al4V machining with experimental validation in strictly orthogonal cutting condition.* International Journal of Mechanical Sciences, 2016. **107**: p. 136-149.
154. Mahnama, M. and M.R. Movahhedy, *Application of FEM simulation of chip formation to stability analysis in orthogonal cutting process.* Journal of Manufacturing Processes, 2012. **14**(3): p. 188-194.
155. Usui, E., T. Shirakashi, and T. Kitagawa, *Analytical Prediction of Three Dimensional Cutting Process—Part 3: Cutting Temperature and Crater Wear of Carbide Tool.* Journal of Engineering for Industry, 1978. **100**(2): p. 236.
156. Usui, E., A. Hirota, and M. Masuko, *Analytical prediction of three dimensional cutting process. part 1. Basic cutting model and energy approach.* Trans ASME-J Eng Ind, 1978. **100**: p. 222-228.
157. Usui, E. and A. Hirota, *Analytical prediction of three dimensional cutting process. part 2. chip formation and cutting force with conventional single-point tool.* Trans ASME-J Eng Ind, 1978. **100**: p. 229-235.

158. Strenkowski, J.S. and J.T. Carroll, III. *An orthogonal metal cutting model based on an Eulerian finite element method,Manufacturing Processes, Machines and Systems*. 1986.
159. Strenkowski, J.S., A.J. Shih, and J.C. Lin, *An analytical finite element model for predicting three-dimensional tool forces and chip flow.* International Journal of Machine Tools and Manufacture, 2002. **42**(6): p. 723-731.
160. Strenkowski, J.S. and K.-J. Moon, *Finite element prediction of chip geometry and tool/workpiece temperature distributions in orthogonal metal cutting.* Journal of Engineering for Industry, 1990. **112**(4): p. 313.
161. Athavale, S.M., J.S. Strenkowski, and N. Carolina, *Material damage-based model for predicting chip-breakability.* Journal of Manufacturing Science and Engineering, 1997. **119**(NOVEMBER): p. 675-680.
162. Puls, H., F. Klocke, and D. Lung, *Experimental investigation on friction under metal cutting conditions.* Wear, 2014. **310**(1-2): p. 63-71.
163. Childs, T., K. Maekawa, T. Obikawa, and Y. Yamane,, *Finite element methods*, in *Chip formation fundamentals: metal machining theory and applications*. 2000, John Wiley and Sons Ltd.
164. Donea, J., et al., *Arbitrary Lagrangian-Eulerian Methods*. 2004, John Wiley and Sons Ltd. p. 1-25.
165. Hu, F. and D. Li, *Modelling and simulation of milling forces using an arbitrary lagrangian–eulerian finite element method and support vector regression.* Journal of Optimization Theory and Applications, 2011. **153**(2): p. 461-484.
166. Movahhedy, M.R., Y. Altintas, and M.S. Gadala, *Numerical analysis of metal cutting with chamfered and blunt tools.* Journal of Manufacturing Science and Engineering, 2002. **124**(2): p. 178.
167. Olovsson, L., L. Nilsson, and K. Simonsson, *ALE formulation for the solution of two-dimensional metal cutting problems.* Computers and Structures, 1999. **72**(4): p. 497-507.
168. Li, L., Y. Ding, and V. Engineering. *Finite element modeling method of chip formation based on ale approach*. 2010. ASME Digital Collection.
169. Haglund, A.J., H.A. Kishawy, and R.J. Rogers, *An exploration of friction models for the chip–tool interface using an Arbitrary Lagrangian–Eulerian finite element model.* Wear, 2008. **265**(3-4): p. 452-460.
170. Arrazola, P.J. and T.r. Özel, *Investigations on the effects of friction modeling in finite element simulation of machining.* International Journal of Mechanical Sciences, 2010. **52**(1): p. 31-42.
171. Agmell, M., A. Ahadi, and J.-E. Ståhl, *Identification of plasticity constants from orthogonal cutting and inverse analysis.* Mechanics of Materials, 2014. **77**: p. 43-51.
172. Xie, L.J., et al., *2D FEM estimate of tool wear in turning operation.* Wear, 2005. **258**(10): p. 1479-1490.
173. Attanasio, A., et al., *Investigation and FEM-based simulation of tool wear in turning operations with uncoated carbide tools.* Wear, 2010. **269**(5-6): p. 344-350.
174. Attanasio, A., et al., *3D finite element analysis of tool wear in machining.* CIRP Annals - Manufacturing Technology, 2008. **57**(1): p. 61-64.

175. A. Attanasio, E.C., C. Giardini, L. Filice, D. Umbrello, *Criterion to evaluate diffusive wear in 3D simulations when turning AISI 1045 steel.* International Journal of Material Forming, 2008. **1**: p. 495-498.
176. Gingold, R.A. and J.J. Monaghan, *Smoothed particle hdyrodynamics: theory and application to non-spherical stars.* Mon. Not. R.astr. Soc., 1977. **181**: p. 375-389.
177. Ambati, R., et al., *Application of material point methods for cutting process simulations.* Computational Materials Science, 2012. **57**: p. 102-110.
178. Ueda, K., et al., *A J-Integral Approach to Material Removal Mechanisms in Microcutting of Ceramics.* CIRP Annals - Manufacturing Technology, 1991. **40**(1): p. 61-64.
179. Xlet, J.Q.B.A.E.Z.H.M., *A study on shear banding in chip formation of orthogonal machining.* International Journal of Machine Tools and Manufacture, 1996. **36**(7): p. 835-847.
180. Obikawa, T., et al., *Application of computational machining method to discontinuous chip formation.* Journal of Manufacturing Science and Engineering, 1997. **119**(4B): p. 667-667.
181. Idelsohn, S.R., E. Oñate, and F.D. Pin, *The particle finite element method: a powerful tool to solve incompressible flows with free-surfaces and breaking waves.* International Journal for Numerical Methods in Engineering, 2004. **61**(7): p. 964-989.
182. OÑAte, E., et al., *the Particle Finite Element Method — an Overview.* International Journal of Computational Methods, 2004. **01**(02): p. 267-307.
183. Onate, E. and R. Owen, *Particle-based methods Fundamentals and applications*. Vol. 25. 2011: Springer.
184. Idelsohn, S.R., et al., *The meshless finite element method.* International Journal for Numerical Methods in Engineering, 2003. **58**(6): p. 893-912.
185. Oñate, E., et al., *Advances in the particle finite element method for the analysis of fluid–multibody interaction and bed erosion in free surface flows.* Computer Methods in Applied Mechanics and Engineering, 2008. **197**(19-20): p. 1777-1800.
186. Oñate, E., M.A. Celigueta, and S.R. Idelsohn, *Modeling bed erosion in free surface flows by the particle finite element method.* Acta Geotechnica, 2006. **1**(4): p. 237-252.
187. E. Oñate , R.O., *Particle finite element method in solid mechanics problem*, in *computational plasticity.* 2007, Springer: Dordrecht.
188. Carbonell, J.M., E. Oñate, and B. Suárez, *Modelling of tunnelling processes and rock cutting tool wear with the particle finite element method.* Computational Mechanics, 2013. **52**(3): p. 607-629.
189. Sabel, M., C. Sator, and R. Müller, *Particle finite element analysis of cutting processes.* Pamm, 2014. **14**(1): p. 259-260.
190. Sabel, M., C. Sator, and R. Müller, *A particle finite element method for machining simulations.* Computational Mechanics, 2014. **54**(1): p. 123-131.

191. Rodríguez, J., et al., *A sensibility analysis to geometric and cutting conditions using the particle finite element method (PFEM).* Procedia CIRP, 2013. **8**: p. 105-110.
192. Fraunhofer. *FPM- Finite Pointset Method*. 2016 20/02/2016]; Available from: http://www.itwm.fraunhofer.de/en/departments/transport-processes/products/fpm-finite-pointset-method.html.
193. Uhlmann, E., R. Gerstenberger, and J. Kuhnert, *Cutting simulation with the meshfree finite pointset method.* Procedia CIRP, 2013. **8**: p. 391-396.
194. Uhlmann, E., et al. *The finite pointset method for the meshfree numerical simulation of chip formation*. 2009.
195. P.A Cundall, O.D.L.S., *A discrete numerical model for granular assemblies.* Geotechnique, 1979. **29**(1): p. 47-65.
196. Tan, Y., D. Yang, and Y. Sheng, *Study of polycrystalline Al2O3 machining cracks using discrete element method.* International Journal of Machine Tools and Manufacture, 2008. **48**(9): p. 975-982.
197. Fleissner, F., T. Gaugele, and P. Eberhard, *Applications of the discrete element method in mechanical engineering.* Multibody System Dynamics, 2007. **18**(1): p. 81-94.
198. Qiu, Y., M. Gu, and Z. Wei, *Machining mechanism research of glass by discrete element method.* Journal of Mechanical Science and Technology, 2015. **29**(3): p. 1283-1288.
199. Tan, Y., D. Yang, and Y. Sheng, *Discrete element method (DEM) modeling of fracture and damage in the machining process of polycrystalline SiC.* Journal of the European Ceramic Society, 2009. **29**(6): p. 1029-1037.
200. Iliescu, D., et al., *A discrete element method for the simulation of CFRP cutting.* Composites Science and Technology, 2010. **70**(1): p. 73-80.
201. Eberhard, P. and T. Gaugele, *Simulation of cutting processes using mesh-free Lagrangian particle methods.* Computational Mechanics, 2012. **51**(3): p. 261-278.
202. Cleary, P.W., M. Prakash, and J. Ha, *Novel applications of smoothed particle hydrodynamics (SPH) in metal forming.* Journal of Materials Processing Technology, 2006. **177**(1-3): p. 41-48.
203. Madaj, M. and M. Píška, *On the sph orthogonal cutting simulation of A2024-T351 Alloy.* Procedia CIRP, 2013. **8**: p. 152-157.
204. Rüttimann, N., et al., *Simulation of hexa-octahedral diamond grain cutting tests using the sph method.* Procedia CIRP, 2013. **8**: p. 322-327.
205. Das, R. and P.W. Cleary, *Effect of rock shapes on brittle fracture using Smoothed Particle Hydrodynamics.* Theoretical and Applied Fracture Mechanics, 2010. **53**(1): p. 47-60.
206. Bui, H.H., et al., *Lagrangian meshfree particles method (SPH) for large deformation and failure flows of geomaterial using elastic-plastic soil constitutive model.* International Journal for Numerical and Analytical Methods in Geomechanics, 2008. **32**(12): p. 1537-1570.
207. Lin, J., et al., *Efficient meshless SPH method for the numerical modeling of thick shell structures undergoing large deformations.* International Journal of Non-Linear Mechanics, 2014. **65**: p. 1-13.

208. Nordendale, N.a., W.F. Heard, and P.K. Basu, *Modeling of high-rate ballistic impact of brittle armors with Abaqus / Explicit*. 2012. p. 1-14.
209. Russel, K.S., *Smoothed particle hdyrodynamics modelling for failure in metals*. 2010. p. 328-328.
210. Villumsen, M.F. and T.G. Fauerholdt. *Simulation of metal cutting using smooth particle hydrodynamics*. 2008. DYNAmore GmbH.
211. Zhao, H., et al., *Influences of sequential cuts on micro-cutting process studied by smooth particle hydrodynamic (SPH).* Applied Surface Science, 2013. **284**: p. 366-371.
212. Gąsiorek, D., *The application of the smoothed particle hydrodynamics (SPH) method and the experimental verification of cutting of sheet metal bundles using a guillotine.* Journal of Theoretical and Applied Mechanics, 2013. **51**(4): p. 1053-1065.
213. Xi, Y., et al., *SPH/FE modeling of cutting force and chip formation during thermally assisted machining of Ti6Al4V alloy.* Computational Materials Science, 2014. **84**: p. 188-197.
214. Guo, X., et al., *A numerical model for optical glass cutting based on SPH method.* The International Journal of Advanced Manufacturing Technology, 2013. **68**(5-8): p. 1277-1283.
215. Calamaz, M., et al., *Toward a better understanding of tool wear effect through a comparison between experiments and SPH numerical modelling of machining hard materials.* International Journal of Refractory Metals and Hard Materials, 2009. **27**(3): p. 595-604.
216. Lungu, N.C.S.M.B.M., *Optimization of cutting tool geometrical parameters using taguchi method.* Academic Journal of Manufacturing Engineering, 2013. **11**(4): p. 62-67.
217. Makadia, A.J. and J.I. Nanavati, *Optimisation of machining parameters for turning operations based on response surface methodology.* Measurement, 2013. **46**(4): p. 1521-1529.
218. Shetty, R., et al., *Taguchi's technique in machining of metal matrix composites.* Journal of the Brazilian Society of Mechanical Sciences and Engineering, 2009. **31**(1): p. 12-20.
219. Malakizadi, A., et al., *Inverse identification of flow stress in metal cutting process using Response Surface Methodology.* Simulation Modelling Practice and Theory, 2016. **60**: p. 40-53.
220. Bİrcan, D.A., *Investigation of Cutting Parameters of Drilling Ti6Al4V Using Finite Element Analysis.* International journal of natural and engineering sciences, 2015. **9**(2): p. 25-31.
221. Chen, W.C., *Effect of the cross-sectional shape design of a drill body on drill temperature distributions.* International Communications in Heat and Mass Transfer, 1996. **23**(3): p. 355-366.
222. Fallis, A.G., *Finite element analysis of hastelloy C-22Hs in end milling.* Journal of Mechanical engineering and sciences, 2011. **1**: p. 37-46.
223. Adetoro, M.B. and P.H. Wen. *FEM Evaluation of Mechanistic Cutting Force Coefficients Using ALE Formulation*.
224. Man, X., et al., *Validation of finite element cutting force prediction for end milling.* Procedia CIRP, 2012. **1**: p. 663-668.

225. Holtermann, R., et al., *Towards the simulation of grinding processes - a thermoplastic single grain approach.* Pamm, 2011. **11**(1): p. 385-386.
226. Fuh, K.-h. and J.-s. Huang, *Thermal analysis of creep-feed grinding.* Journal of Materials Processing Technology, 1994. **43**: p. 109-124.
227. Mackerle, J., *Finite-element analysis and simulation of machining: a bibliography (1976–1996).* Journal of Materials Processing Technology, 1998. **86**(1-3): p. 17-44.
228. Ceretti, E., et al., *Turning simulations using a three-dimensional fem code.* Journal of Materials Processing Technology, 2000. **98**: p. 99-103.
229. Ducobu, F., E. Rivière-Lorphèvre, and E. Filippi, *On the introduction of adaptive mass scaling in a finite element model of Ti6Al4V orthogonal cutting.* Simulation Modelling Practice and Theory, 2015. **53**: p. 1-14.
230. Guediche, M., et al., *A new procedure to increase the orthogonal cutting machining time simulated.* Procedia CIRP, 2015. **31**: p. 299-303.
231. Lin, Z.-C. and Y.-Y. Lin, *A study of an oblique cutting model.* Journal of Materials Processing Technology, 1999. **86**(1-3): p. 119-130.
232. Lin, Z.C. and Y.Y. Lin, *A study of oblique cutting for different low cutting speeds.* Journal of Materials Processing Technology, 2001. **115**(3): p. 313-325.
233. Lin, Z.-C. and Y.-Y. Lin, *Fundamental modeling for oblique cutting by thermo-elastic-plastic FEM.* International Journal of Mechanical Sciences, 1999. **41**: p. 941-965.
234. Bacaria, J.L. and O. Dalverny, *2D and 3D numerical models of metal cutting with damage effects.* Computer methods in, 2004(September): p. 11-14.
235. T.D. Marusich, M.O., *Modeling and simulation of high speed machining.* International Journal for Numerical Methods in Engineering, 1995. **38**: p. 3675-3694.
236. Ducobu, F., E. Rivière-Lorphèvre, and E. Filippi, *Numerical contribution to the comprehension of saw-toothed Ti6Al4V chip formation in orthogonal cutting.* International Journal of Mechanical Sciences, 2014. **81**: p. 77-87.
237. Childs, T., et al., *Chip formation fundamentals*, in m*etal machining theory and applications*. 2000.
238. Han, X., *Analysis Precision Machining Process Using Finite Element Method*. 2012.
239. Lin, Z.C. and W.C. Pan, *A thermoelastic-plastic large deformation model for orthogonal cutting with tool flank wear - Part 2: Machining application.* Int. J. Mech. Sci., 1993. **35**(10): p. 829-840.
240. Lin, Z.C. and S.Y. Lin, *A coupled finite element model of thermo-elastic-plastic large deformation for orthogonal cutting.* Journal of Engineering Materials and Technology, 1992. **114**(2): p. 218.
241. Hillerborg, A., M. Mod´eer, and P.E. Petersson, *Analysis of crack formation and crack growth in concrete by means of fracture mechanics and finite elements.* Cement and Concrete Research, 1976. **6**: p. 773-782.

242. Hashemi, J., A.A. Tseng, and P.C. Chou, *Finite element modeling of segmental chip formation in high-speed orthogonal cutting.* Journal of Materials Engineering and Performance, 1994. **3**(6): p. 712-721.
243. Owen, D.R.J. and M. Vaz, *Computational techniques applied to high-speed machining under adiabatic strain localization conditions.* Computer Methods in Applied Mechanics and Engineering, 1999. **171**(3-4): p. 445-461.
244. Lemaitre, J., *A continuous damage mechanics model for ductile fracture.* J. Eng. Mater. Technol.(Trans. ASME), 1985. **107**(January 1985): p. 83-89.
245. Chen, G., et al., *Measurement and finite element simulation of micro-cutting temperatures of tool tip and workpiece.* International Journal of Machine Tools and Manufacture, 2013. **75**: p. 16-26.
246. Ducobu, F., E. Rivière-Lorphèvre, and E. Filippi, *Influence of the Material Behavior Law and Damage Value on the Results of an Orthogonal Cutting Finite Element Model of Ti6Al4V.* Procedia CIRP, 2013. **8**: p. 379-384.
247. Guerra Silva, R., et al., *Finite element modeling of chip separation in machining cellular metals.* Advances in Manufacturing, 2015. **3**(1): p. 54-62.
248. Xie, J.Q., A.E. Bayoumi, and H.M. Zbib, *FEA modeling and simulation of shear localized chip formation in metal cutting.* International Journal of Machine Tools and Manufacture, 1998. **38**(9): p. 1067-1087.
249. Guo, J.Y. and M. Lv, *Explicit finite element simulation of oblique cutting process.* Key Engineering Materials, 2010. **431-432**: p. 297-300.
250. Iwata, K., K. Osakada, and Y. Terasaka, *Process modeling of orthogonal cutting by the rigid-plastic finite element method.* Journal of Engineering Materials and Technology, 1984. **106**(2): p. 132.
251. Zhang, B. and A. Bagchi, *Finite element simulation of chip formation and comparison with machining experiment.* Journal of Engineering for Industry, 1994. **116**(3): p. 289.
252. Ueda, K. and K. Manabe, *Rigid-Plastic FEM analysis of three-dimensional deformation field in chip formation process.* CIRP Annals - Manufacturing Technology, 1993. **42**(1): p. 35-38.
253. Huang, J.M. and J.T. Black, *An evaluation of chip separation criteria for the fem simulation of machining.* Journal of Manufacturing Science and Engineering, 1996. **118**(4): p. 545.
254. Chandrakanth Shet, X.D., *Finite element analysis of the orthogonal metal cutting process.* Journal of Materials Processing Technology, 2000. **105**(April 1999): p. 95-109.
255. Guoqin, S., D. Xiaomin, and C. Shet, *A finite element study of the effect of friction in orthogonal metal cutting.* Finite Elements in Analysis and Design, 2002. **38**(9): p. 863-883.
256. Zienkiewicz, O.C., R.L. Taylor, and J.Z. Zhu, *Automatic mesh generation*, in *the finite element method: Its basis and fundamentals*. 2013, Elsevier.

257. Barge, M., et al., *Numerical modelling of orthogonal cutting: influence of numerical parameters.* Journal of Materials Processing Technology, 2005. **164-165**: p. 1148-1153.
258. Bäker, M., *Finite element simulation of high-speed cutting forces.* Journal of Materials Processing Technology, 2006. **176**(1-3): p. 117-126.
259. Simulia, D., *Abaqus 6.14 documentation*. 2014.
260. Branco, R., F.V. Antunes, and J.D. Costa, *A review on 3D-FE adaptive remeshing techniques for crack growth modelling.* Engineering Fracture Mechanics, 2015. **141**: p. 170-195.
261. E. Usui, T.S. and T. Kitagawa, *Analytical prediction of cutting tool wear.* Wear, 1984. **100**: p. 129-151.
262. Dan, L. and J. Mathew, *Tool wear and failure monitoring techniques for turning-A review.* International Journal of Machine Tools and Manufacture, 1990. **30**(4): p. 579-598.
263. Takeyama, H. and R. Murata, *Basic Investigation of Tool Wear.* Journal of Engineering for Industry, 1963. **85**(1): p. 33.
264. Shimada, S., et al., *Thermo-chemical wear mechanism of diamond tool in machining of ferrous metals.* CIRP Annals - Manufacturing Technology, 2004. **53**(1): p. 57-60.
265. Matsumura, T., et al., *Autonomous turning operation planning with adaptive prediction of tool wear and surface roughness.* Journal of Manufacturing Systems, 1993. **12**(3): p. 253-262.
266. Attanasio, A., E. Ceretti, and C. Giardini, *Analytical Models for Tool Wear Prediction During AISI 1045 Turning Operations.* Procedia CIRP, 2013. **8**: p. 218-223.
267. Taylor, J., *The tool wear-time relationship in metal cutting.* International Journal of Machine Tool Design and Research, 1962. **2**(2): p. 119-152.
268. Dos Santos, A.L.B., et al., *An optimisation procedure to determine the coefficients of the extended Taylor's equation in machining.* International Journal of Machine Tools & Manufacture, 1999. **39**(1): p. 17-31.
269. Ojha, D.K. and U.S. Dixit, *An economic and reliable tool life estimation procedure for turning.* The International Journal of Advanced Manufacturing Technology, 2005. **26**(7-8): p. 726-732.
270. Binder, M., F. Klocke, and D. Lung, *Tool wear simulation of complex shaped coated cutting tools.* Wear, 2015. **330-331**: p. 600-607.
271. List, G., G. Sutter, and A. Bouthiche, *Cutting temperature prediction in high speed machining by numerical modelling of chip formation and its dependence with crater wear.* International Journal of Machine Tools and Manufacture, 2012. **54-55**: p. 1-9.
272. Childs, T.H.C. and K. Maekawa, *Computer-aided simulation and experimental studies of chip flow and tool wear in the turning of low-alloy steels by cemented carbide tools.* Wear, 1990. **139**(2): p. 235-250.
273. Molinari, A. and M. Nouari, *Modeling of tool wear by diffusion in metal cutting.* Wear, 2002. **252**(1-2): p. 135-149.
274. Nouari, M. and A. Molinari, *Experimental verification of a diffusion tool wear model using a 42CrMo4 steel with an uncoated cemented*

tungsten carbide at various cutting speeds. Wear, 2005. **259**(7-12): p. 1151-1159.

275. Filice, L., et al., *Wear modelling in mild steel orthogonal cutting when using uncoated carbide tools.* Wear, 2007. **262**(5-6): p. 545-554.
276. Zanger, F. and V. Schulze, *Investigations on mechanisms of tool wear in machining of ti-6al-4v using fem simulation.* Procedia CIRP, 2013. **8**: p. 158-163.
277. Monaghan, J. and T. MacGinley, *Modelling the orthogonal machining process using coated carbide cutting tools.* Computational Materials Science, 1999. **16**: p. 275-284.
278. MacGinley, T. and J. Monaghan, *Modelling the orthogonal machining process using cutting tools with different geometry.* Journal of Materials Processing Technology, 2001. **118**: p. 293-300.
279. Matsumura, T., T. Shirakashi, and E. Usui, *Identification of Wear Characteristics in Tool Wear Model of Cutting Process.* International Journal of Material Forming, 2008. **1**(S1): p. 555-558.
280. Zhang, B., et al., *Finite elementt simulation and analysis on wear of mechanical graver for diffraction grating.* Journal of Theoretical and Applied Information Technology, 2012. **46**(1): p. 289-293.
281. Yen, Y.-C., et al., *Estimation of tool wear in orthogonal cutting using the finite element analysis.* Journal of Materials Processing Technology, 2004. **146**(1): p. 82-91.
282. Yen, Y.C., et al., *Estimation of tool wear of carbide tool in orthogonal cutting using fem simulation.* Machining Science and Technology, 2002. **6**(3): p. 467-486.
283. Ceretti, E., et al., *Diffusion wear modelling in 3D cutting process.* International journal of machining and machinability of materials, 2009. **6**(1/2): p. 10-12.
284. Mathew, P., *Use of predicted cutting temperatures in determining tool performance.* International Journal of Machine Tools and Manufacture, 1989. **29**(4): p. 481-497.
285. Lorentzon, J. and N. Järvstråt, *Modelling tool wear in cemented-carbide machining alloy 718.* International Journal of Machine Tools and Manufacture, 2008. **48**(10): p. 1072-1080.
286. Schulze, V. and F. Zanger, *Development of a simulation model to investigate tool wear in Ti-6Al-4V Alloy Machining.* Advanced Materials Research, 2011. **223**: p. 535-544.
287. Salvatore, F., S. Saad, and H. Hamdi, *Modeling and simulation of tool wear during the cutting process.* Procedia CIRP, 2013. **8**: p. 305-310.
288. Yue, C.X., et al., *2D FEM estimate of tool wear in hard cutting operation: extractive of interrelated parameters and tool wear simulation result.* Advanced Materials Research, 2009. **69-70**: p. 316-321.
289. Li, K., X.L. Gao, and J.W. Sutherland, *Finite element simulation of the orthogonal metal cutting process for qualitative understanding of the effects of crater wear on the chip formation process.* Journal of Materials Processing Technology, 2002. **127**(3): p. 309-324.
290. Ducobu, F., et al., *Finite Element Prediction of the Tool wear Influence in Ti6Al4V Machining.* Procedia CIRP, 2015. **31**: p. 124-129.

291. Zorev, N.N. *Interrelationship between shear processes occurring along tool face and on shear plane in metal cutting*. 1963.

292. Ozel, T. and T. Altan, *Determination of workpiece flow stress and friction at the chip-tool contact for high-speed cutting.* International Journal of Machine Tools and Manufacture, 2000. **40**(1): p. 133-152.

293. Childs, T.H.C., M.I. Mahdi, and G. Barrow, *On the stress distribution between the chip and tool during metal turning.* CIRP Annals - Manufacturing Technology, 1989. **38**(1): p. 55-58.

294. Oxley, P.L.B. and A.P. Hatton, *shear angle solution based on experimental shear zone and tool chip interface stress distribution.* International Journal of Mechanical Sciences, 1963. **5**: p. 41-55.

295. Barrow, G., et al., *Determination of rake face stress distribution in orthogonal machining.* International Journal of Machine Tool Design and Research, 1982. **22**(1): p. 75-85.

296. Buryta, D., R. Sowerby, and I. Yellowley, *Stress distribution on the rake face during orthogonal machining.* International Journal of Machine Tools and Manufacture, 1994. **34**(5): p. 721-739.

297. Mamalis, A.G., A.S. Branis, and D.E. Manolakos, *Modelling of precision hard cutting using implicit finite element methods.* Journal of Materials Processing Technology, 2002. **123**(3): p. 464-475.

298. T. TYAN , W.H.Y., *Analysis of orthogonal metal cutting processes.* International Journal for Numerical Methods in Engineering, 1992. **34**: p. 365-389.

299. Seshadri, R., et al., *Finite element simulation of the orthogonal machining process with Al 2024 T351 Aerospace Alloy.* Procedia Engineering, 2013. **64**: p. 1454-1463.

300. Lei, S., Y.C. Shin, and F.P. Incropera, *Thermo-mechanical modeling of orthogonal machining process by finite element analysis.* International Journal of Machine Tools and Manufacture, 1999. **39**: p. 731-750.

301. Zong, W.J., et al., *Finite element optimization of diamond tool geometry and cutting-process parameters based on surface residual stresses.* The International Journal of Advanced Manufacturing Technology, 2006. **32**(7-8): p. 666-674.

302. Guo, Y.B., *Finite element modeling of residual stress profile patterns in hard turning.* JCPDS-International centre for diffraction data, 2009. **24**: p. 344-351.

303. Merchant, M.E., *Mechanics of the Metal Cutting Process. I. Orthogonal Cutting and a Type 2 Chip.* Journal of Applied Physics, 1945. **16**(5): p. 267.

304. Lo, S.P., *An analysis of cutting under different rake angles using the finite element method.* Journal of Materials Processing Technology, 2000. **105**(1-2): p. 143-151.

305. Ng, E.G., et al., *Modelling of temperature and forces when orthogonally machining hardened steel.* International Journal of Machine Tools and Manufacture, 1999. **39**: p. 885-903.

306. Shi, J. and C.R. Liu, *The influence of material models on finite element simulation of machining.* Journal of Manufacturing Science and Engineering, 2004. **126**(4): p. 849.

307. Arrazola, P.J., D. Ugarte, and X. Domínguez, *A new approach for the friction identification during machining through the use of finite element modeling.* International Journal of Machine Tools and Manufacture, 2008. **48**(2): p. 173-183.
308. Lei, S., Y.C. Shin, and F.P. Incropera, *Material constitutive modeling under high strain rates and temperatures through orthogonal machining tests.* Journal of Manufacturing Science and Engineering, Transactions of the ASME, 1999. **121**(4): p. 577-585.
309. Jaspers, S.P.F.C. and J.H. Dautzenberg, *Material behaviour in metal cutting: strains, strain rates and temperatures in chip formation.* Journal of Materials Processing Technology, 2002. **121**(1): p. 123-135.
310. Abukhshim, N.A., P.T. Mativenga, and M.A. Sheikh, *Heat generation and temperature prediction in metal cutting: A review and implications for high speed machining.* International Journal of Machine Tools and Manufacture, 2006. **46**(7-8): p. 782-800.
311. Kara, F., K. Aslantaş, and A. Çiçek, *Prediction of cutting temperature in orthogonal machining of AISI 316L using artificial neural network.* Applied Soft Computing, 2016. **38**: p. 64-74.
312. Tay, A.O., M.G. Stevenson, and G.d.V. Davis, *Using the finite element method to determine temperature distributions in orthogonal machining.* ARCHIVE: Proceedings of the Institution of Mechanical Engineers 1847-1982 (vols 1-196), 1974. **188**(1974): p. 627-638.
313. Analysis, S. and I. Saulcy, *Residual stresses in orthogonal cutting of metals: The effect of thermomechanical coupling parameter and of friction.* Journal of thermal stresses, 2009. **32**(3): p. 269-289.
314. Maekawa, K., Y. Nakano, and T. Kitagawa, *Finite element analysis of thermal behaviour in metal machining (Ist report, influence of thermophysical properties on cutting temperature).* Transactions of Japenese society of mechanical engineers, 1996. **62**(596): p. 1587-1593.
315. Gasiorek, D., *The Application of the Smoothed Particle Hydrodynamics (Sph) Method and the Experimental Verification of Cutting of Sheet Metal Bundles Using a Guillotine.* Journal of Theoretical and Applied Mechanics, 2013. **51**(4): p. 1053-1065.
316. Bawaneh, M.A. and V. Madhavan, *Determination of material constitutive models using orthogonal machining tests.* Department of Industrial and Manufacturing Engineering, 2007. **PhD**(December).
317. Klocke, F., H.W. Raedt, and S. Hoppe, *2d-Fem Simulation of the Orthogonal High Speed Cutting Process.* Machining Science and Technology, 2001. **5**(3): p. 323-340.
318. Johnson, G.R. and W.H. Cook, *A constitutive model and data for metals subjected to large strain, high strain rates and high temperatures.* 7 Internation Sympodium on ballistics proceedings, 1983: p. 541-547.
319. Calamaz, M., D. Coupard, and F. Girot, *A new material model for 2D numerical simulation of serrated chip formation when machining titanium alloy Ti–6Al–4V.* International Journal of Machine Tools and Manufacture, 2008. **48**(3-4): p. 275-288.

320. Sima, M. and T. Özel, *Modified material constitutive models for serrated chip formation simulations and experimental validation in machining of titanium alloy Ti–6Al–4V.* International Journal of Machine Tools and Manufacture, 2010. **50**(11): p. 943-960.
321. Özel, T. and E. Zeren, *Determination of work material flow stress and friction for FEA of machining using orthogonal cutting tests.* Journal of Materials Processing Technology, 2004. **153-154**: p. 1019-1025.
322. Okhrimenko, G.M., *Single crystal silicon piezoelectric ceramics and ferrite under uniaxial compression.* Problemy Prochnosti, 1989. **9**: p. 45-80.
323. Drucker, D.C. and W.J. Prager, *Soil mechanics and plastic analysis or limit design*. 1952, Brown University, Division of Applied Mathematics.
324. Simulia, *User documentation, Abaqus 6.14 Software manual*. 2014.
325. Juliano, T., V. Domnich, and Y. Gogotsi, *Examining pressure-induced phase transformations in silicon by spherical indentation and Raman spectroscopy: A statistical study.* Journal of Materials Research, 2011. **19**(10): p. 3099-3108.
326. Cao, Y.P., M. Dao, and J. Lu, *A precise correcting method for the study of the superhard material using nanoindentation tests.* Journal of Materials Research, 2011. **22**(05): p. 1255-1264.
327. Sartkulvanich, P., F. Koppka, and T. Altan, *Determination of flow stress for metal cutting simulation—a progress report.* Journal of Materials Processing Technology, 2004. **146**(1): p. 61-71.
328. Yan, J., H. Zhao, and T. Kuriyagawa, *Effects of tool edge radius on ductile machining of silicon: an investigation by FEM.* Semiconductor Science and Technology, 2009. **24**(7): p. 075018.
329. Venkatachalam, S., et al., *Crystallographic Effects on Microscale Machining of Polycrystalline Brittle Materials.* Journal of Micro and Nano-Manufacturing, 2013. **1**(4): p. 041001.
330. Barkachary, B.M. and S.N. Joshi, *Integrated finite element method and response surface methodology-based modelling and simulation of single point diamond turning of silicon.* International Journal of Machining and Machinability of Materials, 2015. **17**(3/4): p. 330.
331. Barkachary, B.M.J., Shrikrishna N., *Integrated finite element method and response surface methodology-based modelling and simulation of single point diamond turning of silicon.* Machining and machinability of materials, 2015. **17**(3-4).
332. Venkatachalam, S., *Predictive modelling for ductile machining of brittle materials*. 2007, Georgia Institute of Technology.
333. Banerjee, A., et al., *An Experimental Determination of Johnson Cook Material and Failure Model Constants for Armour Steel.* Applied Mechanics and Materials, 2014. **592-594**: p. 990-995.
334. Ozel, T. and Y. Karpat, *Identification of constitutive material model parameters for high-strain rate metal cutting conditions using evolutionary computational algorithms.* Materials and Manufacturing Processes, 2007. **22**(5-6): p. 659-667.

335. BATRA, R.C. and C.H. KIM, *Effects of viscoplastic flow rules on the initiation and growth of shear bands at high strain rates.* J. Mech. Phys. Solids, 1990. **38**: p. 859-874.
336. Batra, R.C. and N.A. Jaber, *Failure mode transition speeds in an impact loaded prenotched plate with four thermoviscoplastic relations.* International Journal of Fracture, 2001. **110**(1): p. 47-71.
337. Zhan, H., et al., *Constitutive modelling of the flow behaviour of a β titanium alloy at high strain rates and elevated temperatures using the Johnson–Cook and modified Zerilli–Armstrong models.* Materials Science and Engineering: A, 2014. **612**: p. 71-79.
338. Wang, X., et al., *Dynamic behavior and a modified Johnson–Cook constitutive model of Inconel 718 at high strain rate and elevated temperature.* Materials Science and Engineering: A, 2013. **580**: p. 385-390.
339. Kolsky, H., *An Investigation of the Mechanical Properties of Materials at Very High Rates of Loading.* proceedings of Royal Society. **62**(11): p. 676-699.
340. Hopkinson, B., *A method of measuring the pressure produced in teh detonation of high explosives or by the impact of bullets.* Philosophical Transactions of the Royal Society of London series A, 1914. **213**: p. 437-456.
341. Xiao-qiang, W., et al., *Plastic Constitutive Model and Analysis of Flow Stress of 40Cr Quenched and Tempered Steel.* ISRN Mechanical Engineering, 2013. **2013**: p. 1-6.
342. Shrot, A. and M. Bäker, *Determination of Johnson–Cook parameters from machining simulations.* Computational Materials Science, 2012. **52**(1): p. 298-304.
343. Amiri, S., et al., *Determining Elastic-Plastic Properties of Al6061-T6 from Micro-Indentation Technique.* Key Engineering Materials, 2013. **592-593**: p. 610-613.
344. Holmquist, T.J. and G.R. Johnson, *Determination of Constants and Comparison of Results for Various Constitutive Models.* Le Journal de Physique IV, 1991. **01**(C3): p. C3-853-C3-860.
345. Johnson, G.R. and W.H. Cook. *A Constitutive model and data for metals subjected to large strains, high strain rates and high temperatures*. in *Proceedings of the seventh International symposium on Ballistic*. 1983. The Hague, Netherland.
346. Hopcroft, M.A., W.D. Nix, and T.W. Kenny, *What is the Young's Modulus of Silicon?* Journal of Microelectromechanical Systems, 2010. **19**(2): p. 229-238.
347. Wang, T.H., T.-H. Fang, and Y.-C. Lin, *A numerical study of factors affecting the characterization of nanoindentation on silicon.* Materials Science and Engineering: A, 2007. **447**(1-2): p. 244-253.
348. Chavoshi, S.Z., S. Goel, and X. Luo, *Influence of temperature on the anisotropic cutting behaviour of single crystal silicon: A molecular dynamics simulation investigation.* Journal of Manufacturing Processes, 2016. **23**: p. 201-210.

349. Arif, M., M. Rahman, and W.Y. San, *A state-of-the-art review of ductile cutting of silicon wafers for semiconductor and microelectronics industries.* The International Journal of Advanced Manufacturing Technology, 2012. **63**(5-8): p. 481-504.
350. Jasinevicius, R.G.P., A. J. V.;Duduch, J. G.;Pizani, P. S.;Lanciotti Jr, F.;Santos, F. J. dos, *Multiple phase silicon in submicrometer chips removed by diamond turning.* Journal of the Brazilian Society of Mechanical Sciences and Engineering, 2005. **27**(4): p. 440-448.
351. Zhang, L. and I. Zarudi, *Towards a deeper understanding of plastic deformation in mono-crystalline silicon.* International Journal of Mechanical Sciences, 2001. **43**(9): p. 1985-1996.
352. Durazo-Cardenas, I.S., P.;Luo, X.;Jacklin, T.;Impey, S. A.;Cox, A., *3D characterisation of tool wear whilst diamond turning silicon.* Wear, 2007. **262**(3-4): p. 340-349.
353. W.S.Blackley, R.O.S., *Ductile-regime machining model for diamond turning of brittle materials.* Precision Engineering, 1992. **14**(2): p. 118.
354. Ohta, T., et al., *High-efficiency machining of single-crystal germanium using large-radius diamond tools.* International Journal of Surface Science and Engineering, 2007. **1**(4): p. 374.
355. Goel, S., X. Luo, and R.L. Reuben, *Wear mechanism of diamond tools against single crystal silicon in single point diamond turning process.* Tribology International, 2013. **57**: p. 272-281.
356. Zong, W.J.S., T.;Li, D.;Cheng, K.;Liang, Y. C., *XPS analysis of the groove wearing marks on flank face of diamond tool in nanometric cutting of silicon wafer.* International Journal of Machine Tools and Manufacture, 2008. **48**(15): p. 1678-1687.
357. Cai, M.B., X.P. Li, and M. Rahman, *Characteristics of "dynamic hard particles" in nanoscale ductile mode cutting of monocrystalline silicon with diamond tools in relation to tool groove wear.* Wear, 2007. **263**(7-12): p. 1459-1466.
358. Born, D.K. and W.A. Goodman, *An empirical survey on the influence of machining parameters on tool wear in diamond turning of large single-crystal silicon optics.* Precision Engineering, 2001. **25**(4): p. 247-257.
359. Daniel Charles Drucker, W.P., *Soil mechanics and plastic analysis or limit design.* Quarterly of Applied Mathematics, 1952. **10**(2): p. 157-165.
360. Cheng, K.L., X.;Ward, R.;Holt, R., *Modeling and simulation of the tool wear in nanometric cutting.* Wear, 2003. **255**(7-12): p. 1427-1432.
361. Cai, M.B., X.P. Li, and M. Rahman, *Study of the mechanism of groove wear of the diamond tool in nanoscale ductile mode cutting of monocrystalline silicon.* Journal of Manufacturing Science and Engineering, 2007. **129**(2): p. 281.
362. Rashid, W.B., et al., *An experimental investigation for the improvement of attainable surface roughness during hard turning process.* Proceedings of the Institution of Mechanical Engineers, Part B: Journal of Engineering Manufacture, 2013. **227**(2): p. 338-342.
363. Özel, T., *The influence of friction models on finite element simulations of machining.* International Journal of Machine Tools and Manufacture, 2006. **46**(5): p. 518-530.

364. Fang, N. and I.S. Jawahir, *Analytical predictions and experimental validation of cutting force ratio, chip thickness, and chip back-flow angle in restricted contact machining using the universal slip-line model.* International Journal of Machine Tools & Manufacture, 2002. **42**(6): p. 681-694.
365. Pang, L. and H.A. Kishawy, *modified primary shear zone analysis for identification of material mechanical behavior during machining process using genetic algorithm.* Journal of Manufacturing Science and Engineering, 2012. **134**(4): p. 041003.
366. Lee, S., et al., *Large Strain Deformation Field in Machining.* Metallurgical and Materials Transactions, 2005. **37**(A): p. 1633-1643.
367. Fang, N., *Tool-chip friction in machining with a large negative rake angle tool.* Wear, 2005. **258**(5-6): p. 890-897.
368. Cubberley, W.H. and R. Bakerjian, *Tool and manfuacturing engineers handbook*, ed. S.o.M.E. (SME). 1989, USA.

Appendices

Appendix I

Nanotech 250 UPL ultraprecision diamond turning machine tool used for diamond turning of silicon.

Nanotech 250 UPL CNC diamond turning lathe

Machine Specifications

- Ultraprecision two, three or four axis machine
- T-axis orientation
- Spindle: Air bearing spindle
- Spindle drive system: Frameless, Brushless DC motor
- Motional accuracy: Axial: ≤12.5 nm, Radial: ≤ 12.5 nm
- Liquid cooling to maintain thermal stability
- Optimally located air isolation system
- Programming Resolution: 0.01 nm linear / 0.0000001° rotary
- Fully constrained oil hydrostatic Z-axis
- C-axis

Machine performance

- Form accuracy (P-V): ≤ 0.1 µm / 75mm diameter, 250 mm radius convex sphere
- Surface finish (Ra): ≤ 2.0 nm
- Work capacity: 300 mm diameter, 200 mm long
- Speed range: 50 to 10,000 rpm
- Spindle axial stiffness: 228 N/µm@ 7 bar
- Spindle radial stiffness: 98 N/µm@ 7 bar

Appendix II

Precitech Nanoform 250 UltraGrind machine tool for diamond turning of silicon

Precitech Nanoform 250 ultragrind machine tool

Machine Features

- QNX® real time Operating System with 0.01 nanometer programming resolution.
- Linear holographic glass scales with 16 picometer feedback resolution.
- Windows® interface for easy network integration with Diffsys® Basic.
- Completely sealed stainless steel enclosure.
- Sealed natural granite base providing exceptional long-term machine tool stability.
- FEA optimized dual sub-frames for the ultimate in environmental isolation.
- Linear motors coupled to true analogue linear amplifiers •Modular design for future capability upgrades.

- On-machine workpiece balancing system.
- Hydrostatic oil bearing slideways with optimized stiffness and damping characteristics
- Liquid cooled slides for thermal stability
- Motorized air bearing spindles

Machine Performance

- Diamond Turning Form accuracy: ≤0.15 micron (λ/4) PV
- Surface roughness ≤1.5 nanometer Ra
- High Speed Grinding Form accuracy: ≤0.20 micron (λ/3) PV
- Surface roughness ≤5 nanometer Ra

Appendix III

1- **Split Hopkinson pressure bar** testing equipment for high strain rate compression testing.

Split Hopkinson pressure bar test equipment

Equipment Features

- Modular for tension and compression
- Automated gas launcher
- Testing at room and high temperatures
- Repeatable test velocities within 2% accuracy.
- Bar alignment: 0.001 in/ft flatness
- Compressive testing: strain rates up to 5000 S^{-1}
- Bars straightness: 0.1 mm/m

2- **Instron 8801 (100KN)** for quasi-static compression testing.

Instron 8801 (100KN) Fatigue testing system

System Features

- Up to ±100 kN (22,500 lbf) axial force capacity
- Dynamic and static testing
- High and low-cycle fatigue testing
- Thermomechanical fatigue testing
- Fracture testing
- Load cell features compensation for inertial loads caused by heavy grips and fixtures
- Extra-height frame
- Wide range of grips, fixtures, and accessories